University of Strathclyde

A systematic research on diamond turning using nanoscale multi-tip diamond tools

Zhen Tong

Submitted for the degree of Doctor of Philosophy

Department of Design, Manufacture and Engineering Management
Faculty of Engineering

January 2015

'This thesis is the result of the author's original research. It has been composed by the author and has not been previously submitted for examination which has led to the award of a degree.'

Signed: 

Date: 18/03/2015

Abstract

Recently, great interest has been shown in the fabrication of periodic micro- and nanostructures over large area due to their increasing applications in diverse research fields including optics and electronics, cell biology, bioengineering and medical science. Diamond turning using multi-tip single crystal diamond tools fabricated by focused ion beam (FIB), as a new machining technique, shows powerful capacity in the fabrication of micro- and nanostructures. However, lack of support from systematic theoretical research has seriously hindered the advance and industrialization of this technique. As such, molecular dynamics (MD) simulations and experimental trials have been undertaken in this research work to systematically investigate this new technique from the FIB-induced damage during the tool fabrication process to the nanometric cutting mechanism using nanoscale multi-tip diamond tools.

The transmission electron microscope (TEM) measurements were carried out to characterize the FIB-induced damaged layers in single crystal diamond under different ion beam processing voltages. A novel multi-particle collision MD model was developed to simulate the FIB-induced dynamic damage process in diamond. The results indicated that the fabrication of diamond tool by FIB can create an impulse-dependent damaged layer at the tool surface. The nature of FIB-induced damaged layer in the diamond tool is a mixture phase of sp^2 and sp^3 hybridization and accommodates a significant proportion of the implanted gallium.

The nanometric cutting process of using nanoscale multi-tip diamond tools was studied by MD simulations. The results provide in-depth understandings of the nanostructure generation process, the cutting force, the thermal effect, and the tool geometry-dependent shape transferability. The investigation shows that the formation mechanism of nanostructures when using multi-tip tools is quite different from that of using single tip tools. Since the nanostructures are synchronously formed by a single cutting pass, the effect of feed rate and the alignment issues associated with the use of single tip tools to achieve the same nanostructure can be completely eliminated when using nanoscale multi-tip tools. The unique tool geometrical parameters of a nanoscale multi-tip tool including the tool tip distance, tip angle, and tip configuration play important roles in the form accuracy of the machined nanostructures. A hypothesis of a minimum ratio of tip distance to tip base width (L/W_b) of the

nanoscale multi-tip tool has been proposed and qualitatively validated by nanometric cutting experiments.

A series of nanometric cutting experiments and associated MD simulations were further carried out to study the influence of processing parameters on the integrity of the machined nanostructures and tool wear. Under the studied cutting conditions, the burr and structure damage are the two major types of machining defects. With the increase of the depth of cut and the cutting speed, the increasing overlap effect between the tool tips is responsible for the formation of side burrs and structural damage. The tool wear was initially found at the sides of each tool tip after a cutting distance of 2.5 km. The FIB-induced damaged layer, the friction produced at each side of the tool tip, and the high cutting temperature distributed at the tool cutting edges are responsible for the initiation of tool wear.

Based on the research objectives achieved, generic suggestions are proposed for the further development of diamond turning using nanoscale multi-tip tools in terms of selective parameters used in tool fabrication, optimal design of tool geometry, and optimization of processing parameters in nanometric cutting practice.

Acknowledgement

I am indebted to many for their supports during both the research and the writing of this thesis. First and foremost, I would like to express my deepest gratitude to my supervisor Prof. Xichun Luo for his guidance, attention, encouragement and patience throughout the years. He is definitely my best tutor, influencing my approach to many things both in engineering research and in life.

I would also like to thank Prof. Yingchun Liang, Prof. Xiangqian Jiang, Prof. Liam Blunt, and Prof. Alex Duffy for their valuable suggestions, encouragements, and support on my research work. Without their continuing supports, the completion of the project would not have been possible.

My keen appreciation also goes to my previous colleague Dr. Jining Sun from Heriot-Watt University for training of FIB system and suggestions on my research work. I am grateful to Dr. Sam Mafadzean, Mr. William Smith, and Mr. Colin How from the University of Glasgow for their assistances with FIB and TEM measurements. I would also like to thank Dr. Qunfen Qi and Mr. Christ Dawson from the University of Huddersfield for training on CCI (Form TalySurf CCI 3000) and PGI (Form TalySurf PGI 850). I also acknowledge Mr. Dieter Marschall from Ametek Inc. for training on Precitech Nanoform 250 UltraGrind machine tools. I also extend my sincere thanks to Dr. Donald Maclaren (University of Glasgow, UK), Mr. Andrew Cox (Contour Fine Tooling Limited, UK) for their generous supports and helpful suggestions.

I would also like to thank Heriot-Watt University and the University of Strathclyde for providing me the generous financial support in the form of full scholarship. I would like to acknowledge the technical supports from the high performance computing (HPC) team at the University of Huddersfield and assess to the Huddersfield Queensgate Grid for this study.

I am very grateful to my family, my wife Mrs. Li He and my lovely son Gaobo Tong. Words would be few to describe my gratitude towards my beloved parents, Mrs. Aiqun Zhao and Mr. Chuanren Tong for their endless patience, love, supports and encouragements during the entire research period.

I thank to all my colleagues, especially Dr. Wenlong Chang, Dr. Nitul S Rajput, and Mr Amir Mir for their kind hospitality and supports. I also appreciate all my friends in Heriot-Watt University, the University of Huddersfield, and the University of Strathclyde. Thank you all for a pleasant time.

Table of contents

Nomenclature

E_d	The angular-dependent displacement energy
S_e	The energy loss due to electron
S_n	The energy loss due to neutron
E	System energy
E_{TZBL}	The total energy of the system described by the Tersoff.ZBL potential
V_{ij}^{ZBL}	The ZBL portion of the Tersoff.ZBL potential function
$V_{ij}^{Tersoff}$	The Tersoff portion of the Tersoff.ZBL potential function
r_{ij}	The length of the ij bond
r_{ik}	The length of the ik bond
b_{ij}	The bond order term in Tersoff potential
f_F	Fermi-like function
A_F	Parameters controls the transition between Tersoff and ZBL potentials
r_c	The cut-off distance for the ZBL potential
e	The unit electron charge
ε_0	The permittivity of vacuum
$\phi(r_{ij}/a)$	The ZBL universal screening function
a_0	The Bohr radius
f_R	The repulsive pair potential including two-body interaction
f_A	The attractive pair potential including three-body interactions
f_C	The smooth cut-off function to limit the range of the Tersoff potential
ζ_{ij}	The angle potential portion which counts the number of other bonds to atom i besides the ij bond
A	The cohesion energy of the repulsive pair potential function
B	The cohesion energy of the attractive pair potential function
D	The cut-off distance of Tersoff potential in LAMMPS
S_i	The cut-off distance for specie i in Tersoff potential
S_j	The cut-off distance for specie j in Tersoff potential
R	The radius of first neighbour shell
β_e	The bond order parameter
λ_1	The slope parameter of the repulsive pair potential curve
λ_2	The slope parameter of the attractive pair potential curve
λ_3	The slope parameter of the cut-off potential function

c_e	The elastic parameter in Tersoff potential
d_e	The elastic constant in Tersoff potential
h_e	The elastic constant in Tersoff potential
Z_i	The electron charge of the i-th atom nuclei from the Coulomb potential
Z_j	The electron charge of the j-th atom nuclei from the Coulomb potential
n	The high order constant in Tersoff potential
E_p	The potential energy of the lattice
N_{cell}	Total number of atoms in the simulation cell
E_L	The lattice energy per atom
T_i	The atomistic equivalent temperature of atom i
r_0	The cut-off distance for the calculation of atomistic equivalent temperature
K_E	The total kinetic energy of a group of atoms
k_B	The Boltzmann constant
g(r)	The radial distribution function
a_1	Lattice constant parameter for diamond
a_2	Lattice constant parameter for copper
J (x, y)	The ion flux density at a point (x, y)
I	The ion beam current
σ	The standard deviation of the Gaussian distribution
d_{beam}	The ion beam diameter
V_{beam}	The accelerate voltage of ion beam
t_d	Dwell time
N_{Ga}	The number of incident Ga particles
E_{eam}	The total energy of the system described by the EAM potential
F^i	The individual embedding energy for atom i
$\rho^i(r^{ij})$	The electron density of the atom i contributed by atom j
θ_{ijk}	The bond angle between the bonds ij and ik
E_{tot}	The total energy of the system described by the Morse potential
σ_{hydro}	Hydrostatic stress
σ_{von}	von Mises stress
P_i	The centro-symmetry parameter of atom i
W_a	The top width of the tool tip

W_f	The top width of the tool tip
α	Tool rake angle
β	Tool clearance angle
L	Tool tip distance
Y	The yield stress
E_c	The modulus of elasticity
v	The Poisson's ratio
S_a	The arithmetic average of the 3D surface roughness

Abbreviations

3D	Three Dimensional
a-C	Amorphous Carbon
AFM	Atomic Force Microscope
BCA	Binary Collision Approximation
BCC	Body-Centred Cubic
CADD	Coupled Atomistic and Discrete Dislocation Method
CBED	Convergent Beam Electron Diffraction
CM	Continuum Mechanics
CNA	Coordination Number Analysis
CSP	Centro-Symmetry Parameter
CVD	Chemical Vapour Deposition
DEM	Discrete Element Method
DFT	Density Functional Theory
DLC	Diamond-Like Carbon
DOE	Diffractive Optical Elements
DPN	Dip-Pen Nanolithography
EAM	Embedded Atom Method
EBSD	Electron Backscattered Diffraction
EELS	Electron Energy Loss Spectroscopy
EFTEM	Energy-Filtered Transmission Electron Microscopy
FCC	Face-Centred Cubic
FEA	Finite Element Analysis
FEM	Finite Element Method
FIB	Focused Ion Beam

FTS	Fast Tool Servo
GIS	Gas Injection System
HCI	Highly Charged Ions
HPC	High Performance Computer
LAMMPS	Large Scale Atomic/Molecular Massively Parallel Simulator
LMIS	Liquid Metal Ion Source
MAAD	Macro-Atomistic Ab-initio Dynamics
MC	Monte Carlo
MD	Molecular Dynamics
MDOE	Micro Diffractive Optical Elements
nFTS	nano Fast Tool Servo
OFC	Oxygen Free Copper
PEEK	Polyetheretherketone
QC	Quasi-Continuum
RDF	Radial Distribution Function
RVE	Representative Volume Element
SEM	Scanning Electron Microscope
SHI	Swift Heavy Ions
SIMS	Secondary Ion Mass Spectrometry
SNL	Sandia National Laboratories
SPH	Smoothed Particle Hydrodynamic
STEM	Scanning Transmission Electron Microscopy
STS	Slow Tool Servo
ta-C	Tetrahedral Amorphous Carbon
TBSMA	Tight-Binding Second Moment Approximation

TEM	Transmission Electron Microscope
μEDM	Micro Electro Discharge Machining
VE	Volume Element
VMD	Visual Molecular Dynamics
ZBL	Ziegler, Biersack and Littmark
SPDT	Single Point Diamond Turning

List of tables

List of figures

List of publications from this work

Journal papers:

1. Xichun Luo, **Zhen Tong**, Yingchun Liang, "*Investigation of the shape transferability of nanoscale multi-tip diamond tools in the diamond turning of nanostructures"*. Applied Surface Science. (2014) **321** 495–502. (Impact factor: 2.538).
2. **Zhen Tong,** Yingchun Liang, Xuechun Yang, Xichun Luo. "*Investigation on the thermal effects during nanometric cutting process while using nanoscale diamond tools"*. The International Journal of Advanced Manufacturing Technology. (2014) **74** 1709–1718. (Impact factor: 1.779)
3. **Zhen Tong**, Yingchun Liang, Xiangqian Jiang, Xichun Luo. "*An atomistic investigation on the mechanism of machining nanostructures when using single tip and multi-tip diamond tools".* Applied Surface Science. (2014) **290** 458–465. (Impact factor: 2.538)
4. Nitul S Rajput, **Zhen Tong**, Xichun Luo. *"Investigation of ion induced bending mechanism for nanostructures"*. Mater. Res. Express. (2015) **2** 015002.
5. **Zhen Tong**, Xichun Luo, Jining Sun. *"Investigation of a scale-up manufacturing approach for nanostructures by using a nanoscale multi-tip diamond tool"*. The International Journal of Advanced Manufacturing Technology. (2015) **In press**.
6. **Zhen Tong**, Xichun Luo. *"Investigation on the FIB-induced damage in shaping nanoscale diamond tools"*. Applied Surface Science. (**Under review**)
7. **Zhen Tong**, Zongwei Xu, Wei Wu, Xichun Luo. *"Molecular dynamic simulation of ion-induced damage in diamond under low-energy FIB irradiation"*. Nuclear Instruments and Methods in Physics Research Section B. **(Under review)**
8. Nitul S Rajput, **Zhen Tong**, H C Verma, and Xichun Luo. "*Ion beam assisted fabrication and manipulation of metallic nanowires"*. Micro and Nano letter. **(Under review)**

Conference papers:

1. **Zhen Tong**, Xichun Luo, Jining Sun. *"Investigation of a scale-up manufacturing approach for nanostructures using multi-tip nanoscale diamond tool"*, Proceedings of the 14th EUSPEN International Conference, Dubrovnik, June 2014, pp. 347-350.
2. **Zhen Tong**, Xichun Luo. *"An atomistic investigation of nanometric cutting process using a multi-tip single crystal diamond tool"*. Lamdamap 10th International Conference, Kavli Royal Society International Centre, Buckinghamshire, UK, 20th-21st March 2013. PP. 289-297. (Best paper award)
3. **Zhen Tong**, Xichun Luo, Liam Blunt, Xiangqian Jiang. *"An atomistic investigation of FIB process damage on diamond"*. Proceedings of the 13rd EUSPEN International Conference, Berlin, Germany, 27th-30th May 2013. PP. 265-268.
4. **Z. Tong**, X.C. Luo, Y.C. Liang, Q.S. Bai, J.N. Sun. "*Simulation Research on FIB Processing: A Comparison between Silicon and Diamond"*. Proceedings of the 18th International Conference on Automation & Computing, Loughborough University, Leicestershire, UK, 8 September 2012. PP. 1-5.

Chapter 1 Introduction

1.1 Background and significance

Recently, great interests have been shown in the fabrication of periodic micro- and nanostructures over large area due to their growing applications in new optics, automotive, aerospace, biomedical, and power generation devices [1-4]. The advance in current nanofabrication techniques, including optical and electron beam lithography, focused ion beam (FIB) milling, nanoimprinting, femtosecond laser machining, and diamond machining have boosted the development of such new devices. Some dominant micro- and nanofabrication techniques that are widely used to obtain micro- and nanostructures are listed in Table 1-1.

Photolithography (electron beams, X-rays) [5-7] followed by etching/deposition is the technique most widely used in research labs and semi-conductor industry for micro- and nanofabrication. Usually, a radiation-sensitive medium, i.e. a resist, needs to be used to transfer structures to the bulk material. Then subsequent developments and etching processes or metal thin film deposition process are applied to destruct/construct the form of structures. The main advantages of photolithographic techniques include high precision in achieving nanoscale features and the ability for scalable and high-volume production. However, they are time-consuming and suffering from high capital investment and running cost due to requirements for complex equipment, consumables, and high-end clean room [7]. The materials are limited to silicon, glass, and a few other specific materials.

Focused ion beam (FIB) machining [8-11] is a direct writing technique that requires no mask. Current FIB systems are able to produce a beam size smaller than 3.5 nm with an excellent beam-positioning accuracy and a stable operating condition. These features enable the fabrication of complex three-dimensional (3D) microstructures with high precision by this technique. However, it is inherently a slow nanofabrication procedure and very difficult to

scale-up.

Scanning probe lithography including dip-pen nanolithography (DPN) [12-14] is capable to deposit liquid samples (e.g. proteins, DNA, thiols) for nanoscale surface patterning. Although DPN has many advantages for research applications, this technique is slow and limited in throughput and scalability, which eventually led to the recent liquidation of the only DPN commercial company—NanoInk Inc.

Nanoimprinting lithography [15] is now considered as one of the most promising nanofabrication techniques with the ability to fabrication large area nanostructures at low cost and high throughput. However, the cost and throughput are inherently limited by the size of the nanoscale template (the mould for nanofeature replication). In addition, nanoimprinting only suits fabricating imprintable soft materials (mainly polymers from monomers).

Femtosecond laser machining [16-19] is another state-of-the-art technique in micro- and nanofabrication. However, the machined surface roughness is about 10 times higher than other techniques mentioned before.

All in all, these methods fail to meet the increasing requirement in commercializing functional nanostructured devices due to their inherent limitations, particularly the complex processing steps, low processing efficiency, and high operational costs. These limitations have created substantial interest in developing cost effective scale-up manufacturing approaches.

The mechanical method, typically the single point diamond turning and milling using micro tools as well as their extensions, can be used to fabricate micro- and nanostructures in various materials with a high throughput [20-23]. The classification of the respective diamond cutting methods for machining structured surface is shown in figure 1-1 [24]. The inherent advantage of these processes is the high flexibility while achieving a low surface roughness. The dimensional and form accuracy of the cutting tool itself as well as the motional accuracy of the machine tool are important factors to influence the machining

accuracy of the machined structures. The crystalline structure of diamond permits the fabrication of cutting tools with very sharp cutting edges as small as 25 nm, which enable the nanometre level surface finish of machined structures. Currently, ultra-precision machine tools equipped with air-bearing spindle and high precision work stages can offer nanometre level program resolution. The path program can easily be modified to accommodate design changes, tool radius errors, and other machining anomalies. However, the size and configuration limitations of cutting tools limit the diamond machining to create patterns of sub-micro/nanostructures, especially high aspect ratio structures. The major difficulty to extend the single point diamond turning (SPDT) machining capability to achieve sub-micro/nanoscale structures is the reliable fabrication of nanoscale cutting tools with the required shape and dimensions.

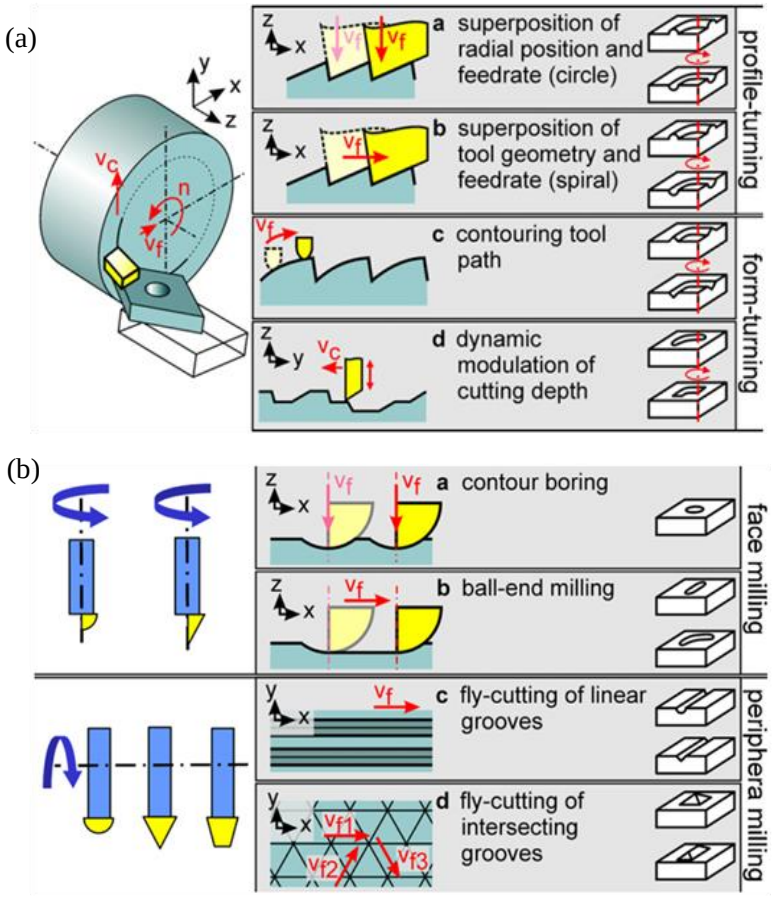

Figure 1-1: Classification of structure generation in (a) diamond turning and (b) diamond milling [24].

Table 1-1: Comparison of different micro- and nano-fabrication technologies

Micro/nano machining technologies	Machining capability	Minimum line width (nm)	Resolution (nm)	Machinable material
Photolithography	3D [25]	~ 4 [26]	~ 10-20 [25]	Silicon, glass, and a few other specific materials
Focused ion beam machining	3D	~ 10 [27]	5 [28]	Almost any solid material
Scanning probe lithography	3D	~ 10 [29]	10 [29]	Soft solid material
Nanoimprinting lithography	3D	~ 10 [28]	~ 10-20 [15]	Imprintable soft materials (mainly polymers from monomers)
Femtosecond laser machining	3D	~ 10 [16]	10 [16]	Almost any solid material
Single point diamond turning (SPDT)	3D	~ 10^4 [30]	~ 10[31]	Materials that are chemically stable with diamond

In recent years, with the advance of FIB processing micro- and nanoscale diamond tools, a newly developed manufacturing approach is to use SPDT process to replicate the micro- or nanostructures pre-fabricated on a diamond tool tip by FIB to a flat surface. Varieties of tool geometries, such as single tipped and dual-tipped tools having rectangular, triangular, and other complex shaped face designs have been produced to generate functional structured surface through ultra-precision lathe turning [32-34]. This approach therefore, fully utilises the fine process capability of the physical sputtering actions of the FIB and the high productivity of diamond turning. Most recently, nano-gratings with the pitch as small as hundreds of nanometres can be generated by this technique while using nanoscale multi-tip diamond tools (with tool tip width of 150 nm) [35, 36]. Owing to the unprecedented merits of high throughput, one-step, and highly flexible precision capabilities, this technique has led to the hope for breaking the technical bottleneck for the scale-up manufacturing nanostructures.

Despite these breakthroughs, there remain significant technical obstacles preventing the commercialization and widespread use of this technique. Apart from the challenges related to the FIB processing of nanoscale diamond tools, the formation mechanism of nanostructures, including the relationship between the geometry of nanostructures pre-fabricated on the tool tip and the form accuracy of nanostructures replicated on the work substrate remains unclear, which has become a significant barrier to realise deterministic nanomanufacturing capability. A systematic investigation combining experiments and simulations needs to be done to fully explore the nanomanufacturing capacity of this technique.

1.2 Aim and objectives

The overall aim of this project is to gain a fundamental understanding of the nanometric cutting using nanoscale multi-tip diamond tools fabricated by FIB. To accomplish this task, large scale MD simulation models in conjunction with experiments are developed to provide an in-depth understanding of the FIB-induced damage during tool fabrication process, the

shape transferability of nanoscale multi-tip diamond tools, and the machining mechanism when using nanoscale multi-tip diamond tools.

In order to achieve the above aim, five main research objectives are set as follows:

- To review the existing literature to gain an understanding of the previous simulation models and identify any advantages and shortcomings of these models.
- To study the FIB-induced damage during nanoscale diamond tool fabrication process, experimentally and theoretically.
- To develop nanometric cutting model to study the shape transferability and the mechanism of machining nanostructures when using nanoscale multi-tip diamond tools.
- To carry out experimental trials to validate the simulations results and to reveal the effect of processing parameters on the quality of machined nanostructures.
- To make generic suggestions for further development of diamond turning using nanoscale multi-tip tools in terms of the selection of parameters used in tool fabrication, the optimal design of tool geometry, and the optimization of processing parameters in nanometric cutting practice.

1.3 Structure of the thesis

The structure of the research is illustrated in figure 1-2. This thesis is presented in eight chapters.

Chapter 1 presents the background of this research project and explains the motivation and objectives of the research work.

Chapter 2 critically reviews the diamond turning of micro- and nanostructures and the major factors which hindered the discovery and advancement of nanoscale multi-tip diamond tools for the deterministic fabrication of sub-micro/nanostructures. It also summarizes the fundamentals of FIB machining technology and the current research progress on the

ion-induced damage in diamond along with some remarks on challenges to remain unsolved.

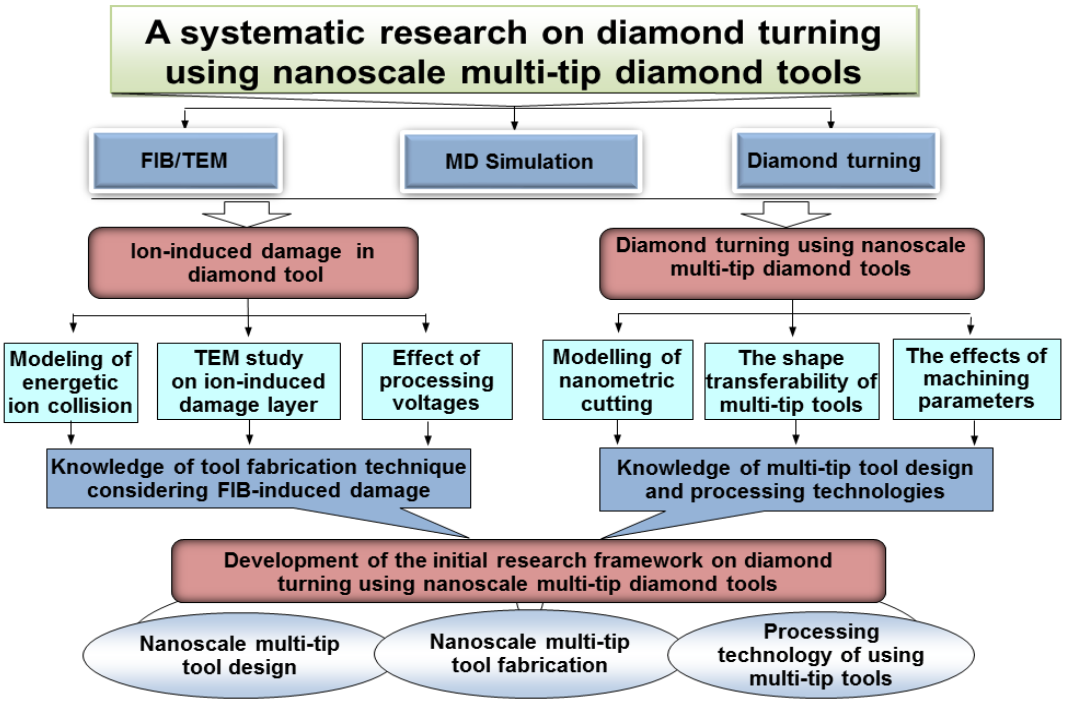

Figure 1-2: The structure of the research project.

Chapter 3 introduces the modelling approach for the study of ion-induced damage in diamond. The basic concept and framework of MD simulation method is first introduced, followed by a discussion of the important parameters for a successful MD simulation of energetic ion bombardment, as well as the post processing methods used for analysing simulation results. Alongside a theoretical description and generic flowchart of building a multi-particle collision model, this chapter presents some preliminary MD simulation results of ion-induced damage in diamond.

Chapter 4 reports a systematic experimental study on FIB-induced damage in diamond tool material. Various efforts to the characterization of the nature of the damage zone created under different FIB processing voltages are carried out. Combined with the results obtained from MD simulations, this chapter provides a detailed description of the ion-induced damage process in diamond. Several suggestions and guidelines for the optimization of experimental

conditions to yield nanoscale multi-tip diamond tools are discussed at the end of this chapter.

Chapter 5 introduces the modelling and simulation methods which provide a foundation for the simulation study on the nanometric cutting when using nanoscale multi-tip diamond tools. Along with a comprehensive discussion on mechanism of machining nanostructures while using a single tip diamond tool and a multi-tip diamond tool, this chapter provides detailed insight into the likely mechanism of machining nanostructures on single crystal copper through diamond turning using nanoscale multi-tip diamond tools.

Chapter 6 describes the details of research on the effect of tool geometrical parameters on the shape transferability of nanoscale multi-tip tools. It offers detailed insight into the nanostructures formation process and a hypothesis of a minimum designed ratio of tip distance to tip base width (L/W_f) of the nanoscale multi-tip tool in machining nanostructures is proposed and qualitatively validated by experiments. The potential of improving the form accuracy of machined nanostructures through an optimal design of the geometry of a nanoscale multi-tip diamond tool is discussed at the end of this chapter.

Chapter 7 presents experiments on diamond turning of copper substrate using nanoscale multi-tip diamond tools under different cutting conditions. As with the MD simulation model, the underlying mechanism for machining defects and the initialization of tool wear observed in experiments are revealed.

Chapter 8 presents the assessment and conclusions of the whole research. Based on the simulations and experiments developed in the thesis, the recommendations and guidelines for further development of diamond turning using nanoscale multi-tip tools are introduced.

Chapter 2 Literature review

2.1 Introduction

In this chapter, a detailed review of diamond turning techniques using micro- and nanoscale diamond tools is given together with the identification of the theoretical and experimental challenges preventing the standardization and commercialization of nanoscale multi-tip diamond tools. In the following sections, the current research progress and the technical challenges regarding the study of FIB-induced damage in diamond are introduced.

2.2 Diamond turning of micro- and nanostructures

2.2.1 Diamond as a cutting tool material

Nowadays, many types of tool materials, ranging from high carbon steel to ceramics and diamond, are used as cutting tools in today's metalworking industry. Single crystal diamond has excellent characteristics in these respects such as high wear resistance, low affinity with a wide range of materials, extreme high strength and hardness, and being fairly easily worked to a sharp cutting edge, making it an ideal tool material for ultra-precision machining.

Diamond is a carbon allotrope in which each carbon is covalently bonded to four other carbon atoms at a distance of 1.545 Å forming a tetrahedral geometry. Some physical and chemical properties of diamond materials commonly used in cutting tools are summarized in Table 2-1.

Table 2-1: Some physical and chemical properties of diamond materials used in cutting tools

Property	Single crystal diamond (SCD)	Chemical vapour diamond (CVD)	Poly-crystal diamond (PCD)
Density (g/cm^3)	3.52	4.1	3.51

Hardness (kg/mm^2)	~10,000	~ 8,000	~ 9,000
Young's Modulus (GPa)	1,223	800	1,180
Tensile strength (MPa)	1,050–3,000	1260	450–1,100
Compression strength (GPa)	8.68	7.4	16
Thermal conductivity (w/(m ƙ))	1,000–2,200	560	750–1,500
Thermal expansion coefficient (cm^2/s)	5.5–11.6	2.7	2.8–11.6

Natural diamond is commonly used to make single crystal diamond tools. According to the form and the amount of the dominant defect/impurity (mostly nitrogen) that may contain, the natural diamond is briefly classified into several categories as shown in figure 2-1. Diamonds that have a large fraction of nitrogen are classified as type I, whereas those that are largely free of nitrogen impurities are classified as type II. Type I diamonds can be further classified into Ia if the nitrogen exits in an aggregated form or as Ib if the nitrogen exists as single substitutional atom. Type II diamonds are sub-classified into types IIa and IIb based on the boron-containing level. Most natural diamonds belong to the subdivision type I. Additionally, since the first recorded synthesis of diamond was performed by Hannay in 1880, several methods of producing diamond have been explored to date such as high temperature high pressure synthesis techniques (HTHP) [37], chemical vapour deposition (CVD) [38, 39], and nanodiamond synthesis techniques [40, 41]. These progresses in fabrication of synthetic diamond increase the use of diamond as cutting tools and its potential applications in optical and electronic devices [42-46].

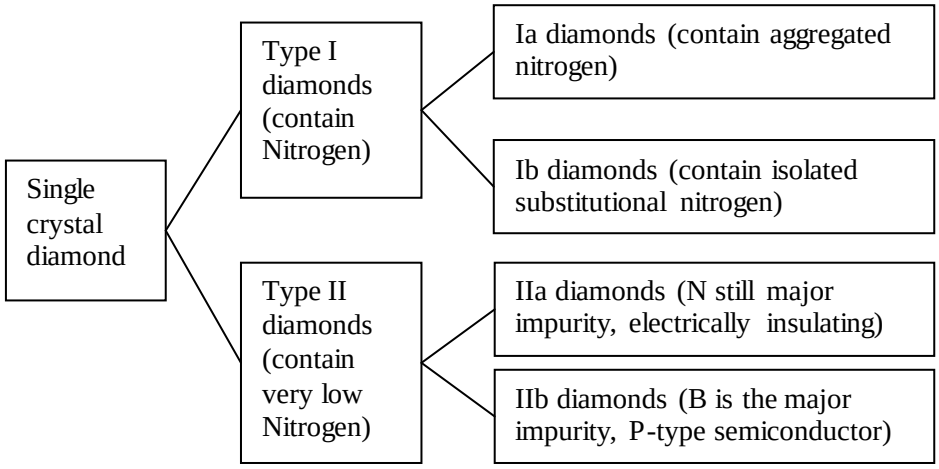

Figure 2-1: The classification of the natural diamond.

2.2.2 Major shaping techniques for diamond tools

Currently the major shaping techniques for diamond tools include mechanical polishing [47], precision mechanical grinding [48], and micro electro discharge machining (μEDM) [49]. Because of the inherent characteristics of the extreme hardness and compositional homogeneity of diamond, it is extremely difficult to fabricate micro/nanoscale diamond tool possessing complex geometry by routine micromachining techniques [47, 50].

In recent years, focused ion beam (FIB) milling technique has been applied in the fabrication of micro/nanoscale diamond cutting tools [32-34, 51-58] owing to its suitability for top-down fabrication (down to submicron level or even down to a few nanometres level). The major advantages of using FIB milling technique for the production of micro-/nanoscale diamond tools lie in its capability for mask-less processing various tool shapes with a high feature resolution as well as observation of a cutting tool during FIB milling process [32, 53]. It can achieve high precision material removal from a specified location in a controllable mode, and it is adaptive for various tool materials and geometries of substrates.

2.2.3 Diamond turning of structured surfaces by single tip diamond tools

Single point diamond turning (SPDT) technology has originated as diamond machining in the 1950s and was originally designed to fabricate metal optics at macroscopic dimensions.

The cutting motion is generated by the rotation of the workpiece, while the tool is guided in relation to the surface, producing the desired surface topography based on the transfer of the tool profile and its working envelope. The cross-sectional shapes of structures are either determined by the geometry of the diamond tool (profile turning) or by the modulation of the infeed depth (form-turning) [24]. Thus, the technique extremely relies on high accuracy of both machine tools motions and tools profiles transferred onto workpieces.

Today, several kinds of advanced SPDT techniques, such as slow tool servo (STS) machining and fast tool servo (FTS) machining, have been applied as deterministic methods for the manufacture of micro components and complex micro-structured surfaces with unique accuracy and cost effectiveness. In these methods, the depth of cut is dynamically modulated according to the radial and angular position of the cutting tool on the work surface. The synchronous multi-axes motion control (at least three numerically controlled machine axes) is a key to machining structures without rotational symmetry.

2.2.3.1 Fast tool servo

The fast tool servo (FTS) technique is widely used for diamond machining functional structured surfaces such as micro prisms, lens arrays, torics and off-axis aspherics [59]. The FTS generates high frequency movement of a cutting tool in the Z-axis (figure 2-2 (a)) based on the desired surface and the machine axes positions. According to the drive mechanism of actuators, FTS can be classified into hydraulic FTS, piezoelectric FTS, magnetostrictive FTS, Lorentz Force FTS, and normal-stress electromagnetically-driven FTS [60]. These systems have strokes from several to a few hundred micrometers with frequencies from 20 Hz to 2 kHz. Normally, FTS with high frequency response always have short strokes, and FTS with

large strokes always have low frequency response and relatively low accuracy.

Recently, Brinksmeier *et al.* [61] developed a novel concept for FST, the nano Fast Tool Servo (nFTS), featuring a stroke of up to 500 nm at a bandwidth of 5 kHz or more. The designed nFTS can generate a variation of the undeformed chip thickness within nanometer range enabling the processing of diffractive micro-structures (figure 2-2). The quality of these diffractive optical elements depends on the design of holograms, the nFTS data pre-processing, the piezo actuator and the workpiece material.

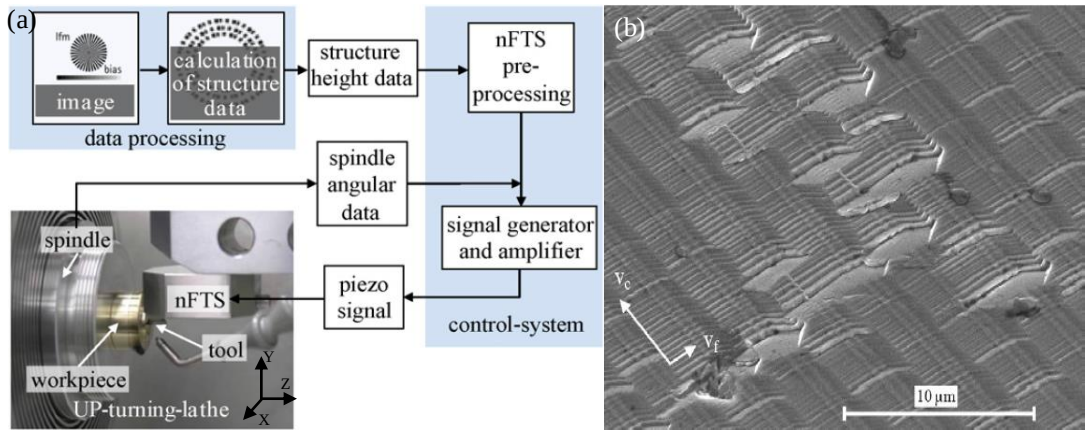

Figure 2-2: The nFTS assisted diamond machining of diffractive optical elements. (a) nFTS control system and data processing sequence. (b) Diffractive surface generated by nFTS in nickel silver (SEM) [61].

2.2.3.2 Slow tool servo

Slow tool servo (STS) is a type of turning method in which the cutting tool mounted on Z-axis oscillates backward and forward while the X and C-axis maintain constant speed [62]. Unlike the FTS method, the oscillation of the cutting tool in a STS system is generated by the Z-axis slide. In a typical STS machining, all axes are under fully coordinated position control. The spindle is controlled using the precision direct current motor, and X and Z-axes are controlled by the linear motor.

STS machining is an efficient method to fabricate freeform surfaces and structured optics [59,

63-65]. In order to achieve high accuracy of the surface profile, the errors of cutting tools are pre-compensated into the tool path/trajectory. In recent decades, numerous research works have focused on the surface generation methods, the machine dynamics, the error analysis and compensation [66-68].

Fang *et al*. [64] has used a cylindrical machining method (figure 2-3) to design the cutting path. A comprehension of cutting tool which considers the tool nose radius and clearance angle, is proposed to achieve the required freeform profile. Yin *et al*. [67] investigated the 3D surface generation in STS machining and analyzed the form error of off-axis paraboloid caused by tool centering error. Zhang *et al*. [69] proposed a coordinate transformation method in STS machining of off-axis aspheric mirrors. Figures 2-3 (b)-(e) show typical freeform surfaces produced by STS machining. However, currently it is still difficult to machine off-axis aspheric mirrors with a large ratio of sag height to diameter because of the inherent limit of tool interference in STS machining.

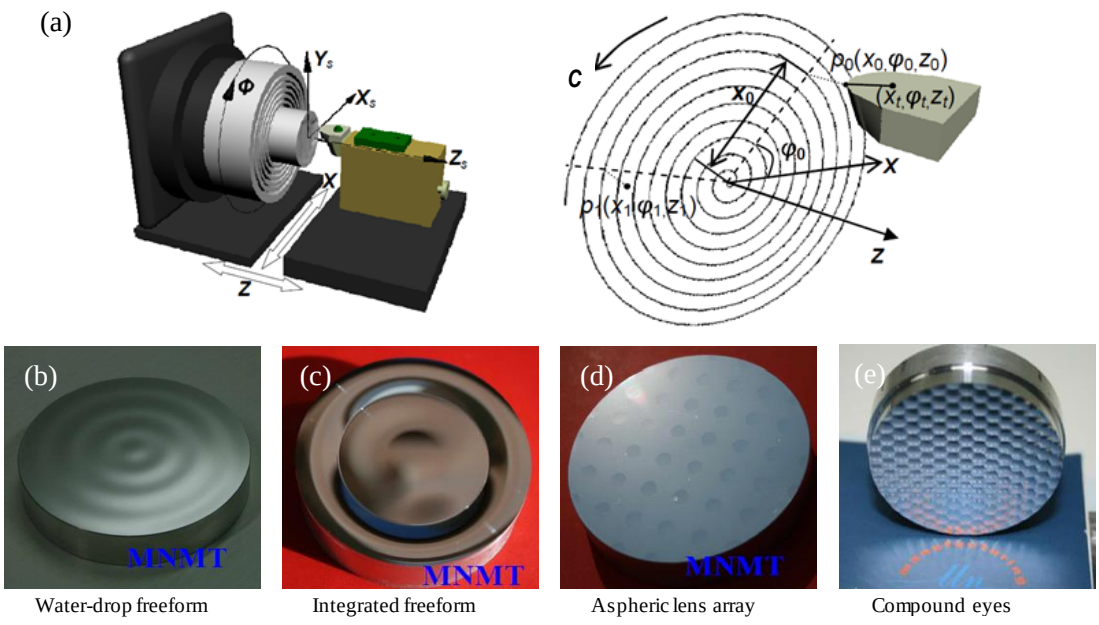

Figure 2-3: STS machining freeform surfaces and structured optics. (a) Cylindrical coordinate machining method; and (b)-(e) are typical freeform surfaces produced by STS diamond machining [59, 64].

2.2.4 Diamond turning using micro multi-tip tools

Using FIB processed multi-tip diamond tool in diamond turning is another approach to generate structured surface. The pioneering work by using this approach was done by Friedrich and Vasile *et al*. [52, 55-57]. They used FIB milling to produce nominal 25 μm diameter micro tools used on an ultra-precision machining centre. A procedure of obtaining sharp cutting edge was proposed as schematically shown in figure 2-4 [70]. Because of the Gaussian ion beam intensity profile, the cutting edge near the ion beam is rounded off and other edges away from the beam become sharper [52, 56].

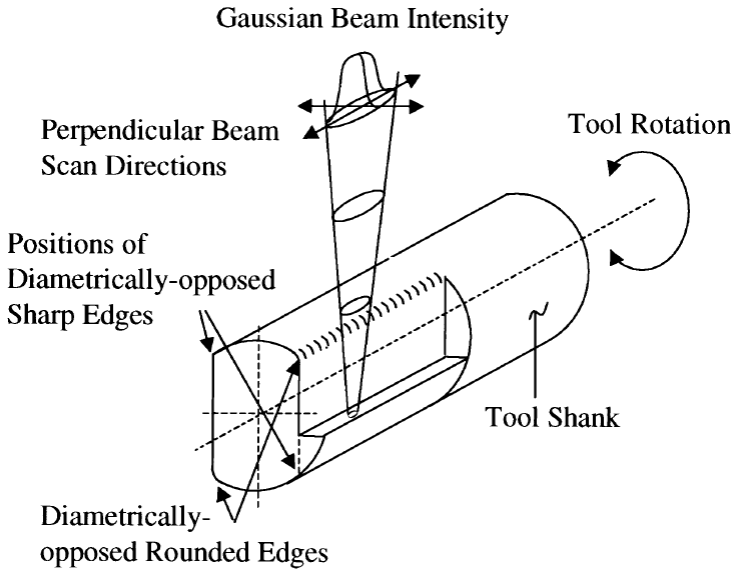

Figure 2-4: Schematics of cutting edge formation [70].

Adams *et al*. [32] from Sandia National Laboratories (SNL) presented the method of FIB shaping micro-scale tools (with dimensions in a range of 15–100 μm) analogous to a cutting tool used in lathes. They proposed a procedure for shaping a two-tip micro cutting tool (as shown in figure 2-5). The cutting tools having rectangular, triangular, and trapezoid shape were successfully fabricated by FIB. Among the tested tool materials, diamond and tungsten carbide materials are easier to form a sharp cutting edge than high speed steel. These tools were further applied for ultra-precision machining of microgrooves, microcoils, and

curvilinear structures (as shown in figure 2-6).

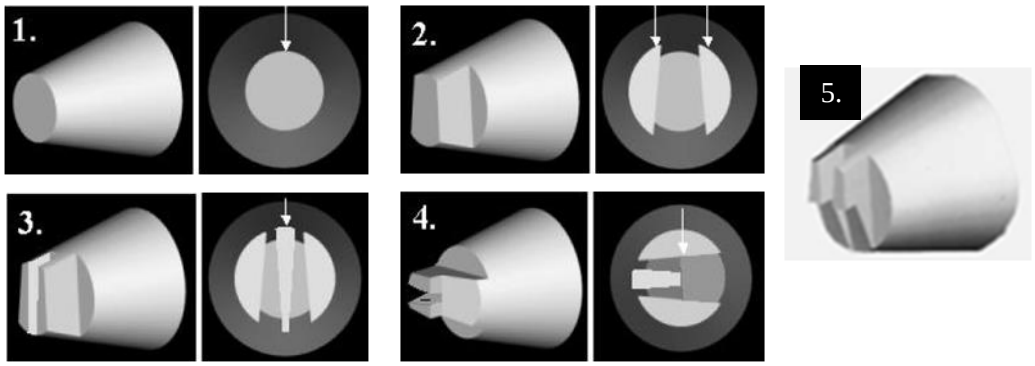

Figure 2-5: The procedures for FIB milling a micro-threading tool. For all sputter steps, a tool is fixed, and the arrows indicate the direction of the ion beam [32].

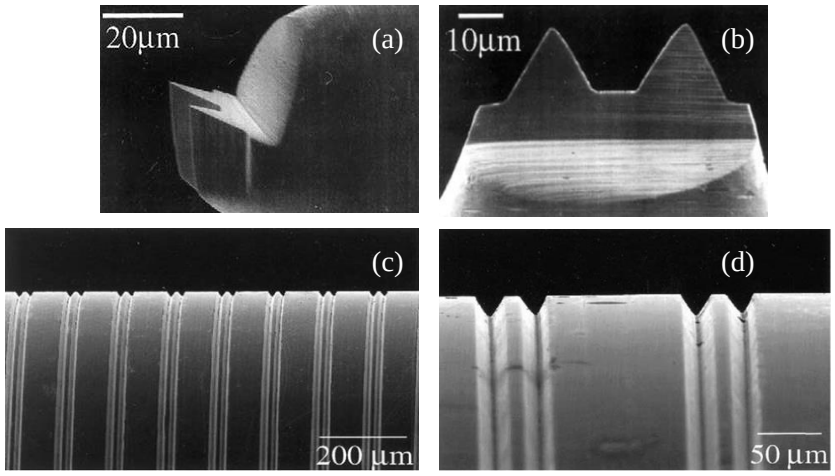

Figure 2-6: FIB shaped two-tip micro tool having triangular cutting faces and the machined micro-grooves. (a) and (b) show the tool tips; (c) and (d) show the machined grooves on PEEK workpiece surface by the two-tip tool [32].

Ding *et al*. [33, 58] evaluated the dependence of machining removal rate and surface morphology of FIB sputtered diamond on FIB processing parameters such as the beam current and the ion incident angle. Their results indicates that a single crystal diamond tool fabricated by FIB under lower beam current of 4.6 nA offers a smoother cutting edge and a better tool surface quality as compared to that generated at a current of 20 nA [33]. More

recently, Fang and his co-workers [34, 51] developed semi-circular micro tools and diffractive optical elements (DOE) shaped micro tools to fabricate micro-DOE (MDOE) which are widely used in solar condense lenses, infrared sensors, laser beam shaping, and high performance optical imaging systems. The measured radius of cutting edges of the micro tool was approximately 25 nm [34]. The DOE-shaped micro tool and the machined MDOE are shown in figure 2-7. Their investigation demonstrated the high efficiency of using micro tools in fabricating micro-DOE with nanoscale surface finishes.

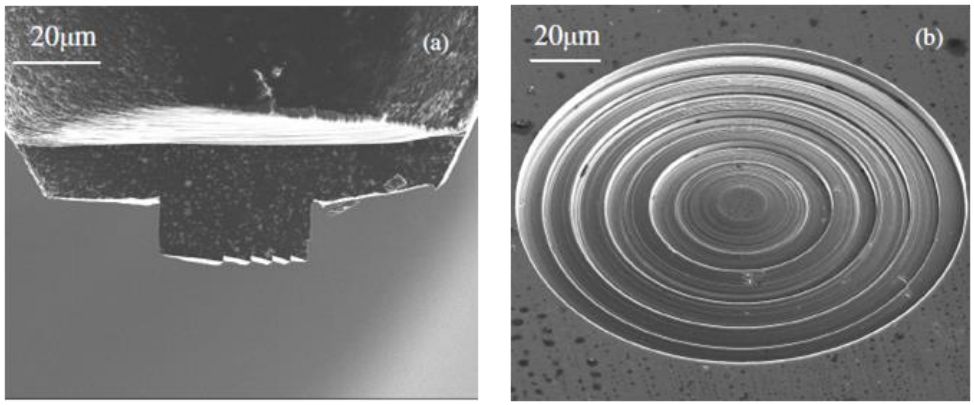

Figure 2-7: SEM images of MDOE fabricated by a DOE-shaped micro tool. (a) DOE-shaped micro tool by FIB, (b) MDOE machined by the DOE-shaped micro tool [34].

2.2.5 Development in the fabrication of nanoscale multi-tip diamond tools

Despite the great progress made in the fabrication and application of micro tools, fabrication of nanoscale diamond tools with high precision and complex tool geometries using FIB milling technique remains challenging. This is mainly due to the five main issues as discussed below.

A. The sample characteristics

In a typical FIB milling process, the target characteristics such as composition, hardness, electrical conductivity, and geometrical feature have huge effects both on the sputtering yield and the machined structural geometry. Since the diamond used for a cutting tool is usually

non-conductive, the additional electric field generated on diamond surface during FIB machining process will deflect the incident Ga ions and/or reduce their energies, which greatly deteriorates the machining efficiency and accuracy.

B. Spatial extension of the ion-induced defects

The exposure of material to ion beam will result in the creation of ion-induced damaged layer and the additional implanted ions in the target matter. These effects are evidenced and play a major role in high-resolution patterning where the incoming spot size is matching the characteristic length of collisional cascades (normally around 10 nm).

C. The redeposition effect

During FIB sputtering process, some of sputtered atoms will attach to the sidewall and also the machined surface. The redeposition is inevitable and will result in the reduction of material removal rate and the creation of unwanted features, making it difficult to accurately fabricate 3D structures with high aspect ratio and surface finish. The FIB milling diamond tools process requires appropriate scanning strategies to avoid or suppress material redeposition on areas of interest as much as possible.

D. Ripples generated on facet

It is well known that energetic ion bombardment of solid surface will create periodically modulated structures which are often referred as ripples [71]. The ripples created on a diamond tool surface will increase its surface roughness and degrade the surface quality of machined nanostructures.

E. The beam tail effect

The beam tail effect is generated due to approximately assumption of Gaussian distribution of the ion beam. In FIB processing the beam profile is usually considered as a Gaussian distribution with a circular cross section. The extra ion dose would remove extra material at the sputtering area. The contributions of beam tail depend on the beam spot size and the pitch between adjacent scanning pixels [53]. This beam tail effect will significantly degrade the form accuracy of nanoscale diamond tools.

In recent years, several theoretical and technical measures have been attempted to improve the form accuracy of FIB machined 3D nanostructures. Various two-dimensional and three-dimensional surface topography predication models for ion beam machining have been proposed to evaluate ion sputtering yield, and to provide references for FIB operators (as summarized in Table 2-2). Moreover, Monte Carlo (MC) method has been developed to simulate time-independent cascade processes, and most commonly used software are SRIM/TRIM [72, 73] and TRIDYN [74, 75]. To improve the form accuracy of machined structures, several slicing strategies of three-dimensional structures have also been proposed, including the depth control method, slice by slice method, and continuous slicing method (as shown in figure 2-8).

Table 2-2: Topography simulation codes for FIB machining [36]

Simulation Code	Dimension	Topography model	Redeposition
COMPOSITE	2D	String-based	Yes
DINESE	3D	Huygens' Principle	No
FIBSIM	2D	Cell-based	Yes
Ionshaper	2D, 3D	Huygens' Principle	Yes
AMADEUS-2D	2D	String-based	Yes
AMADEUS-3D	3D	Cell-based	Yes
AMADEUS-Level set	2D	Level set method	Yes

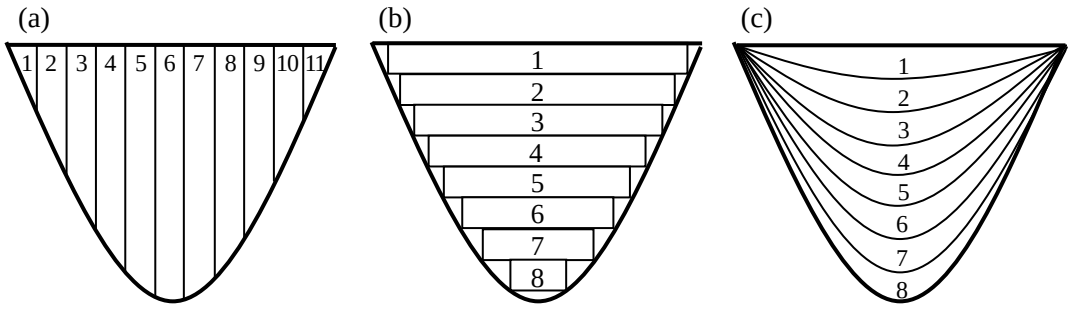

Figure 2-8: Three different methodologies for producing a 3D shape. (a) Depth control method: sputtering by changing the dwell time on the pixel, (b) 2D Slice-by slice method:

sputtering the sequential 2D slice-by-slice, and (c) continuous slicing method: modified by repeating Fu's method by continuously reducing the ion dose for each slice, whereas the total ion dose is the same as Fu's method [76].

Most recently, Sun *et al*. [36, 53] proposed a divergence compensation method to facilitate FIB machining of ultra-precision 3D structures. Through adjusting key fabrication parameters such as dwell time distribution, scanning passes, scanning pitch and scanning strategy, they successfully fabricated a nanoscale diamond cutting tool with nanoscale periodical chisel structures on the tool tip as shown in figure 2-9. A surface roughness Ra of 1 nm was obtained on both the clearance facet and the rake facet. Initial results of using the nanoscale multi-tip diamond tool in the scratching of nano-grating arrays on an electroless nickel substrate show a high machining efficiency. The material removal rate was proved to be 30,000 times higher than purely FIB machining with ion current of 1 nA when machining these nanostructures [53].

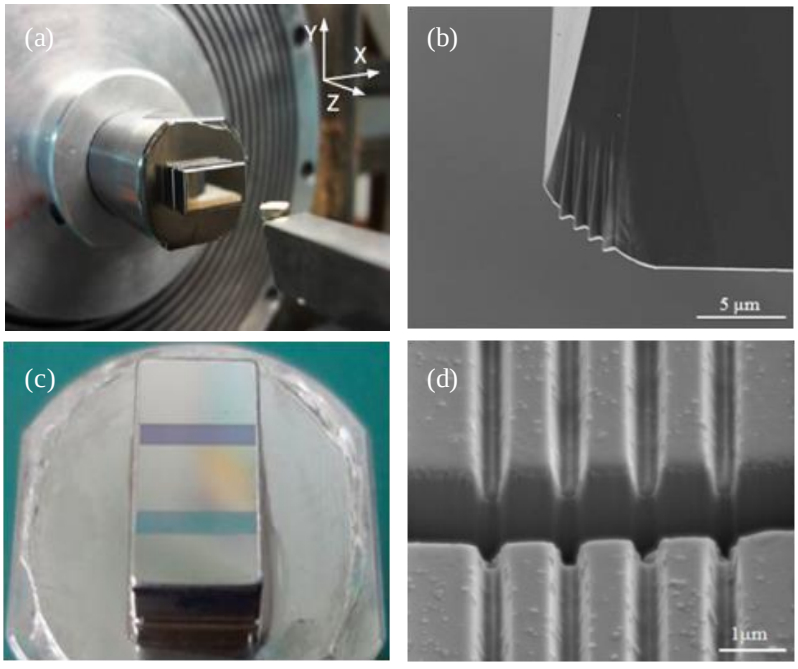

Figure 2-9: Diamond machining of nano-grating arrays using a nanoscale multi-tip diamond tool. (a) Experimental setup of the SPDT test; (b) SEM image of the nanoscale multi-tip

diamond tool; (c) nano-grating arrays fabricated in two regions on the Nickel sample surface; and (d) the cross-sectional view of the machined nano-grating arrays [53].

2.2.6 Challenges in applying nanoscale multi-tip diamond tools

As discussed above, in recent decades, attempts have been continuously made to improve the form accuracy of the micro- and nanoscale diamond tools fabricated by FIB. The results of these cutting trials initially demonstrated the feasibility of using nanoscale diamond cutting tools to increase the complexity and ultimate dimensional resolution of diamond-machined products. However, the development of a systematic theory on diamond turning using nanoscale multi-tip diamond tools is relatively lagging behind. To fully characterise this technique, there are four main issues which need to be addressed.

2.2.6.1 Nanocharacterisation of ion-induced damage in diamond tools

FIB milling technique is an effective means of fabricating micro- to nanoscale tools by sputtering diamond tool on a nanometre scale. However, this method leads to the implantation of ion source material and the creation of atomic defects in target material. For nanoscale diamond tools fabricated by FIB, the ion-induced damage at the near surface of cutting edges can significantly influence the tool cutting performance. Hence, an in-depth understanding of the ion collision process and the ion-induced damage in diamond under different irradiation conditions is required in order to develop a FIB machining strategy to obtain defect free nanoscale diamond tools. An introduction of FIB technique and a review of current research progress and technical challenges regarding the study of FIB-induced damage in diamond will be presented in section 2.4 and 2.5, respectively.

2.2.6.2 Revealing machining mechanism for nanostructures

While using a nanoscale multi-tip cutting tool, the nanostructures are synchronously generated through a single cutting pass. The material removal process in a nanoscale

multi-tip tool cutting will be different from that of using a single tip cutting tool. In-depth understanding of the nanostructure formation process during multi-tip tool cutting is a necessity to further improve the nanomanufacturing capacity of this technique.

2.2.6.3 The shape transferability of nanoscale multi-tip diamond tools

Although a few reports can be found in the literature which preliminarily described the high form accuracy and throughput offered by the multi-tip tool cutting, no experimental or theoretical research work has been carried out to investigate the dependence of the form accuracy of machined nanostructures on the tool geometrical parameters. The practical limits of the feature size and pitch of nanostructures, which is transferred by a nanoscale multi-tip tool profile, remain unclear. The characterization of tool geometry-dependent shape transferability in this technique is needed for future standardization and commercialization of nanoscale multi-tip diamond tools.

2.2.6.4 Processing technology of multi-tip tool cutting

Currently, the effects of machining parameters on the integrity of machined nanostructures and tool wear remain unknown. As the tools and the machined structures are in a range of sub-microns or even dozens of nanometres, even tiny (nanometre level) machining defects can degrade the form accuracy and the integrity of machined nanostructures. Additionally, the mechanism of tool wear and the tool life criteria in nanoscale multi-tip tool cutting have not yet been established. In-depth understanding of the machining process, especially knowing the nanomanufacturing capability under different cutting conditions is of great significance to full exploration and the advancement of this technique.

2.3 Modelling of micro- and nanoscale diamond cutting

Currently, it is still difficult to realize in-process observations and measurement in micro- and nanoscale machining processes. The complexity of the cutting process such as the

elastic/plastic deformation, fracture with high strain rates, and the variation of material properties during the process etc., makes it extremely difficult to use the analytical modelling (based on kinematics from empirical observation) to understand the material behaviour at the this level. On the contrary, computer based numerical simulation method can offer a reasonable insight into material behaviours and assist further empirical research and understanding of the process.

In recent decades, numerical simulation method has been continuously developed as a complementary tool for the study of micro- and nanoscale machining. In these simulations the materials are modelled either from a continuum point of view or from a discrete point of view. The simulation methods are classified as finite element method (FE simulations, for large systems) based on continuum mechanics (CM), and the molecular dynamics method (MD simulations) based on the forces acting between the particles at a molecular level. More recently, multi-scale modelling techniques combining the merit of FEM and MD have been proposed. The corresponding length scales of these methods are illustrated in figure 2-10 [77]. These methods are good compliment to experimental approaches if they are applied correctly. The advantages and limitations of these approaches are discussed below along with examples of recent research progress.

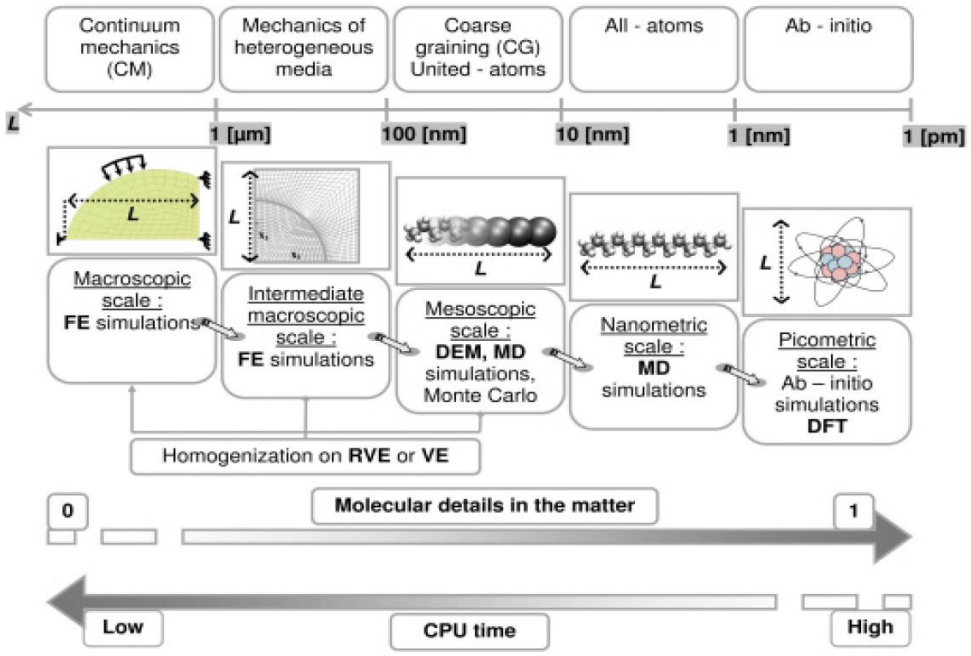

Figure 2-10**:** Various techniques for the numerical simulation of matter with their corresponding characteristic length scales *L* (VE = volume element; RVE = representative volume element; DEM = discrete element method; DFT = density functional theory) [77].

2.3.1 FEM modelling

Finite element modelling is based on principles of continuum mechanics in which the materials are seen as a continuous and homogeneous medium. The material properties are defined as bulk material properties by means of experimental tests. It is a popular simulation technique in macro machining where the heterogeneities of the work materials are often neglected, allowing one to simulate large systems (of the order of meters) and in long time scales (of the order of seconds). However, it has limitations for accurately describing micro- and nanoscale machining when the material behaves discontinuously during machining. Nevertheless, in most cases of isotropic micromachining, FEM can still be an attractive modelling method because the process can be reasonably treated in continuum space. As an example shown in figure 2-11, fundamental variables such as stresses, strains, strain-rates, temperatures can be well predicted by finite element analysis [78].

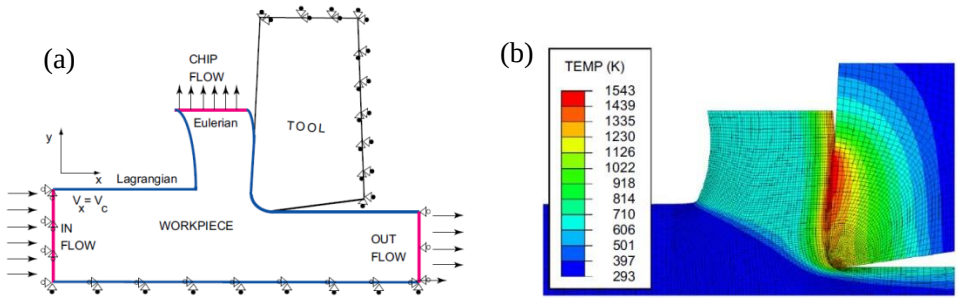

Figure 2-11: (a) FE simulation model with Eulerian boundary condition, and (b) the simulated temperature field [78].

Recently, for micro cutting, Liu *et al.* [79] built a strain gradient plasticity based finite element model to examine the size effect caused by tool edge radius in orthogonal micro-cutting of Al5083-H116. They pointed out that cutting edge radius contributes to the size effect by changing the material flow pattern and increasing the tool-chip contact length. The strain gradient effect is dominant at low cutting speeds, small uncut chip thickness, and negligible tool edge radius. However, the model cannot provide any further information on the material crystal distortion and phase transformation which are important to the understanding of micro- and nanoscale machining.

Moreover, some researchers have proposed to develop a representative volume element (RVE) which can consider the heterogeneities of materials [80-82]. The RVE is theoretically viewed as the smallest volume containing all information about the distribution and morphology of the heterogeneities in target materials such as crystalline phase and amorphous phase. At the macroscopic level, the work material is then idealized as a continuous and homogeneous medium from the mean mechanical behaviour of the RVE. However, this model is limited by the hypothesis of the continuity of the matter and the formalism based on continuum mechanics and macroscopic thermodynamics [77]. More recently, in order to solve the excessive element distortion when modelling micro cutting, a mesh-free Lagrangian numerical method named smoothed particle hydrodynamic (SPH) has been developed and extensively used to deal with multi-body dynamics and computational

fluid mechanics [83]. Recent advance in FEM modelling of micro cutting can be found at [84].

2.3.2 MD modelling

The molecular dynamic (MD) simulation technique, developed by Alder and Wainwright in the late 1950s [85], is based on interatomic force calculations defined by potential functions. It can describe the characteristics of material at micro- and nanoscale such as crystalline structure, atomic defect, dislocation, and crack etc. In early 1990s, Belak [86], Inamura [87, 88], Shimada [89, 90], Ikawa [91, 92] and Komanduri [93, 94] pioneered the framework of MD simulation of nanometric cutting which was followed by Luo [95] and Ye [96] etc. in early 2000s. Since then, many researchers have been continuously devoted to the MD simulation research of nanometric cutting. These studies have made a great contribution towards the in-depth understanding of the dynamic behaviour of materials under different nanometric cutting conditions.

Belak and co-workers [86] carried out MD simulation to simulate the tribological process in orthogonal cutting of copper (1 1 1) surface and the silicon (0 0 1) surface. The work of Inamura *et al*. [87, 88] focused on the energy dissipation and material deformation at shear zone through MD simulation**.** Their simulation linked the intermittent drop of potential energy of workpiece with the plastic deformation of workpiece and heat generation as well as impulsive temperature rise on the tool rake face. They also reported the stress distribution in the workpiece during the cutting process.

Shimada *et al*. [90] simulated the nanometric chip removal process in micro cutting of copper and qualitatively compared it with experimentally determined values. The comparison showed a good agreement of the chip morphologies, the cutting force, and the specific energy. They also pointed out that MD simulation method can be used to analyse the thermal field in metal cutting by employing a suitable scaling of thermal conductivity. The ultimate surface roughness that can be achieved by SPDT was estimated to be 1 nm for both

monocrystalline copper and polycrystalline copper [89].

Komanduri *et al*. [94, 97, 98] conducted MD simulations to investigate the effects of tool geometry, crystal orientation, and depth of cut on nanometric cutting, and quantified significant differences of the machining characteristics between ductile metals and brittle materials. They attributed the mechanism of plastic deformation of silicon to a pressure induced phase transformation—from cubic to body centred tetragonal. They also highlighted the difference between macro and micro scale cutting, and identified four stages of the nanometric cutting process: (1) compression of the work material ahead of the tool; (2) chip formation; (3) side flow; and (4) subsurface deformation of the workpiece [94].

Luo *et al*. [95] conducted MD simulation and atomic force microscope (AFM) experiments to study the tool wear in nanometric cutting of silicon, and pointed out that the thermo-chemical wear is the basic wear mechanism of diamond cutting tools. Ye *et al*. [96] studied the effect of cutting speed on the cutting temperature and machined surface. The whole cutting process comprised two steps: material removal process as the tool was machining the surface, and the relaxation of the work material to a low defect configuration after the tool passed the machined region (as shown in figure 2-12).

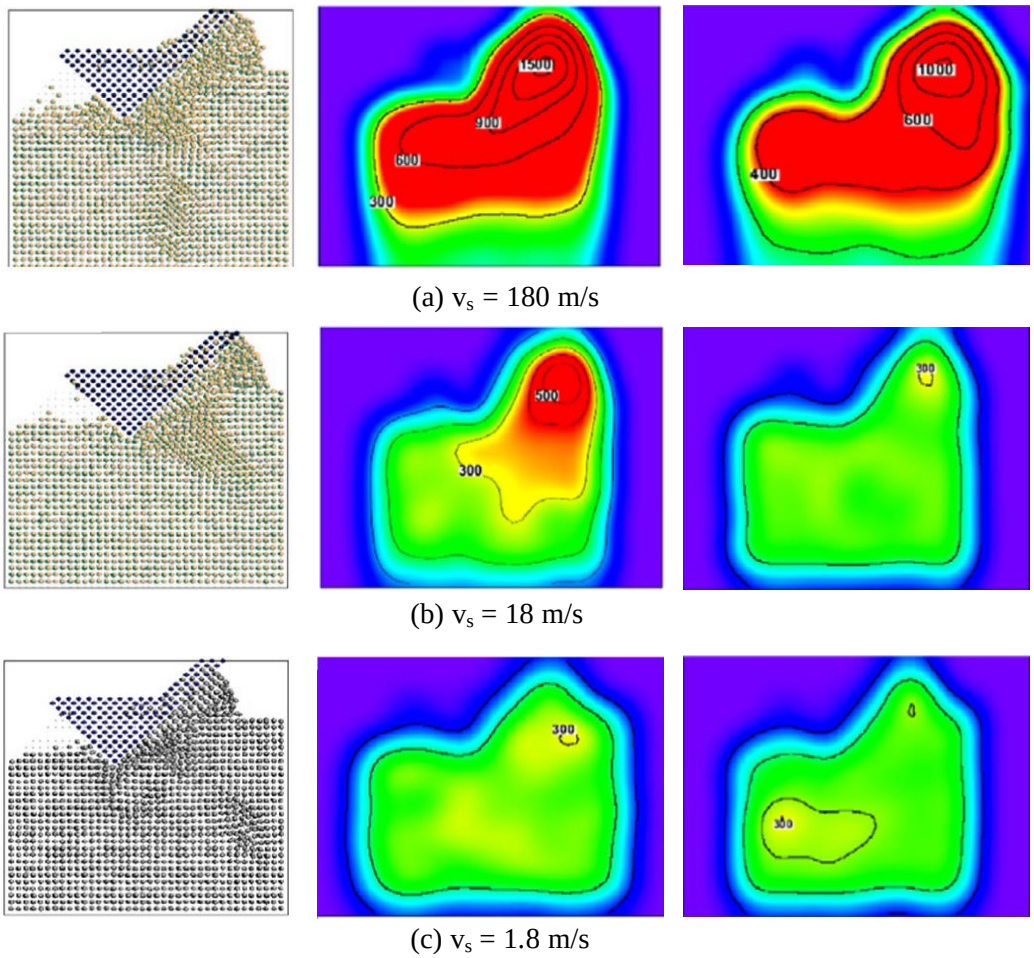

(a) v_s = 180 m/s

(b) v_s = 18 m/s

(c) v_s = 1.8 m/s

Figure 2-12: MD simulation of nanometric cutting of (1 0 0) copper surface with a rigid tool with rake angle −45 ° at cutting speeds of (a)180 m/s, (b)18 m/s, and (c) 1.8 m/s. The left column shows configurations of workpiece and cutting tool; the mid and right columns show the temperature distributions of workpiece before and after 120 ps relaxation, respectively. The depth of cut is 1 nm in all cases [96].

However, due to the limitation of computational power at that time, many MD models have been only applied to simulate two dimensional orthogonal cutting with a very small model size, or unrealistic high cutting speed. In recent years, the development of high performance computer (HPC) helps to enlarge the spatial and time scales of MD simulation. Many researchers have conducted parallel large-scale MD simulation for 3D cutting process.

Fang and his co-workers [99] have identified the frictional coefficient and forces as a

function of the rake angle of the pin shape tool. Kim *et al*. [100] reported that in the nanoindentation and scratching process, the nucleation of dislocations plays more important role in determining the abrupt drop during stick-slip than subsequent propagation of partial dislocations. Yan *et al*. [101] have simulated the multiple scratching processes of using an AFM tip and investigated the effects of the feed rate on the deformation of the machined surface. A deformation criterion relating the single-atom potential energy variation to atom lattice deformation was further explored and the simulation results showed that four states exist between AFM pin tool and the workpiece surface [102].

Moreover, MD models were also built successfully to investigate the role of friction and tool wear in nanometric machining of copper, such as the work done by Maekawa *et al*. [103], Lin and Huang [104] etc. More recently, large scale MD model with model size up to 10 million atoms has been performed by Pei *et al*. [105] to study the size effect existing in nanometric cutting of copper. Using this model, they quantified the effect of processing parameters on cutting force and lattice defects (as shown in figure 2-13) [106].

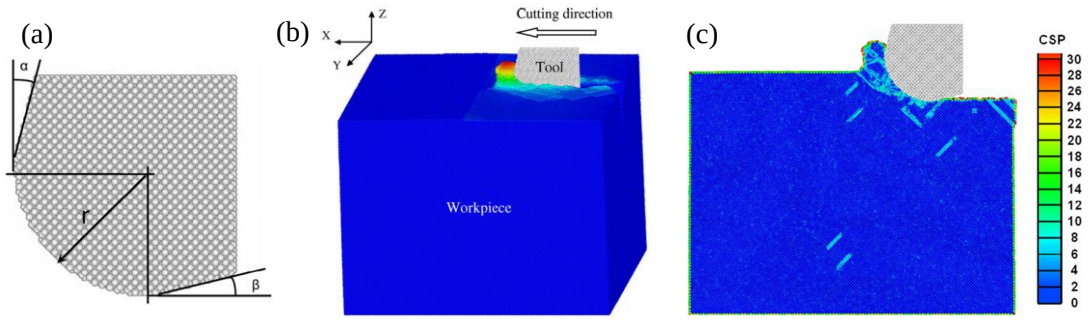

Figure 2-13: The large-scale MD simulation model of nanometric machining. (a) The geometry of the cutting too (tool edge radius r = 6 nm, the rake angle α = 12 °, and clearance angle β = 12 °); (b) nanometric cutting at the cutting distances of 16 nm; and (c) the cross-sectional views of the defects formed during cutting process (the atoms are coloured according to their centro-symmetry parameter (CSP) value) [106].

2.3.3 Multiscale modelling

To bridge the gap between the atomistic and continuum scale, multi-scale simulation methods such as the quasi-continuum (QC) method [107], the macro-atomistic ab-initio dynamics method (MAAD) [108], and the coupled atomistic and discrete dislocation method (CADD) [109], have been developed by hybridizing the FE and MD simulations. Various handshaking schemes used in these methods were reported to be able to reduce the computational cost and thus increase the length scale of simulations. Ever since 1990s, a few multi-scale simulations can be found in the literature to study the micro- and nanoscale machining process.

In 1990s, Inamura *et al*. [87, 88] used multiscale modelling method to study the stress state in the primary shear zone during the nanometric cutting process. Shiari and Miller [110] conducted multiscale simulation to study the details of nanometric cutting of single crystal aluminium including material removal, chip formation, surface evolution, and generation and propagation of dislocations for a wide range of tool speeds (20–800 m/s) at room temperature. Their results demonstrated the power of using the multiscale simulation method in capturing both long-range dislocation plasticity and short-range atomistic phenomena in micro- and nanoscale machining.

Additionally, Aly *et al*. [111] developed a hierarchical modelling method to couple FE and MD. The material properties used to construct a constitutive model were extracted from the stress-strain curve produced by an MD model. This constitutive model was then applied to a regular FE cutting model to evaluate the cutting forces which were required to machine a silicon wafer using different cutting parameters.

Recently, Cheng and Sun *et al*. [112, 113] demonstrated the capabilities of the QC approach in studying nanometric cutting of single crystal copper and aluminium. The effects of rake angle on chip formation and propagation of atomistic dislocations have also been examined (as shown in figure 2-14). Later, Pen *et al*. [114] preformed QC simulations to study the

effects of crystal orientation and cutting direction on the attainable machined surface quality. The results show that cutting on the (1 1 1) surface along the [-1 1 0] cutting direction can minimize the residual damaged layer on the machined surface and thus was recommended in practical applications.

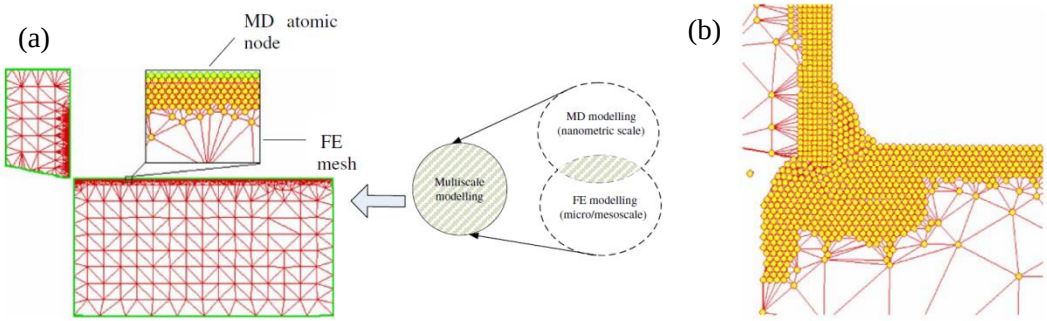

Figure 2-14: (a) Multiscale model for nanometric cutting of single crystal aluminium; and (b) the atom snapshot with motion of the tool at 43rd time step [112].

2.4 Introduction of FIB machining technique

2.4.1 FIB instrument

The FIB technique was developed in the early 1970's by researchers working on liquid metal ion source (LMIS) for use in space (first conducted by Krohn *et al*. in 1961) [115]. The world first FIB instrument based on field emission technology was developed by Levi-Setti [116] and Orloff and Swanson [117]. Nowadays, many dual-beam FIB systems or more advanced FIB instruments incorporate the ion beam column with other analytical or measurement systems such as a scanning electron microscope (SEM), a transmission electron microscope (TEM) or a secondary ion mass spectrometry (SIMS). These dual-beam systems are recognized as the most powerful tools for micro-/nanoscale fabrication and characterization, across many research areas from material science, microelectronics, to biology and life science. A typical dual-beam instrument consists of a vacuum system, a chamber with sample stage, an ion source, an ion column, an electron column, a gas injection

system (GIS), and a computer to control the whole instrument as schematically shown in figure 2-15 [118].

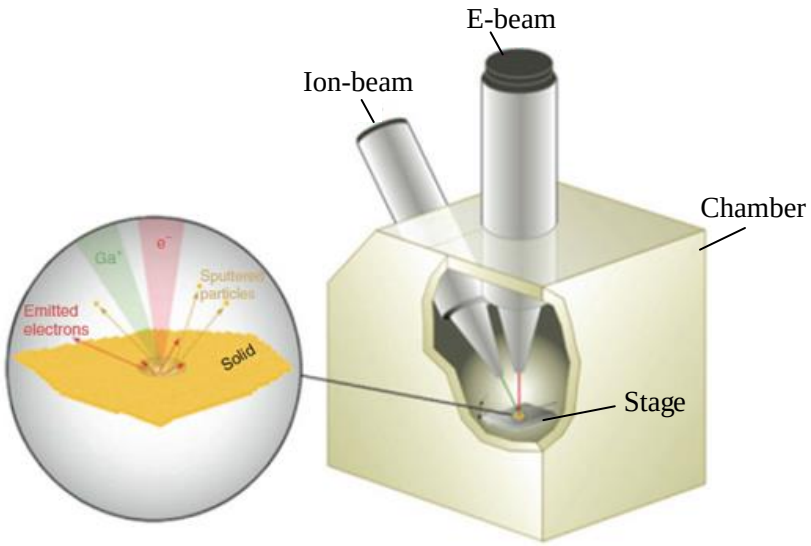

Figure 2-15: Schematic diagram of an FIB-SEM dual beam system [118].

Nowadays, the majority of commercial FIB LMIS systems operating worldwide are suited only for Ga ions due to their advantage in achieving the emitted ion mass spectrum with 99 % singly charged ions at low melting point and vapour pressure. Therefore, no mass filter is needed and the ion column design becomes easier due to the use of electrostatic ion optics, which is mass-independent. To enlarge the application field of FIB to other species than Gallium, alloy LMIS can be applied, but it requires a mass separation system with a selection aperture to choose a certain ion mass and the ion charge state. The two basic configurations of ion optics are schematically shown in figure 2-16 [119]. Currently, the available ion sources include Al, As, Au, B, Be, Bi, Cs, Cu, Ga, Ge, Er, Fe, H, In, Li, Ni, P, Pb, Pd, Pr, Pt, Si, Sn, U and Zn [11]. A comprehensive overview of FIB column designs has been given by Orloff [120].

In the present research project, a FIB/SEM dual column instrument (FEI Quanta 3D FEG FIB) was used to fabricate nanoscale multi-tip diamond tools. The essential specification of the FIB system is attached as appendix I.

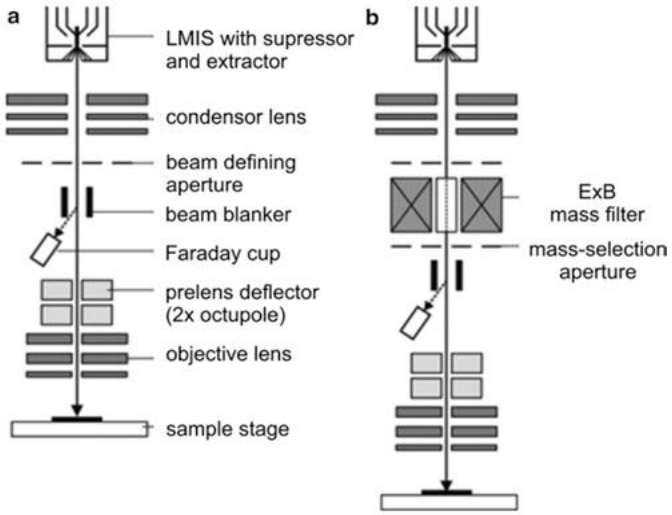

Figure 2-16: Typical FIB column geometry without (a) and with mass-separator (b) [119].

2.4.2 Principles of FIB system

Before operating the ion beam in FIB system, the Ga^+ wets up the sharp tungsten (W) needle and flows to the W tip. A high extraction field (> 10^8 V/cm) is used to pull the liquid Ga^+ into a sharp cone of up to 5–10 nm radius. The emission ions are further accelerated by adjusting the voltage applied on the suppressor. The ion beam energy is typically designed with a range between 5 and 50 keV. By finely controlling of the strength of the electrostatic lenses and adjusting of the effective spray aperture sizes, the beam spot size can be adjusted and the beam current can be varied between 1 pA and 10 nA, allowing fine beam for high-resolution imaging on sensitive samples and a heavy beam for fast rough milling. Moreover, most of the FIB systems are available for delivering a variety of gases in the working stage by a gas jet nozzle assembled inside the working chamber through an appropriate piping system. These gases are used for faster and more selective etching as well as for the deposition of different kinds of materials.

In general, the important fundamental processes of ion beam interaction with materials can be classified as follows: secondary particle generation for imaging and surface analysis, ion implantation, material removal, and gas assisted ion beam etching and material deposition.

Simplified diagrams of these processes are shown in figure 2-17.

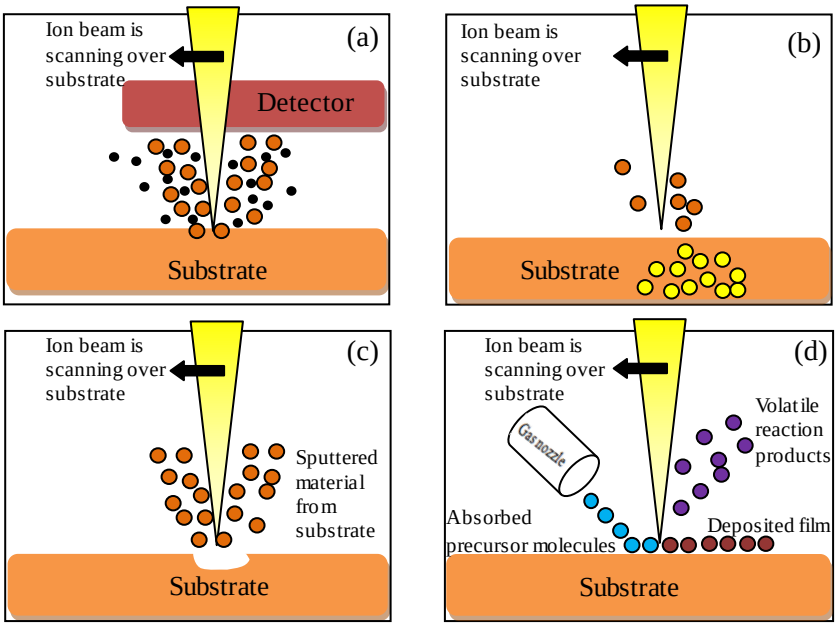

Figure 2-17: Schematics of the important fundamental processes of ion beam interaction with materials. (a) Ion beam topographical imaging; (b) ion beam implantation; (c) material removal; and (d) gas assisted ion beam etching and material deposition. (replotting based on figure 3 in [121]).

2.4.3 Key fabrication parameters in FIB milling

In general, the term 'milling' in FIB processing means 'removal of the target material' which in nature is a combination of physical sputtering and material redeposition. Principally, the FIB milling technique is available to machine nearly all kinds of materials. There is a number of FIB fabrication parameters used to control the operations in FIB instrument such as the adjustment of sample stage, manipulation of the ion beam, and the control of vacuum system and gas jets for gas delivery (as summarized in figure 2-18). In-depth understanding of the effects of these processing parameters on the material removal process can lead to an improvement of the form accuracy of machined structures as well as the machining efficiency. The overview of the optimization of fabrication parameters used in FIB milling

process has been recently given in [36, 122, 123].

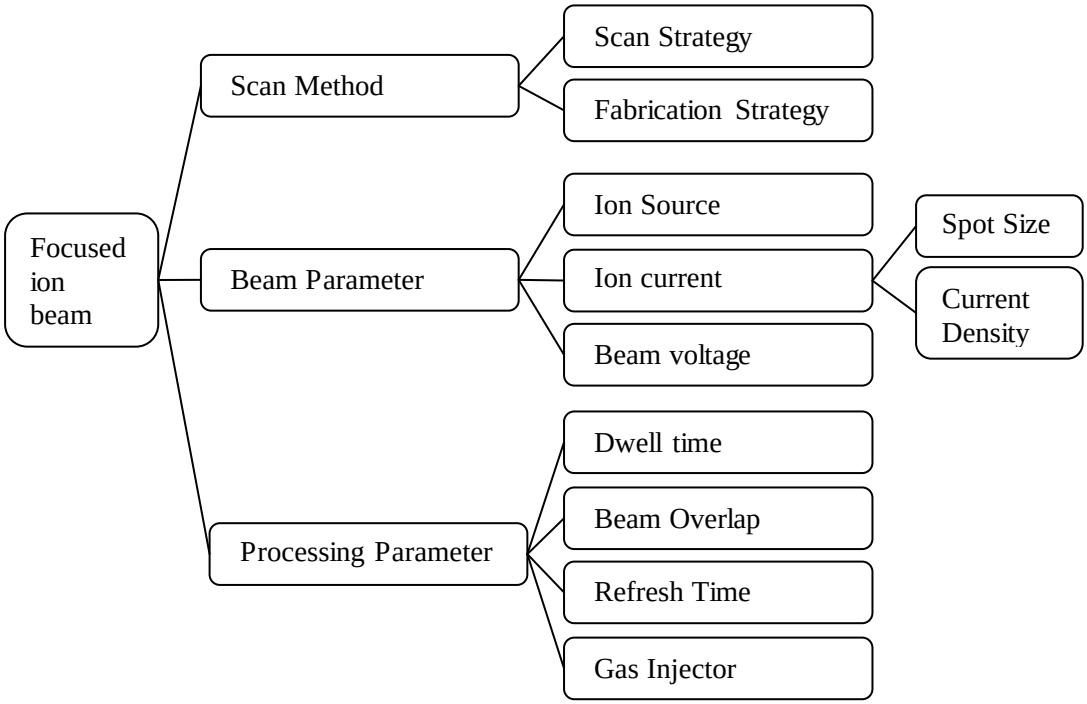

Figure 2-18: Classification of the processing parameters of a typical FIB system (replotting based on scheme 1.1 of [123]).

2.5 FIB-induced damage in diamond material

Although various advanced FIB processing methods for the fabrication of 3D nanostructures have been successfully developed by many researchers, the FIB milling has an unavoidable result in terms of the implantation of ion source materials and the formation of damaged layer at the near surface. These damaged layers can significantly degrade/alter the device performance and limit the applications of FIB nanofabrication technique. Understanding the ion-solid interactions physics provides a unique way to control the FIB produced defects in terms of their shape and location. The theory of ion-matter interaction and the previous investigation on ion-induced damage in diamond will be discussed and reviewed in the following sections.

2.5.1 Theory of ion matter interaction

When an energetic ion strikes the matter, it immediately interacts with the target atoms by transferring energy and momentum. Ions lose energy by means of both nuclear and electronic interactions with the substrate atoms. Depending on the mass of the incident ion and the target atom, and the incident ion energy, the impulse of Coulomb forces might be sufficient to knock out electrons from target atoms resulting in either ionization of the substrate surface or electron excitation process leading to emission of X-rays. The primary nuclear interactions lead to the displacement of the target atoms from their original positions and the creation of vacancies in the target material if the transferred energy exceeds the target atomic-mass-dependent and angular-dependent displacement energy E_d. If the energy transferred to the primary atom 'knocked on' is sufficiently high, the secondary, tertiary and higher order atomic knock-ons take place which refers to the energetic atomic collision cascade as schematically shown in figure 2-19. The displaced atoms may run out from the surface which is known as sputtering. The implantation of the incident ions and the process of vacancy-interstitial creation lead to the disorder of the local crystal structure in terms of condensed matter phase transition, amorphisation, swelling and/or other physical changes depending on the type of target material as well as the ion beam processing parameters.

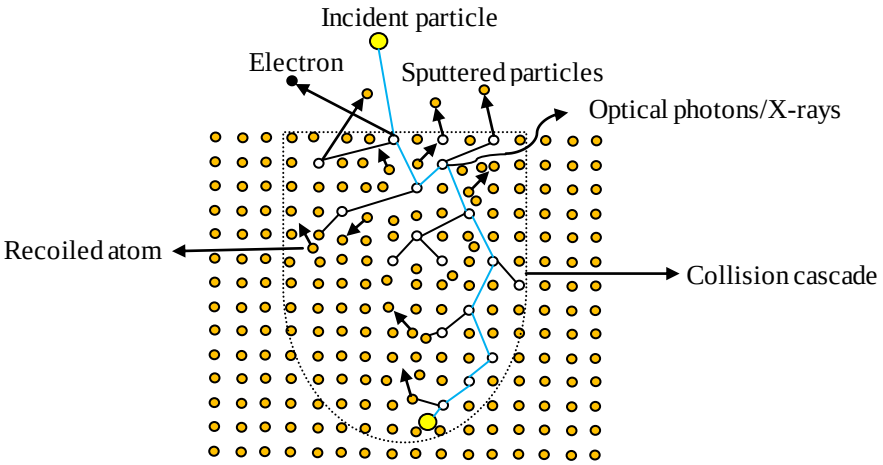

Figure 2-19: Schematic diagram of the various processes that occur during ion-material

interaction.

Briefly the mechanism operating to slow down incident ions and to dissipate ion energy can be classified into three categories: elastic collisions process (nuclear stopping), inelastic collision process (electronic stopping), and charge exchange process. The energy loss process can be expressed as:

$$\left(\frac{dE}{dX}\right)_{loss} = \left(\frac{dE}{dX}\right)_{Elect} + \left(\frac{dE}{dX}\right)_{Nucl} + \left(\frac{dE}{dX}\right)_{ChargeExchange} \quad (2\text{-}1)$$

where $\left(\frac{dE}{dX}\right)_{Elect}$ is loss due to electron, $\left(\frac{dE}{dX}\right)_{nucl}$ is loss due to neutron, and $\left(\frac{dE}{dX}\right)_{ChargeExchange}$ is loss due to charge exchange. Since charge exchange loss represents a small fraction of total energy loss for low charged ions, it can be neglected.

Theoretically, a general way to describe the slowing down of an ion in matter is through the 'stopping power' (–dE/dx) defined as the energy dE lost by an ion per unit path length of an ion on its trajectory dx. Thus the total stopping power can be written as

$$\left(\frac{dE}{dx}\right) = \left(\frac{dE}{dx}\right)_e + \left(\frac{dE}{dx}\right)_n \cong S_e + S_n \quad (2\text{-}2)$$

where S_e is the energy loss due to electron by an ion per unit path length, S_n is the energy loss due to neutron by an ion per unit path length. The nuclear energy transfer occurs in discrete steps as a result of elastic collisions where the energy of the incoming ion is lost to target atoms by momentum transfer. The electronic energy loss occurs as a result of inelastic scattering events where the transfer of energy occurs through electronic excitation.

The electronic and nuclear stopping curves for Ga ion in single crystal diamond calculated by SRIM [73] software are shown in figure 2-20. The stopping power is proportional to the velocity of the ions at low energy regime. It attains a maximum value (around 50 keV) and gradually decreases with the incident energy. However, in the high-energy regime the

electron energy loss dominates the energy transfer process because the velocity of the incoming ion becomes comparable to that of the orbital electrons. The nuclear energy loss is smaller than the electron energy loss and hence it has a negligible contribution to the energy transfer in high-energy regime. For material removed by the collision cascade, the optimized energy is normally in a range of 10–100 keV [124].

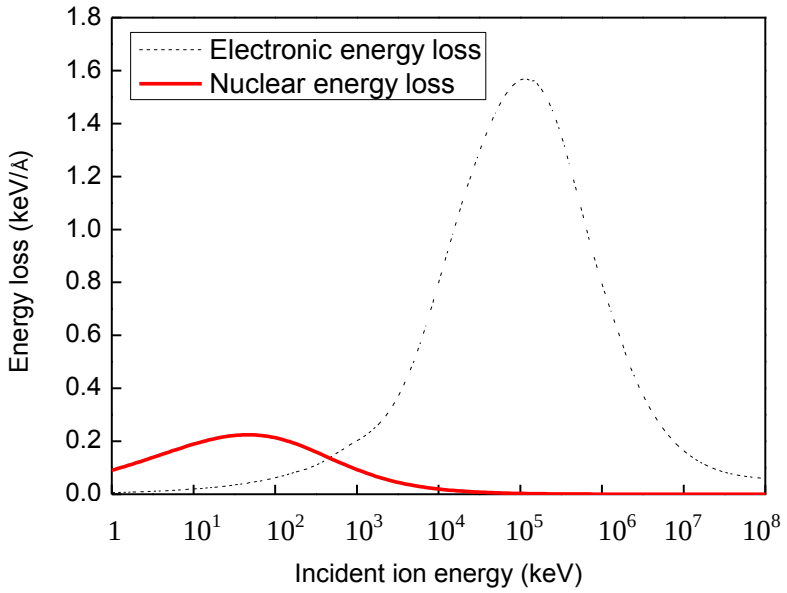

Figure 2-20: The electronic and nuclear stopping curves for Ga ion in single crystal diamond calculated by SRIM (using 52 eV for the displacement energy).

2.5.2 Experimental study on FIB-induced damage in diamond

Before going into detail, it is important to distinguish the LMIS based Ga^+ FIB beam from other high energy ion beams such as the slow highly charged ions (HCI) beam and the swift heavy ions (SHI) beam. Slow highly charged ions are characterized by their low velocity and high potential energy such as Xe^{q+} and Ar^{q+} (q is the charge state). The ions-induced damage such as electron emission [125] and sputtering [126-129] are attributed to the potential energy (the sum of all binding energies of the missing electrons) of slow HCI which is comparable to or considerably higher than the kinetic energy. Swift heavy ions are characterized by their high kinetic energy (several tens of MeV and above) and the ion

stopping in matter is predominated by electronic excitation and ionization processes. The elastic collisions (nuclear stopping) with the target atoms play a minor role and come into play only at the end of the trajectory for energies of a few hundred keV and below. The commercial LMIS based Ga^+ FIB beam normally has a voltage ranging from 2 kV to 30 kV. The ion-solid interaction in a typical FIB milling process is governed by the nuclear energy loss at the surface of the solid [44].

In recent decades, a variety of techniques including Raman spectroscopy [130, 131], optical measurements [132], atomic force microscopy (AFM) [133, 134], scanning electron microscopy (SEM) [134], and transmission electron microscopy (TEM) [45, 46, 135] have been developed to investigate the ion-induced damage in diamond substrates caused by gammas[136], neutrons[137], electrons [138], protons [139] and ions [45, 46, 135] under different scale of energies. There is also a body of work looking at the radiation hardness of diamond in particle detectors for use in high-energy physics [140], nuclear [141] and medical [2] applications. However, due to the inherent differences in the beam species and energies, there are remarkable differences in the characteristics of ion-induced damage when using difference ion beams. Those studies of SHI and HCI beam bombardment of diamond and relevant applications have been reviewed in [142] and will not be introduced in the following section.

2.5.2.1 Formation of a-C and the required critical dose

In typical LMIS based Ga^+ FIB beam milling process, the energy transferred by the incident Ga^+ is usually sufficient to break the C-C bond leading to the displacement of lattice atoms, surface sputtering and creation of craters and hillocks, formation of point defects, and the initiation of other secondary processes. These dynamic effects are transient. When the density of point defect is sufficient high, the displaced atoms may partly re-order into different characteristic arrangements of atoms and a residual damaged layer is formed at the near surface comprised mostly of vacancies and interstitials.

Admas *et al*. [54] has used TEM to study the amorphous carbon (a-C) layer in diamond created by FIB milling. The thickness of the a-C layer varies at different sites on rough surfaces, and a larger amorphous layer was found when a small local incident angle of ion beam was applied. They have further investigated the effect of H_2O on the formation of damaged layer, and found that a reactive sputtering during the H_2O assisted FIB milling process can suppress the formation of damaged layer. A 20% reduction in the thickness of a-C layer was found when using H_2O assisted FIB milling [54].

Brunetto *et al*. [131] studied the ion-induced amorphisation of diamond (CVD diamond) by in-situ Ramon spectroscopy. The energies of impact ions (H^+, He^+, and Ar^+) ranging from 30 keV up to 200 keV were used. Amorphous carbon was formed when a threshold of damage density of 2.0×10^{22} vacancies/cm^3 was reached.

Most recently, in order to further determine the amorphisation threshold for ion implantation in diamond, Rubanov *et al*. [46] investigated the ion-induced damaged layers in a synthetic type1b diamond substrate under eight different doses ranging from 6.0×10^{14} to 1.0×10^{16} ions/cm^2 via a combination of cross-sectional TEM imaging and electron energy loss spectroscopy (EELS) analysis (figure 2-21). The amorphisation threshold for ion implantation in diamond at room temperature was determined to be 5.2×10^{22} vacancies/cm^3. The thickness of the damaged layer grew with the ion dose and achieved an equilibrium value of 44 nm for continuous 30 keV Ga^+ FIB milling [46].

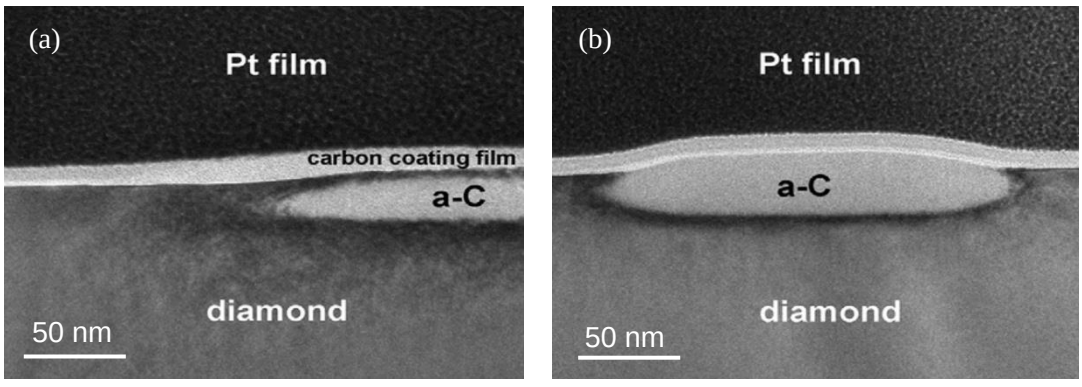

Figure 2-21: Cross-sectional TEM bright field images of the damage regions in synthetic

type1b diamond after 30 keV Ga^+ FIB implantation with doses of: (a) 6.0×10^{14} ions/cm^2 and (b) 6.0×10^{15} ions/cm^2 [46].

Mckenzie *et al*. [45] studied the interactions between a single crystal natural conductive diamond and 30 keV Ga^+ focused ion beam through scanning transmission electron microscopy (STEM), EELS, and electron backscattered diffraction (EBSD). The near surface microstructure varied with the increase of ion dose, and the critical dose for the amorphisition of the diamond substrate was 2.0×10^{14} ions/cm^2. A stable amorphous layer (thickness of 35 nm) was found at a high dose (1.0×10^{15} ions/cm^2) and it swelled up to 31% its original volume in order to accommodate a significant quantity of implanted gallium (figure 2-22). The EELS results further characterized this layer and identified the hydrogen and oxygen contents within the amorphous carbon layer [45].

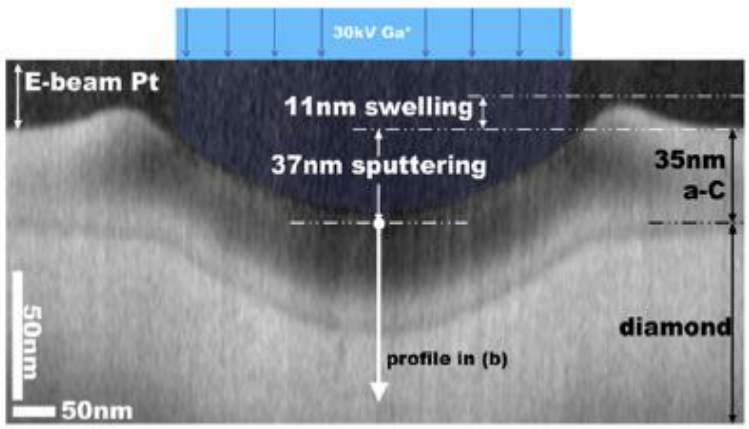

Figure 2-22: Bright field STEM image of a single crystal diamond sample exposed to a dose of 4.2×10^{17} Ga/cm^2 over the area indicated. The image has been electronically elongated in the vertical direction (see scale bars) to highlight the surface profile [45].

2.5.2.2 Effect of implantation of Ga

Apart from the amorphisation in diamond, there might be additional effects which are caused by the implantation of ion source atoms. Adding of ion species into the sample can change the chemical composition, optical, magnetic, electrical, and mechanical properties of FIB

fabricated products.

Gnaser and co-workers [143] reported a fluence-dependent evolution of the implanted Ga concentration in nanocrystalline diamond films by SIMS. A linear increase of the Ga peak concentration with fluence was found up to ~2.0 × 10^{16} ions/cm^2 and the Ga content approached a saturation level at about 2.0 × 10^{17} ions/cm^2.

Hamada *et al*. [140] reported that the accumulation of implanted gallium ions would degrade the stability of applicable electric field of micro structures fabricated in an undoped diamond substrate. They proposed a process, combining a high temperature annealing in high vacuum and a following chemical treatment with acid and alkaline solutions, to remove the implanted Ga atoms.

Similarly, Philipp *et al*. [144] observed Ga segregation in FIB modified tetrahedral amorphous carbon (ta-C) films. Due to the phase separation of Ga and C, the implanted Ga was segregated at ta-C surface, and the Ga droplets were transformed into spherical shaped dots at a high temperature (above 300 ℃). The size and the height of Ga dots segregated on the surface increased with the increase of annealing temperature (as shown in figure 2-23).

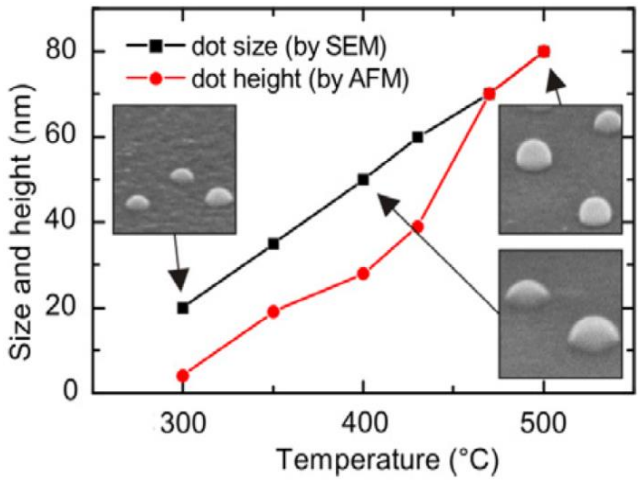

Figure 2-23: Temperature dependence of dot diameter and height after 30 keV Ga^+ irradiation with 1.0 × 10^{17} cm^{-2}; insets show SEM images of the segregated gallium [144].

Recently, Kupfer *et al*. [145] proposed a FIB-only approach for the fabrication of diamond micro-cantilevers and pointed out that the contamination with the gallium ions in diamond can be effectively eliminated by high temperature thermal treatment (above 500 ℃). Xu *et al*. [146] investigated the FIB-induced damage in diamond tool used in nanometric cutting and reported that the tool wear may result from the a-C layer created during FIB milling process. Through MC simulation, they pointed out that decreasing the FIB processing energy can reduce the Ga^+ implantation depth as well as the thickness of a-C layer.

Most recently, Kawasegi *et al*. [147] reported that the doping of gallium ion in a diamond tool (type 1b (1 0 0)-oriented single crystal diamond) can increase the adhesion of work materials to the tool surface, which would result in a rapid diamond tool wear at the gallium rich area. A combination of 500 ℃ heat treatment and aluminium deposition was demonstrated to be an effective method to remove the gallium ions and to improve the wear resistance of the ion-irradiated diamond tool. The transcribed tool shapes using the treated tool were uniform, resulting in a smooth surface (figure 2-24).

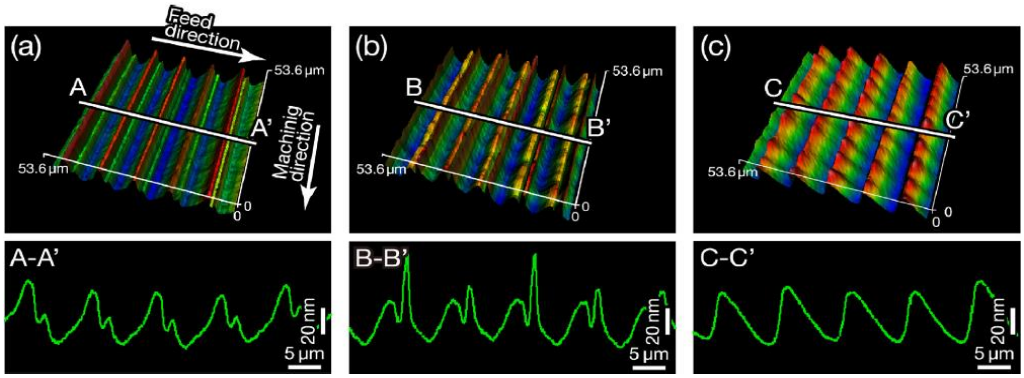

Figure 2-24: Surface topography of the NiP (nickel phosphorus) surface after machining using (a) non-FIB, (b) FIB, and (c) treated tools after a cutting distance of 50,080 m, measured using a white light interferometer [147].

2.5.3 Atomistic simulations of ion bombardment

Simulations of energetic ion-solid interaction can be used to predict a large number of experimentally observed quantities, and to probe areas outside the range of the experimental

observation. In recent decades, different kinds of computer simulation methods have been developed to examine the mechanism of ion penetration and ion-induced damage in various materials.

Binary collision approximation (BCA) and molecular dynamics (MD) are the two major simulation methods. BCA method approximates the full atomic dynamics of a material by a series of binary collisions, neglecting many possible body effects, which provides a computationally efficient means for examining the transport of energetic ions [73, 148-150]. MD methods describe the interactions between atoms involved in ion collision process more realistically, requiring much larger amounts of computer capacity than the BCA method [151]. In both BCA and classical MD simulations the interactions between atoms in the sample are described with interatomic potentials. The essential difference between these methods is how the atom motion is considered. The forthcoming sections will point out the principle and problems of BCA simulations in calculating ion collision, and illustrate why MD method is suitable for the study of energetic ion bombardment events by reviewing the significant results obtained from typical MD simulations.

2.5.3.1 Binary collision approximation method

In BCA calculations the movements of incident particles are usually treated as a sequence of independent binary collisions. For each individual collision the classical scattering integral is solved for a given impact parameter between the moving atom and a stationary atom in the target material by numerical integration [152]. The impact parameters of the next colliding atom and the atomic type used in the scattering integral are determined either from a stochastic distribution (such as the Monte-Carlo algorithm used in programs like TRIM/SRIM [72, 73, 150]), or in a way that considers the crystal structure of the matter (such as the method used in MARLOWE [153] and Crystal-TRIM [154, 155] where the atoms are either frozen at the ordered lattice sites or oscillating with the Debye frequency). Because the solution of the integral of motion results in precise scattering angles for both the

projectile and the target atoms, a fairly reliable prediction of ions penetration depths and formation of point defects in implanted materials can be achieved for almost all cases of interest [156]. Owing to its high computational efficiency in defect cascade simulations, it stands as a significant method particularly for calculating high-energy (MeV) ion behaviour [157]. Most recently, in the newly reported multiscale scheme, the BCA method can be used combined with MD simulations to include multiple scales in dimensions during high energy ion irradiation [158, 159].

Nevertheless, the BAC method has some inherent obstacles in describing the slowing-down process of energetic ions realistically. The first and the most important one is the basic assumption of binary collisions when trying to build a model taking multiple atomic interactions into account. It also makes it impossible to distinguish a cascade when it goes from the linear cascade to the heat spike regime [143, 157]. The scattering integral also does not allow for incorporating angle-dependent potentials, which significantly limits its capacity to describe covalently bonded materials like silicon and diamond [151, 160]. Moreover, although basically BCA models can estimate the overall spatial distribution of vacancy-like and interstitial-like damage by counting recoils that exceed the threshold displacement energy, it cannot distinguish the atomic structure of these defects [156]. In some cases, the defect distribution information can be irrelevant or meaningless. For example, the BCA simulation is able to predict the production of point defects in diamond created by the heavy ion irradiation. However, it is not able to pinpoint the location of a vacancy or interstitial in an amorphous zone and cannot identify whether local phase transition takes place. Additionally, the algorithm describes the atoms binding at surface in the same way as the inside atoms. Therefore, it is problematic when describing the sputtering or other surface effects [161].

In contrast, MD simulation which can describe the non-equilibrium ballistic motion of high energy ions as well as the subsequent thermalisation of the ions is ideally suited for the modelling of ion bombardment, and have emerged as the main computational tool for the

study of irradiation effects [162].

2.5.3.2 MD modelling of ion bombardment

In MD simulation, movements of all atoms are calculated. The full many-body dynamics in an atomic system is simulated with the accuracy limited only by the reliability of the interaction Hamiltonian employed [148]. The time evolution of an atomic system is calculated by numerically solving Newton equations of motion in a step-by-step fashion.

Ever since MD developed as a technique in the 1950s, it has been widely used to study all kinds of atomic-level physics, chemistry and biological issues. In fact, some very first uses of MD have already dealt with irradiation effects such as the phase transitions in hard spheres system [85], the thermal spike in irradiated metals [163], and many-processes in an energetic displacement cascade [164].

However, the major boom in MD simulations only began in the 1980s when the computer capacity was sufficient to monitor a system of thousands of atoms. In the remarkable work done by Harrison [165], MD simulations were carried out to investigate the sputtering of metals and rare gases. The channelling and blocking mechanisms for ion stopping and the emission patterns of particles from single crystals were initially revealed. The thermal spike in implanted metals can apparently enhance atom mixing process [166]. In the work by Rubia *et al*. [167], a large scale MD model was built to fully contain the collision cascade. The simulation results demonstrated the existence of the local melting in copper cascades created by 3 keV and 5 keV collisions. In the mid-1990s, numerous studies examined the defect and dislocation production in collision cascades [164, 168, 169] and illustrated local melting in a large variety of other materials [170, 171].

In addition to the thermal spike and its effect, other aspects such as the formation of defects, their spatial configuration and properties, and the phase transformations have also been widely investigated. In 1994, Averback [164] discussed the distinct mechanism of atom mixing in a displacement cascade, such as recoil implantation, cascade mixing, and thermal

spike mixing (as schematically illustrated in figure 2-25). The recoil implantation is important for the explanation of high energetic ion implantation. The cascade mixing theory yields reasonable agreement with experiment, however, the mixing value is far too small for those materials where thermal spikes are important. Ghaly *et al*. [172] further pointed out that the formation mechanism of damage product at near surface was different from those in the bulk. Their simulations also provided a new insight into the nature of nonlinear sputtering in metals.

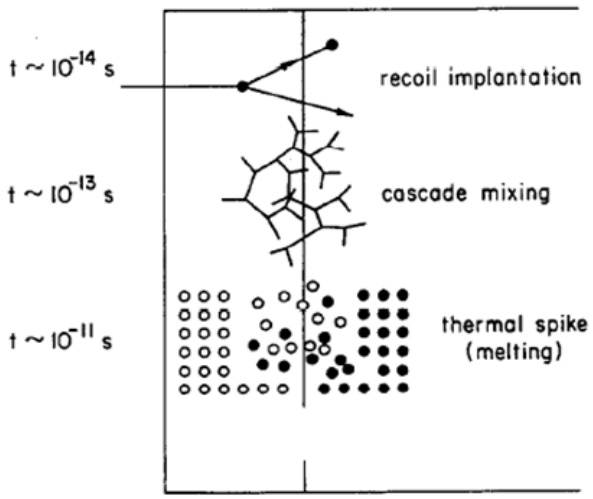

Figure 2-25: Schematic depiction of the three mechanisms of ion beam mixing: recoil implantation, cascade mixing, and thermal spike mixing [164].

Moreover, Rubia *et al*. [173] simulated the motion and clustering of vacancies and interstitials in silicon and showed the formation process of the stable amorphous zone in a collision cascade. Nordlund *et al*. [174] carried out a series of MD simulations to investigate the pre-existing point defect movement and annealing in collision cascades. In contrast to the annealing effects observed for FCC (face-centred cubic) metals where both interstitials and vacancies were pushed toward the centre of the liquid region, in silicon the amount of new damage created by a cascade is roughly independent of the number of initial point defects (as shown in figure 2-26). Later, they simulated the amorphisation of Si and pointed out that

low-energy recoils (about 3–15 eV) can also lead to a significant thermal dynamic recrystallization component during ion irradiation [175]. These works contributed a lot towards our understanding on the fundamental processes of ion-induced defects production.

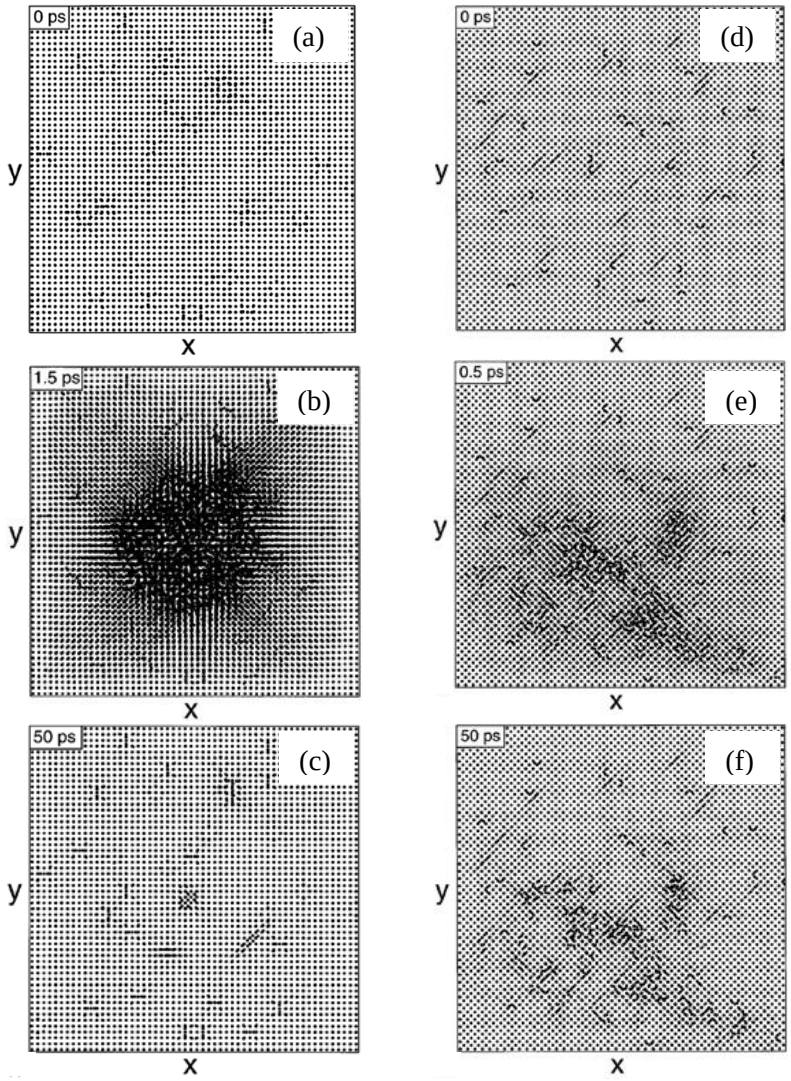

Figure 2-26: Snapshots of a 5 keV Au cascade (left column), and Si cascade (right column. The cascade is clearly less dense and well defined than in gold, and much more damage remains afterwards [174].

However, the spatial and time scales of these models were too small to fully track the whole process of multi-particle collision. The rapid progress in developing the computer power capacity in recent years, especially the development of parallel computing cluster technique,

has largely increased the size of computing domain and enabled the promised elucidation of multi-particle ion collision processes. Since then many research papers started to address the damage creation in various target materials under different irradiation conditions.

Kalish and his co-workers [176, 177] simulated the ion-induced damage in diamond and the thermal annealing process. The results indicated that the disrupted region (amorphous carbon) is rich in sp^2-like (graphitic) bonds, and the <1 0 0> split interstitial with a bonding configuration resembling graphite is the most stable defect (figure 2-27). The transformation depended significantly on the density of point defects created by the implantation. The damaged region collapses to graphite when the vacancy density exceeds a critical density of vacancies, whereas it regrows to diamond structure upon annealing for lower damage levels [178, 179]. Most recently, the formation of nanodiamond and nanographite from molten carbon has been emulated by MD simulations [180].

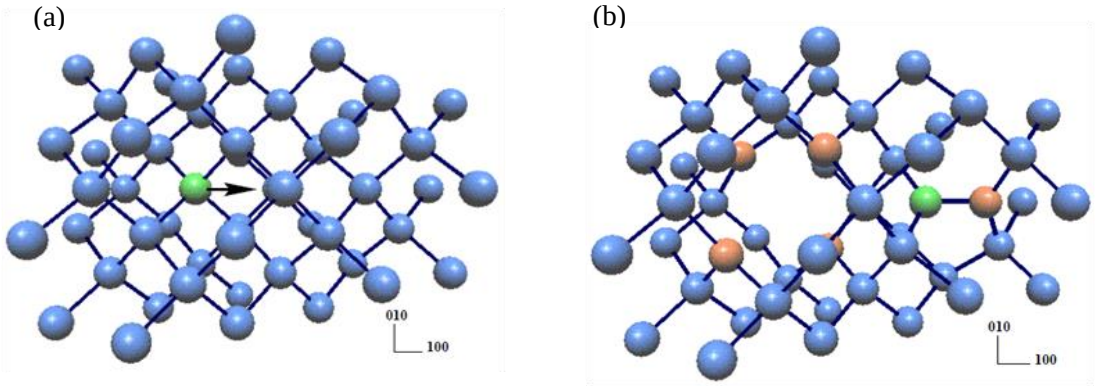

Figure 2-27: (a) Structure of the sample before any displacement (The direction of displacement is indicated by the arrow). (b) Structure of the damaged area obtained from knocking the marked (in green) atom with energy of 60 eV. Atoms remaining sp^3 bonded are drawn in blue. The displaced atom, now a member of a split interstitial is drawn in green, and sp^2 bonded atoms are drawn in brown [176].

In recent years, Satake *et al.* [181] studied the influence of computational domain and empirical potential function on the accuracy of simulation results (40 keV Ga^+ impact

silicon), and pointed out that a combination of ZBL (Ziegler, Biersack and Littmark) and Tersoff potential functions can offer more accurate description of the collision process than other tested potentials. Li *et al.* [182] compared the structural change of amorphous carbon when using different potential functions and recommend Tersoff potential for modelling ta-C. Large-scale MD computational domain was reported to be able to help express accurately the stopping of incident ions [181] as well as fully track the thermal spike [183]. Some recent research work also reported the effects of ion fluence and acceleration energy of incident ion on the Si surface deformation as shown in figure 2-28 [184, 185].

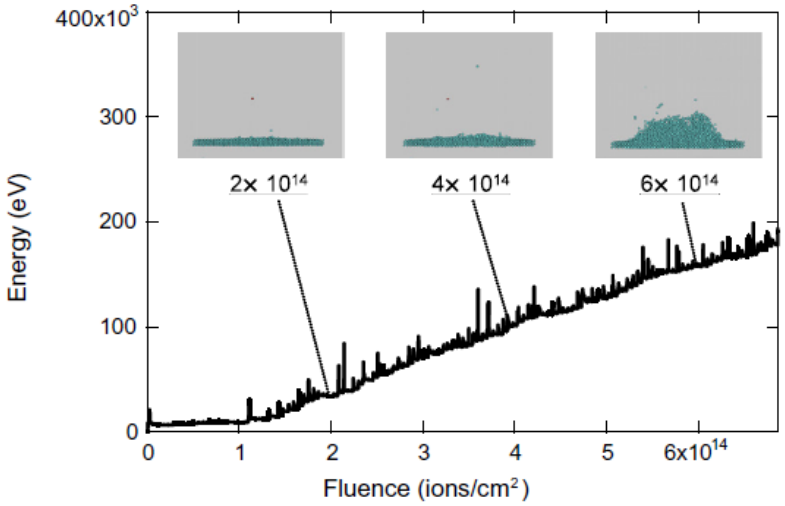

Figure 2-28: Energy of Si substrate versus Ar^+ fluence, and visualization of hillock structures at three fluence values [185].

Most recently, many research works were focused on the influence of beam processing parameters on the structure and properties of irradiated materials. Burenkov *et al.* [186] investigated the angular distribution of sputtered silicon at tilted gallium ion beam incidence. Their simulation results indicated that the variations of the surface structure of the silicon target change the total sputtering yield but have only a small impact on the angular distributions. Li and co-workers [187] studied the effect of incident angles of energetic carbon atoms (0-60 °) on the structure and properties of diamond-like carbon (DLC) film.

The surface roughness and the porous structure were increased with the incident angle (as shown in figure 2-29). A significant reduction of residual compressive stress was found when an incident angle of 45 ° was used, implying the great potential of controlling incident angle to improve the adhesive strength of DLC film.

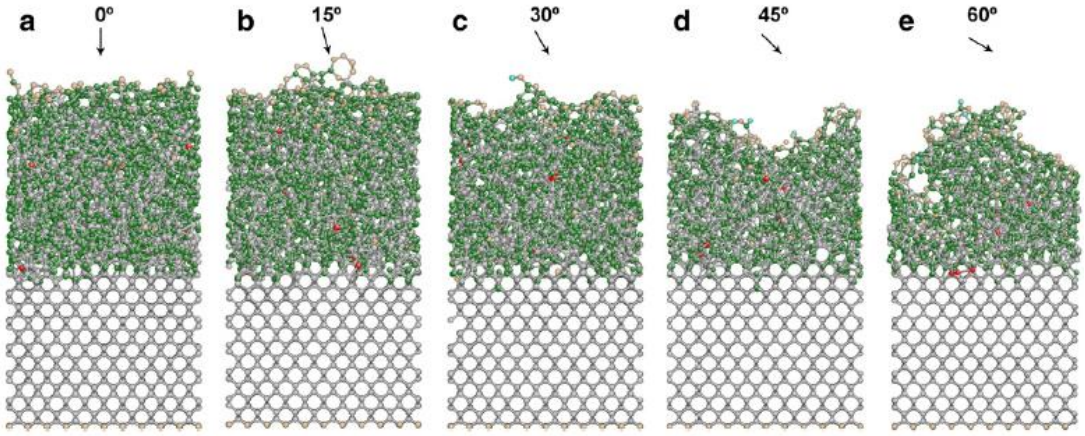

Figure 2-29: Snapshots of the films at the incident angles of (a) θ = 0°, (b) θ = 15°, (c) θ = 30°, (d) θ = 45° and (e) θ = 60°, where blue, yellow, green, gray and red colours represent the different coordination numbers of 1, 2, 3, 4 and 5, respectively [187].

2.5.4 Challenges in ion-induced damage study

The previous research work has provided a systematic analysis of ion-induced damage in diamond. However, most of the experimental work was concentrated on the CVD or doped diamond materials, not on natural single crystal diamond used in cutting tools. This is mainly due to the challenges involved in fabricating large, flat, and uniform TEM samples in undoped non-conductive diamond, particularly the beam drift caused by electrostatic charging of diamond. Moreover, in a typical FIB irradiation experiment, only ion dose is measurable during the test. The attempts to detect phase transformation that might occur during FIB processing diamond, are often disconnected from physical observations. The post-facto-observation leaves a gap in understanding the formation process of ion-induced damage, forcing the use of assumptions. In many cases, the average results measured by

experiments will hide the fact of dynamic damage processes in target materials under different irradiation conditions.

In contrast, MD simulations of ion bombardment have shed much light on ion beam mixing for decades. These activities make it an interesting and important task to understand what the fundamental effects of energetic particles on matter are. However, most of the models for tracking the evolution of amorphous zones in diamond are either borrowed from the actual cascade simulations or created artificially, and thus yield limited insight into the whole ion collision process [151, 156, 162]. Additionally, due to the lack of potential function which is capable of describing the interactions between incident gallium ions and carbon atoms, the previously reported artificial multi-particle self-collision model cannot provide detailed information on the motion or spatial distribution of implanted gallium ions.

2.6 Summary

This chapter has presented a literature review on the state-of-the-art diamond turning using micro- and nanoscale diamond tools. The review indicates that diamond turning using multi-tip single crystal diamond tools fabricated by FIB has powerful capacity in the fabrication of micro- and nanostructures. However, the lack of support from systematic theoretical study has seriously hindered the advance and industrialization of this technique. The remaining challenges against the discovery and advancement of this technique for the deterministic fabrication of nanostructures has been summarized, including the characterization of FIB-induced damage during tool fabrication process, the revealing of mechanism of machining nanostructures, the quantification of the tool shape transferability, and the development of processing technology. The current research progress and technical challenges regarding the study of FIB-induced damage in diamond have also been reviewed.

Chapter 3 Development of a random multi-particle collision model for MD simulation

3.1 Introduction

In recent years, FIB milling techniques have been extended towards the fabrication of micro- and nanoscale diamond tools used in ultra-precision machining [34, 53-55, 58]. Several pioneering works have initially demonstrated the feasibility of using nanoscale diamond tools for scaling up fabrication of nanostructures through diamond turning operation. Nevertheless, it is a technique which remains at the immature stage. The exposure of diamond tool to FIB will result in the implantation of the ion source material and the amorphisation of the milled area at the near surface. The ion-induced damage of cutting edges during the tool fabrication process and its effect on the cutting performance of nanoscale diamond tools remain uncovered. Investigation of the fundamental physical aspects of ion collisions, leading to processing defects in FIB machining, is in high demand for a deterministic fabrication of nanoscale diamond tools.

As compared with other simulation methods, MD simulation method has long been regarded as a powerful and effective tool for analysing ion-solid interaction with regard to its capacity of tracking atoms dynamically. Unfortunately, due to the limitations of computer power and the lack of suitable potential functions to describe the interaction between Ga ions and the target materials, many previous MD simulation systems were limited in scale with inadequate experimental correspondence, and thus yielding comparatively limited insight into the whole ion collision process.

In this chapter, a novel random distribution multi-particle collision MD model is developed to study FIB-induced damage in diamond. This chapter starts with a description of the important parameters for a successful MD simulation of energetic ion bombardment, as well as the post processing methods used for analysing simulation results. The discussion then

turns to how the impulse of each single ion leads to atomic displacements and finally to a residual damaged layer at irradiation area.

3.2 Parameters for an MD simulation of energetic ion bombardment

MD is a computational method for the simulation of physical movements of atoms and molecules. It is a deterministic simulation methodology in which atoms and molecules are allowed to interact for a period of time by approximations of known physics, giving a view of the motion of the atoms as schematically shown in Figure 3-1.

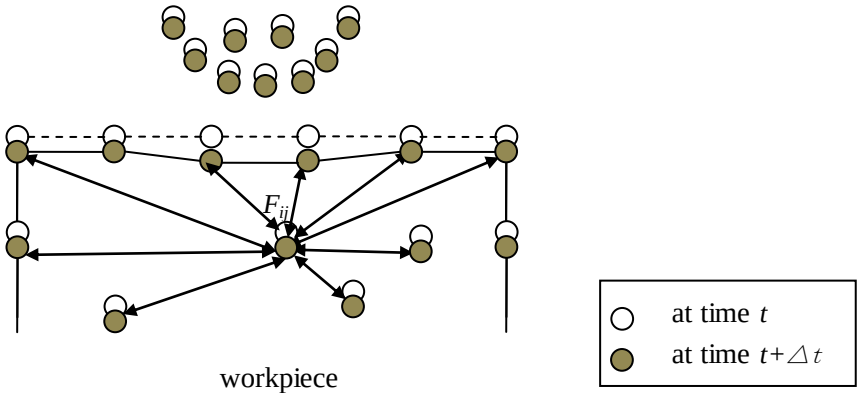

Figure 3-1: Schematic of physical movements of atoms in MD simulation for FIB machining.

The key issue in an MD simulation system is to choose the right potential function such as a function V (r_1, r_2, …, r_n) of the positions of the nuclei, representing the potential energy of the system when atoms are arranged in that specific configuration. Forces can then be derived as the gradient of the potential with respect to the atomic displacements.

$$F_i = -\nabla_{r_i} V(r_1, r_2, \ldots, r_N) \tag{3-1}$$

In the most common versions, the trajectories of molecules and atoms can then be determined by numerically solving Newton's equations of motion for a system of interacting particles.

3.2.1 Boundary conditions and system size

MD simulations are usually carried out in a 3D cubic box. The atoms of a model are allocated into one of three different zones: boundary atoms zone, thermostatic atoms zone, and Newton atoms zone. The boundary atoms are kept fixed in their initial lattice positions, serving to maintain the symmetry of the lattice. The thermostatic atoms are used to simulate the thermostatic effects of the bulk and guarantee the equilibrium temperature to approach a desired value. The workpiece is represented by the Newton atoms which are assumed to follow the classical Newton's second law of motion, computed from the interatomic forces described by potential functions.

Since MD was first developed to calculate interatomic forces among all atoms within a certain boundary, intensive computational power is required to obtain enough data in a reasonable time. For the energetic ion collision process, it is important to make sure that the system size is able to track all the stopping processes of incident particles as well as the entire collision cascades happening subsequently. In a typical FIB machining process, each incident Ga ion will create a damaged region along its trajectory in the target material. As a result, small systems cannot be used in a full analysis of collision cascades, and the thickness of the substrate built in a MD system needs to be large enough for multi-particle collisions.

Recently, Smith *et al.* [183] pointed out that there is no fixed rule for boundary condition and system size as long as the lateral cascade never reaches the edges of the system. Thus, the boundary influence is negligible when the boundary atoms are sufficiently far away from the cascade. Since the kinetic energies of incident ions and the properties of target materials are the two major impact parameters determining the actual range of collision cascades, the system size and the boundary condition should be calculated by a numerical experimentation. In our study, a single ion collision model was built to obtain necessary parameters for building a multi-particle ion collision model, which will be discussed in section 3.4. It is necessary to contain the cascade fully so that all effects are captured.

3.2.2 Potential functions for ion collision study

The potential function in an MD simulation is a description of the terms by which the particles in the simulation will interact. The accurate level of MD simulation results depends significantly on the selected potential function. In recent decades, many empirical and semi-empirical potential functions have been developed to approximate atomic force fields for large atomic aggregates. According to the number of atoms considered in computing the interaction atomic forces, the potential functions can be broadly classified into pair potential functions and many-body potential functions.

The pair potential functions representing the non-bonded energy are formulated as a sum over interactions between the particles of the system. It is the simplest choice employed in many popular force fields, in which the total potential energy can be calculated from the sum of energy contributions between pairs of atoms. A classic example of such pair potential functions are the non-bonded Lennard-Jones potential function [188, 189] and the Morse potential function [190, 191].

The many-body potential functions include the effects of three or more particles interacting with each other. An example of such a potential for covalent materials is the Tersoff potential function [192], which has been used to simulate a wide range of brittle materials such as carbon, silicon, and germanium. Other examples are embedded atom method (EAM) potentials [193] and Tight-Binding Second Moment Approximation (TBSMA) potentials [194] which are widely used to describe ductile metals and alloys. The state of electron density in the region of an atom is calculated from a sum of contributions from the surrounding atoms, and the potential energy contribution is then a function of this sum.

The potential functions used in the MD simulation studies of energetic ion collisions performed so far have been listed in Table 3-1 with highlighting remarks. It is evident from the table that various potential functions have been developed and used in the previous research works. Most recently, Satake *et al*. [181] compared the influence of potential

functions on the energy transition and indicated that the kinetic energy of gallium ion cannot be effectively transferred to silicon when using Tersoff potential as compared with ZBL potential function. A combination of the Tersoff potential [192] with the ZBL potential [149] (named Tersoff.ZBL potential) has shown the best results among other tested potential functions.

Table 3-1: Main potential functions for the simulation of ion collision

Case (Ion source/Workpiece)	Potential function for Ion-workpiece	Potential function for workpiece-workpiece	Details
Ga/Si	Lennard-Jones	Tersoff	S. Satake *et al*. [181]
Ga/Si	Tersoff	Tersoff	
Ga/Si	ZBL	Tersoff	
Ar/Si	ZBL	Tersoff	S. Satake *et al*. [184]
Ar/4H-SiC	ZBL	Tersoff	S. Satake *et al*. [195]
Ga/Si	Tersoff.ZBL	Tersoff.ZBL	A. Burenkov *et al*. [186]
Ga/Si	ZBL	Tersoff.ZBL	M.F. Russo Jr. *et al*. [196]

The Tersoff.ZBL potential function includes a 3-body Tersoff potential with a close-separation pairwise modification based on a Coulomb potential and the ZBL universal screening function, giving the system energy E_{TZBL} of all atoms as:

$$E_{TZBL} = \frac{1}{2}\sum_{i}\sum_{j\neq i} V_{ij} \tag{3-2}$$

$$V_{ij} = (1 - f_F(r_{ij}))V_{ij}^{ZBL} + f_F(r_{ij})V_{ij}^{Tersoff} \tag{3-3}$$

$$f_F(r_{ij}) = \frac{1}{1 + e^{-A_F(r_{ij}=r_c)}} \tag{3-4}$$

where the V_{ij}^{ZBL} and the $V_{ij}^{Tersoff}$ indicate ZBL portion and Tersoff portion, respectively. The distance between atoms i and j is r_{ij}. The f_F term is a Fermi-like function used to smoothly connect the ZBL repulsive potential with the Tersoff potential. There are two parameters used to adjust it: A_F and r_C. A_F controls how "sharp" the transition is between the two potentials, and r_C is essentially the cut-off distance for the ZBL potential.

For the ZBL portion, the interaction potential, V_{ij}^{ZBL}, between two atoms i and j can be written in the form of

$$V_{ij}^{ZBL} = \frac{1}{4\pi\varepsilon_0}\frac{Z_1 Z_2 e^2}{r_{ij}}\phi(r_{ij}/a) \tag{3-5}$$

$$\phi(x) = 0.1818e^{-3.2x} + 0.5099e^{-0.9423x} + 0.2802e^{-0.4029x} + 0.02817e^{-0.2016x} \tag{3-6}$$

where Z_1, Z_2 are the numbers of protons in each nucleus, e is the electron charge (1 for metal and real units) and ε_0 is the permittivity of vacuum. $\phi(r_{ij}/a)$ is the ZBL universal screening function and a is the Thomas-Fermi screening radius for collision and is given by

$$a = \frac{0.8854a_0}{Z_1^{0.23} + Z_2^{0.23}} \tag{3-7}$$

where a_0 is the Bohr radius (typically 0.529 Angstroms). This screening function should be applicable to most systems. However, it is only accurate for small separations (i.e. less than 1 Angstrom).

For the Tersoff portion, the interaction potential, $V_{ij}^{Tersoff}$, between two atoms i and j can be computed as follows:

$$V_{ij}^{Tersoff} = f_C(r_{ij})[f_R(r_{ij}) + b_{ij} f_A(r_{ij})] \tag{3-8}$$

$$f_C(r) = \begin{cases} 1 : r < R - D \\ \frac{1}{2} - \frac{1}{2}\sin(\frac{\pi}{2}\frac{r-R}{D}) : R - D < r < R + D \\ 0 : r > R + D \end{cases} \quad (3\text{-}9)$$

$$f_R(r) = A\exp(-\lambda_1 r) \quad (3\text{-}10)$$

$$f_A(r) = -B\exp(-\lambda_2 r) \quad (3\text{-}11)$$

and

$$b_{ij} = (1 + \beta_e{}^n \zeta_{ij}^n)^{-\frac{1}{2n}} \quad (3\text{-}12)$$

$$\zeta_{ij} = \sum_{k \neq i,j} f_C(r_{ik}) g(\theta_{ijk}) \exp[\lambda_3^3 (r_{ij} - r_{ik})^m] \quad (3\text{-}13)$$

$$g(\theta) = 1 + \frac{c_e{}^2}{d_e{}^2} - \frac{c_e{}^2}{[d_e{}^2 + (\cos\theta - h_e)^2]} \quad (3\text{-}14)$$

where i, j, and k label the atoms of the system, r_{ij} is the length of the ij bond, r_{ik} is the length of the ik bond, b_{ij} is the bond order term, θ_{ijk} is the bond angle between the bonds ij and ik, f_R is a two-body term representing a repulsive pair potential, and f_A represents an attractive pair potential including three-body interactions. f_C merely represents a smooth cut-off function to limit the range of the potential, and ζ_{ij} is the angle potential portion which counts the number of other bonds to atom i besides the ij bond.

For this work, the Tersoff.ZBL potential function is used to describe the atomic interactions. Table 3-2 depicts the Tersoff.ZBL potential function parameters for different variants of pure Ga and C.

Table 3-2: Tersoff.ZBL potential function parameters for pure Ga and C

Parameters	Ga	C
m	1	1
c_e	7.6298×10^{-2}	1.9981×10^{4}
d_e	1.9796×10^{1}	7.0340
h_e	7.1459×10^{-1}	-3.3953×10^{-1}
n	3.47290	9.9×10^{-1}
β_e	2.3586×10^{-1}	4.1612×10^{-6}
$A[eV]$	2.83982×10^{3}	1.5448×10^{3}
$B[eV]$	1.14786×10^{2}	3.8963×10^{2}
$D[\text{Å}]$	0.1	0.15
$\lambda_1[\text{Å}^{-1}]$	3.2834	3.4653
$\lambda_2[\text{Å}^{-1}]$	1.7154	2.3064
$\lambda_3[\text{Å}^{-1}]$	0	0
$R[\text{Å}]$	2.8	1.8
Z_i	31	6
Z_j	31	6

For the interaction of C-Ga, the parameters for species *i* and *j* can be calculated using the mixing rules as listed bellow:

$$\lambda_1^{i,j} = \frac{1}{2}(\lambda_1^i + \lambda_1^j) \tag{3-15}$$

$$\lambda_2^{i,j} = \frac{1}{2}(\lambda_2^i + \lambda_2^j) \tag{3-16}$$

$$A_{i,j} = (A_i A_j)^{1/2} \tag{3-17}$$

$$B_{i,j} = (B_i B_j)^{1/2} \tag{3-18}$$

$$R_{i,j} = (R_i R_j)^{1/2} \tag{3-19}$$

$$S_{i,j} = (S_i S_j)^{1/2} \tag{3-20}$$

where A—cohesion energy of the repulsive pair potential function

B—cohesion energy of the attractive pair potential function

D—cut-off distance of tersoff potential in LAMMPS

S_i—cut-off distance for species i in tersoff potential

S_j—cut-off distance for species j in tersoff potential

R—radius of first neighbour shell

m, n—high order constant

β_e—bond order parameter

λ_1—slope parameter of the repulsive pair potential curve

λ_2—slope parameter of the attractive pair potential curve

λ_3—slope parameter of the cut-off potential function

c_e, d_e,h_e—elastic constant in Tersoff potential function

Z_i—electron charge of the i-th atom nuclei from the coulomb potential

Z_j — electron charge of the j-th atom nuclei from the coulomb potential

3.2.3 Equilibrium lattice parameter

The lattice parameter of a solid corresponds to the length of the unit cell at the equilibrium volume. In MD simulations, the lattice parameter may vary with the individual potential function. Thus, it is suggested to use the equilibrium lattice parameter for the selected potential function in order to improve the accuracy of simulation results.

The lattice parameter can be obtained through an energy minimization process of a single cell (as shown in figure 3-2). The lattice energy per atom E_L is defined as:

$$E_L = \frac{E_p}{N_{\text{cell}}} \tag{3-21}$$

where E_p is the potential energy of the lattice, N_{cell} is total number of atoms in the simulation cell. In this study, the minimum lattice energy per atom E_L = -7.46909092 eV for diamond was observed at a lattice parameter of a_1 = 3.567 Å when using the Tersoff.ZBL potential function as discussed above.

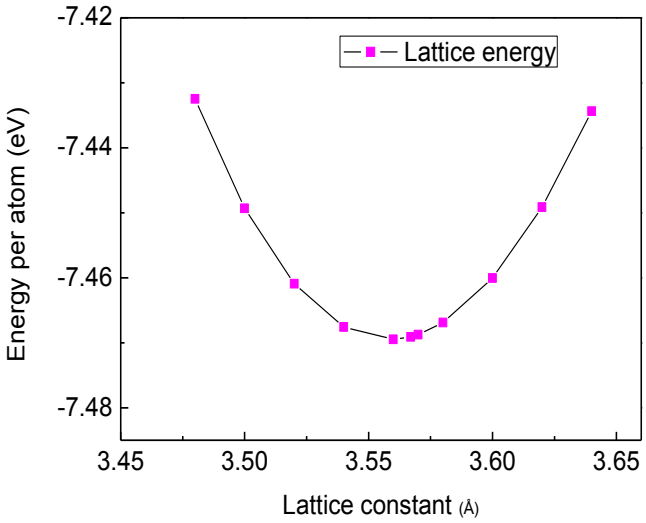

Figure 3-2: The variation of lattice energy with the lattice constant when using Tersoff.ZBL potential function.

3.2.4 Ensembles

An ensemble is a collection of all possible systems which have different microscopic states but have an identical macroscopic or thermodynamic state. There are four most common ensembles: micro-canonical ensemble (or NVE ensemble), canonical ensemble (or NVT ensemble, isobaric-isothermal Ensemble (or NPT ensemble), and grand canonical ensemble (or μVT ensemble).

- Microcanonical ensemble (NVE): The thermodynamic state characterized by a fixed number of atoms, *N*, a fixed volume, *V*, and a fixed energy, *E*.
- Canonical Ensemble (NVT): This is a collection of all systems whose thermodynamic state is characterized by a fixed number of atoms, *N*, a fixed volume, *V*, and a fixed temperature, *T*.
- Isobaric-Isothermal Ensemble (NPT): This ensemble is characterized by a fixed number of atoms, *N*, a fixed pressure, *P*, and a fixed temperature, *T*.
- Grand canonical Ensemble (μVT): The thermodynamic state for this ensemble is characterized by a fixed chemical potential, μ, a fixed volume, *V*, and a fixed temperature, *T*.

However, since the high energetic ion bombardment event is inherently a non-equilibrium process, only the micro-canonical ensemble (NVE) is applicable for the description of the collision phase [156]. In this investigation, NVE ensemble is selected for the isolated system describing the ion bombardment. The thermodynamic state was characterized by a fixed number of atoms (*N*), a fixed volume (*V*), and a fixed energy (*E*).

3.3 The post-processing methods

3.3.1 Calculation of the atomistic equivalent temperature

The characterization of the local temperature at core collision area is important to the understanding of defects formation process. According to the law of equipartition of energy, the representative temperature of a group of atoms can be calculated from the total atomic kinetic energy of the group. However, this averaged temperature has difficulty in identifying the feature of temperature distribution at core collision area which is normally laid in several nanometres.

In the current study, a concept of atomistic equivalent temperature T_i, which is calculated from the statistical average temperature of neighbour atoms around the atom *i*, is used to

characterize the variation of temperature at core collision area during ion collision processes. As the nature of the temperature is statistical, the accurate level of the temperature calculated significantly depends on how the atoms are being selected. In general, the larger the cut-off distance, the lower the calculated temperature. It was found through trial simulations that, the range of ion-induced damage along a single ion trajectory was about 4 nm. In order to reflect the local thermal behaviours of diamond under ion irradiation, a critical cut-off of radius r_0 = 4 nm was employed in this study to select the neighbour atoms for the calculation of temperature T_i. The translation between the atomic kinetic energy and the statistical temperature is calculated using the following equation:

$$K_E = \frac{1}{2}\sum_{j=1}^{n} m_j v_j^{\,2} = \frac{3}{2} n k_B T_i \tag{3-22}$$

where K_E is the total kinetic energy of a group of atoms, n is the number of atoms within the radius r_0, m_j and v_j represent the mass and instantaneous velocity of atom j respectively, and k_B is the Boltzmann constant ($1.3806503 \times 10^{-23}$ J/K).

3.3.2 Quantification of ion-induced damage

Many previous researches have reported that the exposure of diamond materials to FIB would result in an amorphous carbon layer at near surface [45, 46]. Generally amorphous structures can be characterized by a high degree of short range order and an absence of long range order. In order to describe the structure of ion sputtered diamond, the coordination number analysis (CNA) and the radial distribution function (RDF) are used.

3.3.2.1 Coordination number analysis

The CAN is a useful measure of the local crystal structure around an atom. The coordination number n_c is the number of nearest neighbour atoms. The original CAN method was proposed by Honeycutt and Andersen [197]. It was further modified by Faken [198] and

Tsuzuki [199]. The method is based on the analysis of the nearest neighbours of an atom within a defined cut-off distance. Two atoms are marked as nearest neighbours if the distance between them is less or equal to a cut-off distance.

3.3.2.2 Radial distribution function

The radial distribution function g(*r*) describes how density varies as a function of distance from a reference particle. Instead of looking at the first nearest neighbours only, the algorithm counts the number of atoms that lie at the distance *r* from a specific atom, averaging over all the atoms of the lattice. For a perfect lattice, g(*r*) will give delta functions at characteristic distances of the lattice.

As illustrated in figure 3-3, considering a homogeneous distribution of the atoms in a space, the RDF, g(*r*), represents the probability to find an atom in a shell d*r* at a distance *r* from another atom chosen as a reference point. The number of atoms *dn*(*r*) at a distance between *r* and *r* + *dr* is expressed as follows:

$$dn(r) = \frac{N}{V} g(r) 4\pi r^2 dr \tag{3-23}$$

where *N* represents the total number of atoms, *V* is the model volume.

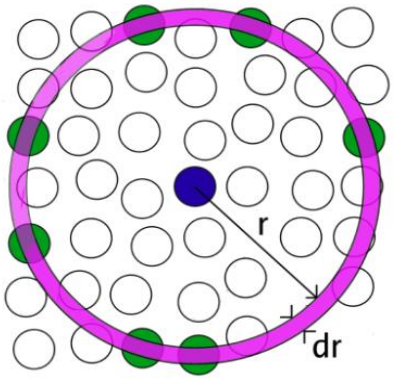

Figure 3-3: Schematic diagram of radial distribution function [200].

3.4 Single ion collision

3.4.1 MD simulation model for a single ion collision

In order to gain fundamental understanding of the ion damage process and to obtain basic parameters for building up a multi-particle collision model, a single ion collision model was built as shown in figure 3-4. The free boundary condition is applied in all directions of the model. The diamond crystalline lattice and the corresponding coordinate axes are shown in figure 3-4 (a). The three orientations of diamond substrate are [1 0 0], [0 1 0] and [0 0 1] in the X, Y and Z directions, respectively. As shown in figure 3-4 (b), the target workpiece has a computational region size of $50a_1 \times 50a_1 \times 60a_1$, composed of 1,217,161 atoms in total, where the lattice constants a_1 is 3.567 Å for diamond. Except the ion irradiation surface (top surface), all the rest boundary atoms are fixed (thickness of $2a_1$).

The voltage of ion beams is assumed to be 8 kV in the simulation and is translated into the velocity of gallium atom corresponding to the specific energy. The incident angle is 0°, parallel to the Z axis. For the beam energy and materials treated here, the electronic stopping power is expected to contribute very little to slow down the gallium ion, and thus it is neglected in current study. Since the velocities of atoms at the initial collision cascade are extremely high, the time step used for solving the equations of motions has to be short enough. It has been found by "trial and error" approach that a time step of 0.1 fs is a good trade-off between computational efficiency and velocity insensitivity, and hence it is adopted in the simulation. Before the ion collision, the system temperature was adjusted to 297 K through 80,000 time step's relaxation process. The thermostat atoms in thermal layer (thickness of $3a_1$) were kept at a constant temperature of 293 K using the velocity scaling method to perform the heat dissipation during the ion collision process [101].

Large scale atomic/molecular massively parallel simulator (LAMMPS) [201] was used to perform the simulation. The visualization of the results was performed by software named Visual molecular dynamics (VMD). The concept of atomistic equivalent temperature [202]

was employed to analyse the temperature distribution at the core collision area which has a size of $40a_1 \times 40a_1 \times 35a_1$ (indicated by the dotted line in figure 3-4 (c)).

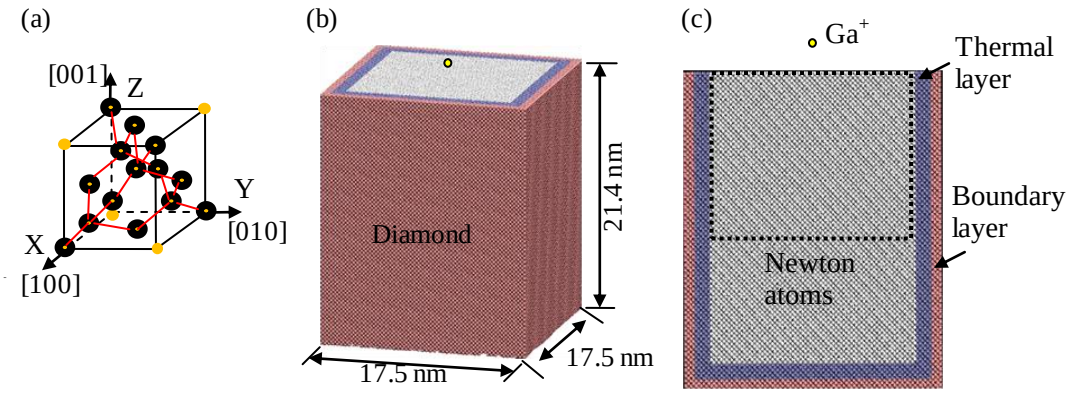

Figure 3-4: Single Ga^+ collision MD simulation model: (a) The diamond crystalline lattice and the corresponding coordinate axes; (b) the dimensions of diamond bulk model (front view); and (c) a cross-sectional view of the workpiece (The dotted line indicated the core collision area selected for local temperature analysis).

3.4.2 Ion collision process

The local temperature and the collision-dynamics during the interaction of a single 8 keV gallium ion with the diamond are shown in figure 3-5. Each diamond atom was coloured by the atom's common neighbour analysis (CNA) value. The cyan and purple atoms represent the dangling bonded and sp^2 bonded C atoms respectively. Moreover, the defect-free regions (sp^3 hybridization) were removed from the visualizations. As shown in figure 3-5, the single ion collision process comprises a temperature spike portion (encircled by the dotted line in figure 3-5; magnified and shown in inset (a)) and a relatively long stage of recrystallization process (healing the atomic defects).

When an energetic ion particle enters into the solid, it transfers its energy and momentum to the target atoms and creates voids and interstitials in addition to surface sputtering. At initial collision stage, the irradiated Ga particle interacts with the C atoms, and a large number of atomic defects (vacancies and interstitials) are created by breaking the local sp^3 bonds of

diamond (inset (b) in figure 3-5). During this period, the Ga particle transfers its kinetic energy partly into thermal energy of the target material. At 0.028 ps, the local temperature reaches a peak value of 1327.5 K. This highest local temperature region is located at the surface facing the ion beam irradiation. Also, the damage zone was observed to grow continuously through the displacement cascades. The peak disorder of the local lattice structure was found at 0.072 ps at which the local temperature was found to be cooled down to 793.8 K (figure 3-5 (c)). Following the growth of the damage zone, there is a long stage of relaxation process, during which the local high temperature provides thermal energy for the atomic defects to anneal back to diamond structure [203, 204]. After the full-relaxation-process, it is noted that more than half of the atomic defects annealed back to diamond structure (figure 3-5 (e)), and finally only a few atomic defects remain in the sample, mostly sp^2 bonded.

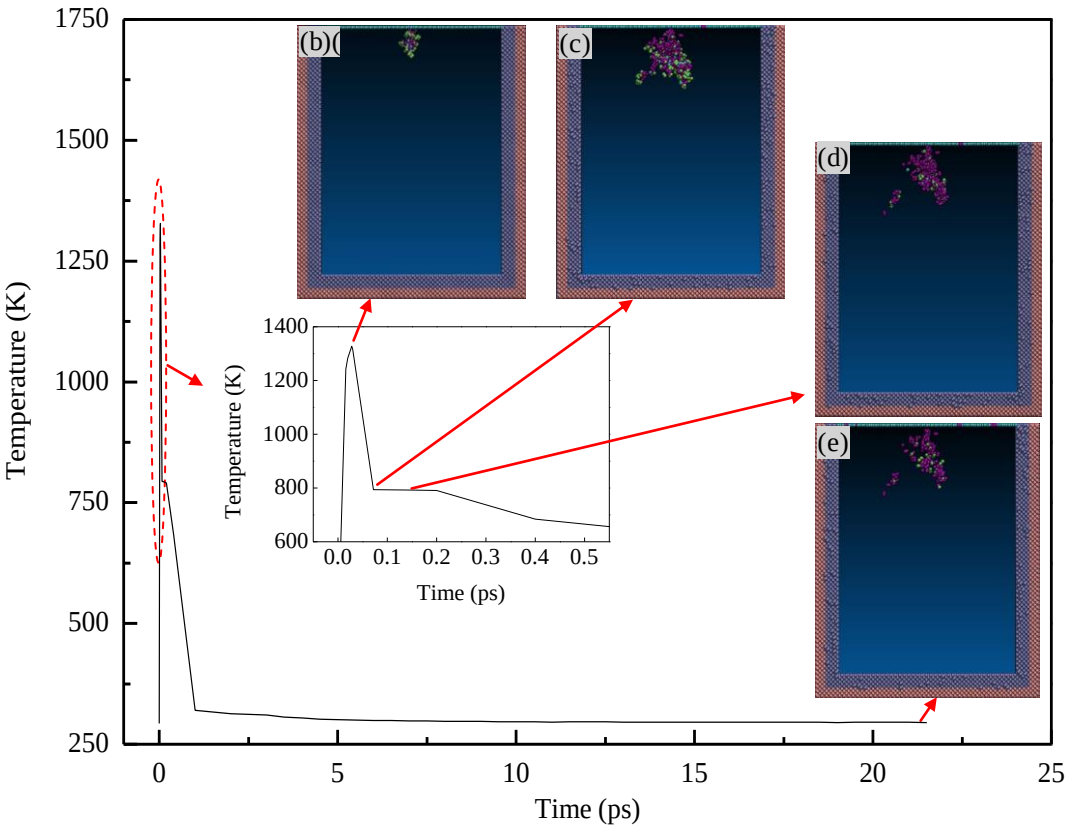

Figure 3-5: Molecular dynamics simulations describing the temperature evolution and the

recrystallization process for the single Ga particle collision of diamond. Inset (a): the local view of the temperature during the temperature spike phase. Inset (b): the initial defects created when the local temperature has reached the peak value of 1327.5 K at 0.028 ps; this highest temperature region is shown by the encircled line. Inset (c): the defect configuration at the stage of the peak disorder of the lattice achieved at 0.072 ps. Inset (d): an intermediate phase during the re-crystallization process observed at 0.15 ps; Ga particle stopped inside the diamond bulk at this stage. Inset (e): the residual atomic defects after the system cooled down to 293 K at 21.5 ps. The cyan and purple atoms represent the dangling bonded and sp^2 bonded C atoms respectively. The atoms in lime colour are interstitials. The C atoms of perfect diamond structure are removed from the visualizations.

3.5 Random multi-particle collision

3.5.1 The spatial distribution of particles in the ion beam

A major challenge to simulate the successive FIB milling process is how to describe the nature of ion beams under different ion irradiation conditions. The extremely long path length of each gallium projectile also requires a large sample size in order to track the whole ion collision process. Based on the results obtained from single ion collision, a unique scheme was developed to build up a random multi-particle collision model.

A typical FIB beam profile is usually considered as 2D Guass distribution with a circular cross section in nature. The intensity distribution satisfies the following equation:

$$J(x,y)=\frac{I}{2\pi\sigma^2}\exp\left[-\frac{(x-x_p)^2+(y-y_p)^2}{2\sigma^2}\right] \tag{3-24}$$

where $J(x, y)$ is the ion flux density at a point (x, y); I is the ion current and σ is the standard deviation of the Gaussian distribution; the centre of the beam is located at point (x_p, y_p).

The beam spot size is usually characterized as the full width at half maximum (FWHM) of the intensity or e^{-1} (36.7%) of the maximum intensity. In this study, FWHM was used to

calculate the beam size. The beam diameter d_{beam} can be approximately estimated as:

$$d_{beam} = \sqrt{8\ln 2}\sigma \tag{3-25}$$

In a typical FIB system, the beam diameter is adjusted to control the ion current. An illustration of this relationship for the FIB used in current study is shown in figure 3-6.

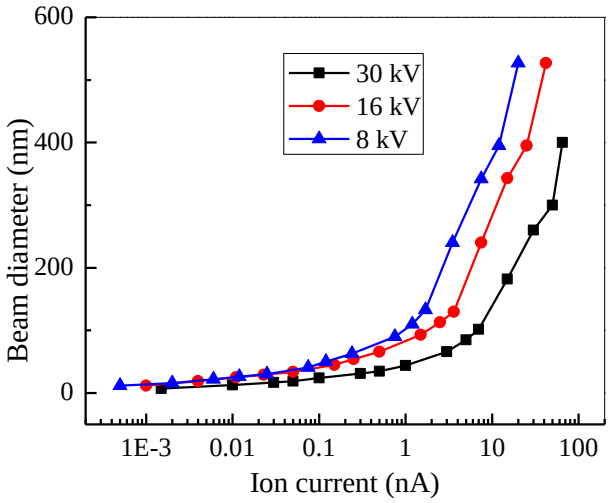

Figure 3-6: The relationship between the ion current and the beam diameter of the FIB system used in this study.

The flowchart of a program developed for building the multi-particle collision model is illustrated in figure 3-7. First of all, the ion dose is calculated according to the selected ion irradiation condition. After selecting the beam current I, the spot size d_{beam}, the acceleration voltage V_{beam} and the dwell time t_d, the total number of incident particles, N_{Ga}, can be calculated as follows:

$$N_{Ga} = \frac{I \times t_d}{e} \tag{3-26}$$

An algorithm was used to generate the initial coordinates for the N_{Ga} points having random distribution, and then normalized the coordinates to fit the defined sputter area of the MD model. In order to avoid the overlap of atom's coordinates, the coordinates were selected before being input to the system.

Further, in order to place the entire beam of particles in the MD simulation system but not have them adversely interacting, the incident particles are initially invisible to the system, having no mass, velocity, or potential with any of the C atoms in the system. The particles were then turned on, one by one, having the correct mass of gallium and the velocity corresponding to the energy of beam.

As discussed above, each ion collision process comprises a temperature spike portion and a relatively long stage of recrystallization process. After each bombardment event the system is equilibrated via a velocity scaling stochastic layer until a point when the energy of the system has relaxed to a corresponding temperature of 293 K. Once this relaxation has completed, typically requiring an interval of 20-30 ps depended on the energy of the impact ions and the target workpiece materials, the next gallium particle was allowed to impinge onto the sample until the last ion collision finished.

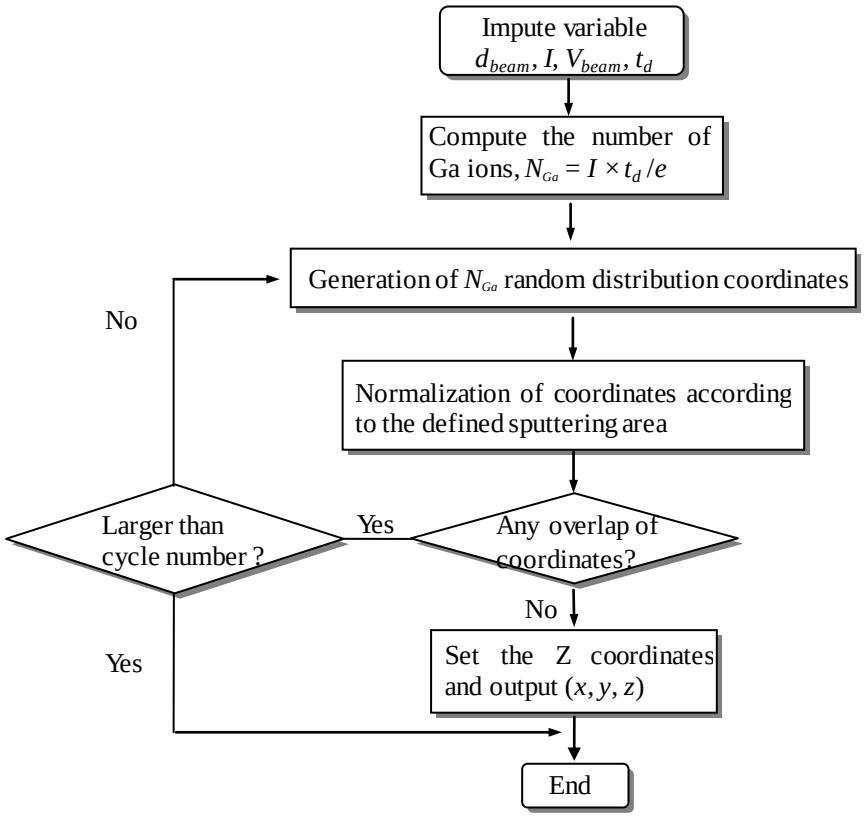

Figure 3-7: The program flowchart for building the coordinates of incident particles.

3.5.2 MD simulation model of multi-particle collision

The multi-particle collision MD model was built as shown in figure 3-8. The dimensions of the diamond bulk are the same as the single ion collision model, i.e. a square box with a dimension of $50a_1 \times 50a_1 \times 60a_1$. Free boundary condition was used to avoid the reflection effect caused by using fixed or period boundary conditions. At the beginning of ion collision, the gallium ions were introduced at a random location above the irradiation area (d_{beam} = 3.0 nm) as shown in figure 3-8 (b). The incidence angle is 0 °which is perpendicular to the (0 0 1) surface of diamond because the (1 0 0) lattice plane is usually used as the rake face of diamond cutting tools. The dotted line in figure 3-8 (b) indicates the core collision area selected for temperature analysis.

The interval time between each ion collision was set to 21.5 ps which was determined by the single ion collision event as discussed before. The number of incident gallium particles used in this simulation is 23 from the irradiation area (figure 3-8 (a)), corresponding to ion fluence up to 4.0×10^{14} ions/cm^2.

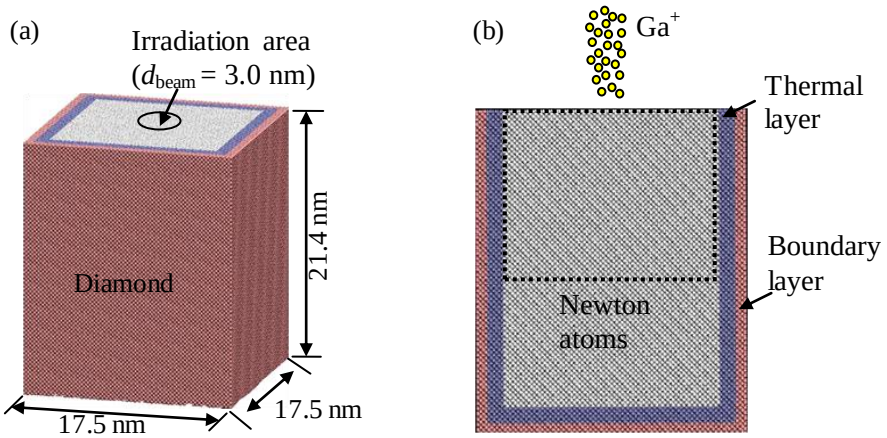

Figure 3-8: Multi-particle collision MD simulation model. (a) The dimensions of the diamond bulk model (front view). (b) A cross-sectional view of the workpiece. The dotted line in figure 3-8 (b) indicates the core collision area selected for temperature analysis.

3.5.3 Results and discussions

Figure 3-9 shows the inside view of the defects formed in diamond bulk after multi-particle irradiation. The cyan atoms represent the dangling bonded C atoms and purple atoms represent sp^2 bonded C atoms. The defects are found at the first few atomic layers. As shown in figure 3-9 (a), the implanted gallium particles create a damage region with a diameter of 6.0 nm, approximately an area of 28.3 nm^2, which is nearly four times the irradiation area (defined as 7.065 nm^2). The thickness of the residual damaged layer is about 14.9 nm.

Figure 3-9 (c) shows the distribution of all the implanted gallium particles (yellow colour) after the collision. The implanted gallium particles are uniformly distributed in the damaged layer. The simulated maximum depth of the implanted Ga was 10.5 nm. No gallium ion was found to move deeper into perfect diamond crystal for the current beam voltage used. The experimental validation will be introduced in the next chapter.

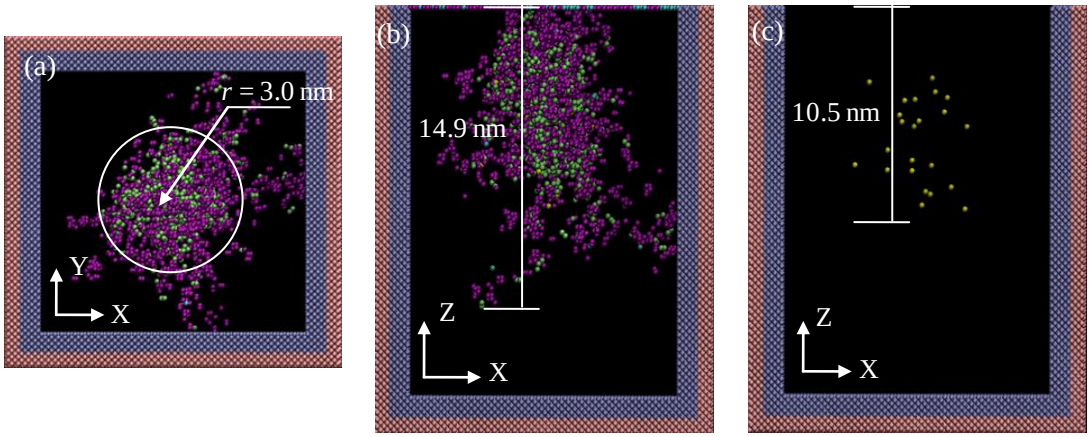

Figure 3-9: The internal images of the damaged area after 8 keV Ga particles collision with a fluence of 4.0×10^{14} ions/cm^2. (a) Plan view of amorphous region; (b) cross-sectional view of amorphous region; and (c) the distribution of the implanted gallium particles. The cyan atoms represent the dangling bonded C atoms and purple atoms represent sp^2 bonded C atoms. The yellow atoms represent the implanted gallium ions.

3.6 Summary

This chapter was dedicated to providing a detailed description on how the multi-particle collision MD model was built. After an introduction of the concept and the background of the subject, this chapter provided all the important parameters which were required to a successful MD simulation of the energetic ion bombardment. By summarising the potential functions used in the previous MD studies of ion bombardment, it was shown that a combination of the Tersoff potential with the ZBL potential was appropriate for the study of FIB-induced damage in diamond. The post-processing tools used to analyse the MD simulation results such as the calculation of atomistic equivalent temperature and the methods used for the quantification of atomic defects, were also comprehensively described. Taking a straightforward example of the single ion collision, the formation of atomic defects under energetic ion collision was obtained. Based on the simulation results and the characterization of the spatial distribution of ions in the ion beam, a new scheme was developed to build up the random multi-particle collision model. The simulation results describe the FIB-induced damage process under low ion beam energy of 8 keV. This MD model will be used in the coming Chapter 4 to further study the dynamic damage process of FIB machining diamond in combined with TEM experiments.

Chapter 4 Experimental and simulation study on FIB-induced damage in diamond tools

4.1 Introduction

In recent decades, a variety of experimental techniques including Raman spectroscopy [131], secondary ion mass spectrometry (SIMS) [143], and transmission electron microscope (TEM) [45, 46] have been used to study the FIB processing damages in diamonds. In this chapter, the focus will be on the nanocharacterisation of FIB-induced damage in a single crystal diamond tool. A TEM was used to characterise the damaged layer in the diamond tool irradiated by FIB under different irradiation conditions. The multi-particle collision MD simulation model developed in Chapter 3 was employed to simulate the ion irradiation process. A dynamic ion-induced damage model was proposed based on the obtained simulation and experimental results. The analysis will be an important guide for any application where a commercial FIB LMIS system is used in processing or analysing diamond.

4.2 Experimental setup

4.2.1 Facilities for ion-induced damage study

TEM is a useful technique in studying structural properties and damage effects. Energy-filtered transmission electron microscopy (EFTEM) is a technique used in TEM equipment, in which only electrons of particular kinetic energies are used to form images or diffraction patterns. In current project, the FIB irradiated sample was examined by FEI Tecnai T20 transmission electron microscopes (TEMs) operated at 200 keV. The microscope's EFTEM lens programme can achieve high magnifications up to 1,000 kx, which is suitable for high-resolution imaging of atomic columns.

In addition, electron diffraction performed in a typical TEM or SEM system is commonly

used in solid state physics and chemistry to study the crystal structure of solids. The convergent beam electron diffraction (CBED) integrated in the TEM system can reveal the full 3D symmetry of the crystal, and thus it was performed to characterize the crystal structures of the irradiated region. The essential specification of the TEMs is listed in Appendix II.

4.2.2 Sample preparation and measurements

In this study a FEI Nova 200 nanolab dual beam FIB system with Ga ion source was used for both the ion irradiation of a diamond tool and the TEM sample preparation. The ion implantation was carried out normal to the rake face of a diamond tool ((1 0 0) lattice plane) with an irradiation area of $2.0 \times 0.5\ \mu m^2$. We chose this angle for analysis because a smooth surface and uniform thickness of amorphous carbon layer can be developed. Three acceleration voltages, 8 kV, 16 kV, and 30 kV were used to mill the irradiation area to the same depth of 0.5 μm. The ion fluences were 9.71×10^{20} ions/cm^2, 7.75×10^{20} ions/cm^2, and 7.54×10^{20} ions/cm^2 for the acceleration voltages of 8 kV, 16 kV, and 30 kV, respectively.

TEM sample preparation procedure is summarized in figure 4-1. After the irradiation, the diamond sample was covered with Pt stripes deposited through a standard e-beam deposition process to protect the created damaged layer from additional Ga^+ implantation during the following TEM sample preparation procedures. After the e-beam deposition, ion-beam Pt deposition was used to further deposit a thick Pt cover to avoid the charging effect and to protect the interested area during the TEM sample thinning process. The cross-sectional TEM sample was prepared using the standard lift-out technique, described in [205].

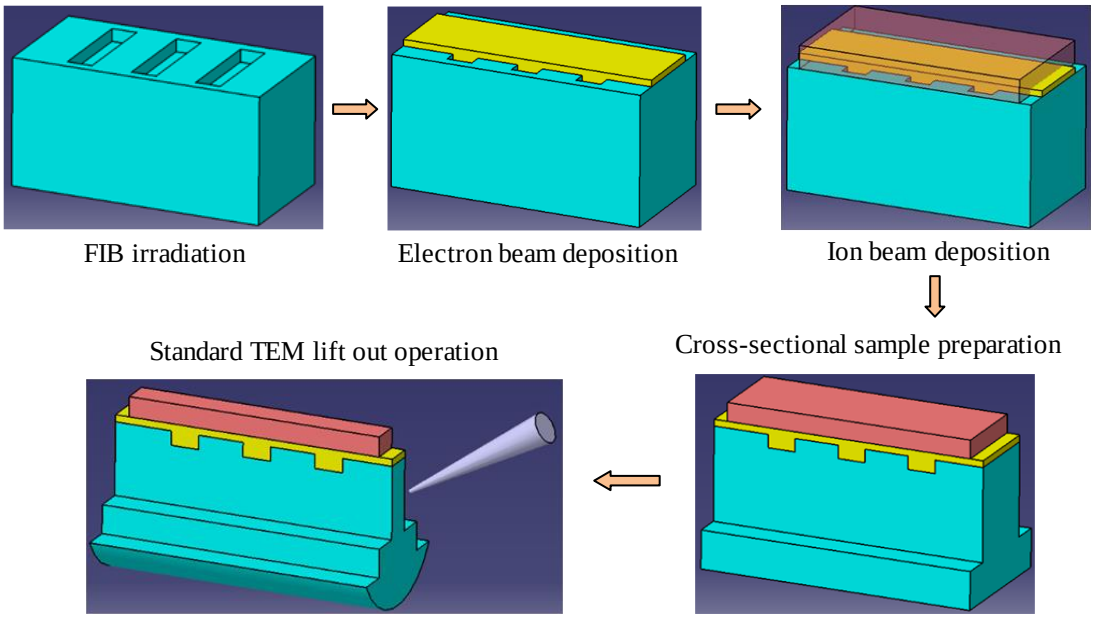

Figure 4-1: The procedure of FIB irradiation and TEM sample preparation.

The secondary ion source damage/pollution is a common problem with TEM sample preparation when using gallium LMIS FIB system. In general, the strategies to solve this problem can be classified as the followings: (1) low energy ion milling in the range of 1-5 kV [43, 135, 206]; (2) low power plasma cleaning with Ar [135, 206] or a 4:1 ratio Ar/O mixture [207] after FIB etching; and (3) chemical treatment with HCL or HNO3. Because the latter two methods are multi-step and will tend to reduce the specimen overall thickness due to their abrasive natures, in this study, the sample was further thinned to electron transparency with the thickness less than 100 nm through the low energy FIB milling method. The final TEM sample is shown in figure 4-2 (a).

4.3 MD simulation setup

In order to shed light on the formation mechanism of FIB-induced damaged layer under different ion irradiation conditions, the large scale multi-particle collision MD model developed in the previous chapter was employed to simulate the ion irradiation process. Because the interval time between each ion collision depends significantly on the energies of

the incident particles and the properties of target materials, single ion collisions under different beam voltages were carried out firstly to determine the time slots used for setting up the multi-particle collision model. For the purpose of concision, the simulation parameters are listed in Table 4-1 as show below.

Table 4-1: MD simulation parameters for ion collsion under 8kV and 16kV

Simulation Parameters	8kV irradiation	16kV irradiation
Workpiece material	Diamond	Diamond
Workpiece dimensions	$50a_1 \times 50a_1 \times 60a_1$ (a_1 = 3.567 Å)	$50a_1 \times 50a_1 \times 60a_1$ (a_1 = 3.567 Å)
Number of atoms	1,217,184	1,217,184
Sputtered area (d_{beam})	3 nm	3 nm
Incident angle	0 º	0 º
Interval time	21.5 ps	26.5 ps
Time step	0.1fs	0.1fs
Initial temperature	293K	293K
Ion fluence	3.0×10^{14} ions/cm^2	3.0×10^{14} ions/cm^2

4.4 EFTEM observation of the damaged layer

The cross-sectional EFTEM images of the damage areas in diamond after the FIB irradiation are shown in figure 4-2. The FIB sputtered regions under different beam voltages are markedly visible below the deposited Pt cover. Because the electrons will be scattered in arbitrary directions in amorphous materials, the absence of any diffraction contrast in the damage areas indicates that the lattice structures of the damaged layers are amorphous (as shown in figures 4-2 (b)-(d)). Moreover, the thickness of ion-induced damaged layer increases with the beam energy. The measured thicknesses of the damaged layers were 11.5 nm, 19.4 nm, and 27.6 nm for the beam voltages of 8 kV, 16 kV, and 30 kV, respectively.

Moreover, noticeable dark patches were found at the interface between a-C layer and the diamond bulk. These dark regions may result from the increase of local density of that area caused by the high concentration of the implanted gallium particles (figures 4-2 (c) and (d)). Additionally, the dark region observed inside the diamond bulk might be the aggregated form of nitrogen which is usually found in natural single crystal diamonds.

In addition, elemental mapping was carried out to determine the relative gallium and carbon distribution in the damaged regions. As shown in figure 4-3, the visible white areas indicate the distribution of the targeted element. Figures 4-3 (a)-(c) represent the mapped carbon distributions, and figures 4-3 (d)-(f) represent the mapped gallium distributions. Compared with the sharp and narrow Ga signal maps of 16 kV and 30 kV irradiations, a wide fuzzy Ga signal (figure 4-3 (d)) was observed for the 8 kV FIB irradiation. This phenomenon might be linked to the fact that a larger Ga^+ dose is required when sputtering the same volume of diamond materials using a low beam voltage.

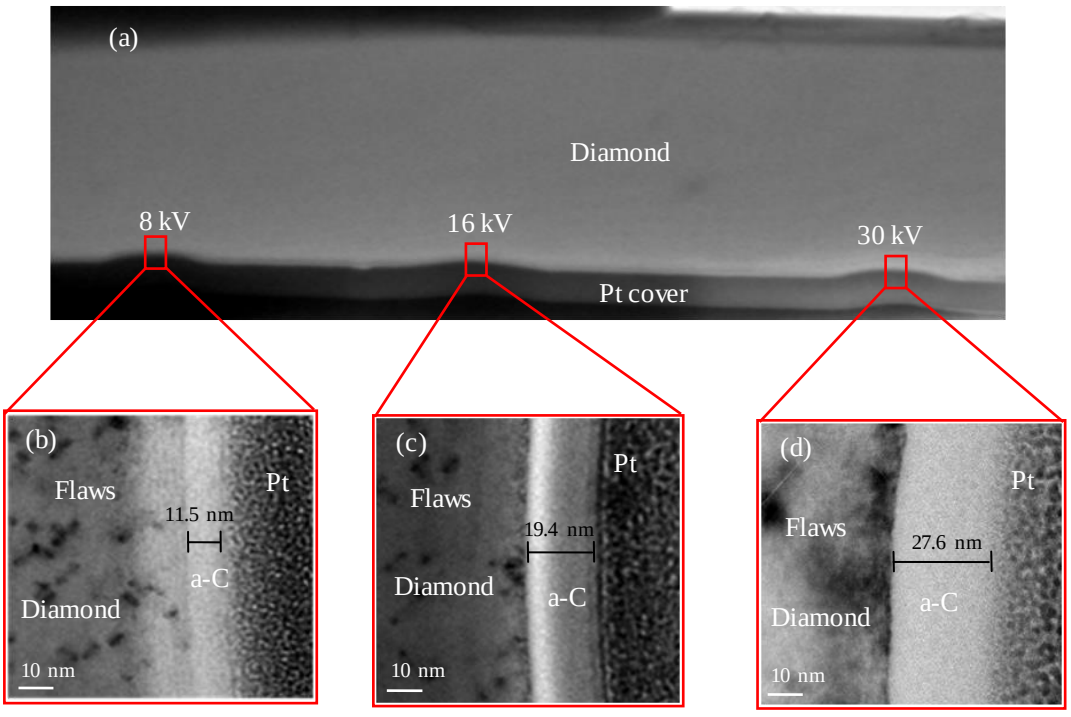

Figure 4-2: EFTEM images of the ion-induced damage areas. (a) The TEM sample after thinning; (b)-(d) are the EFTEM images showing the ion-induced damaged layers formed

under beam voltages of 8 kV, 16kV, and 30kV, respectively.

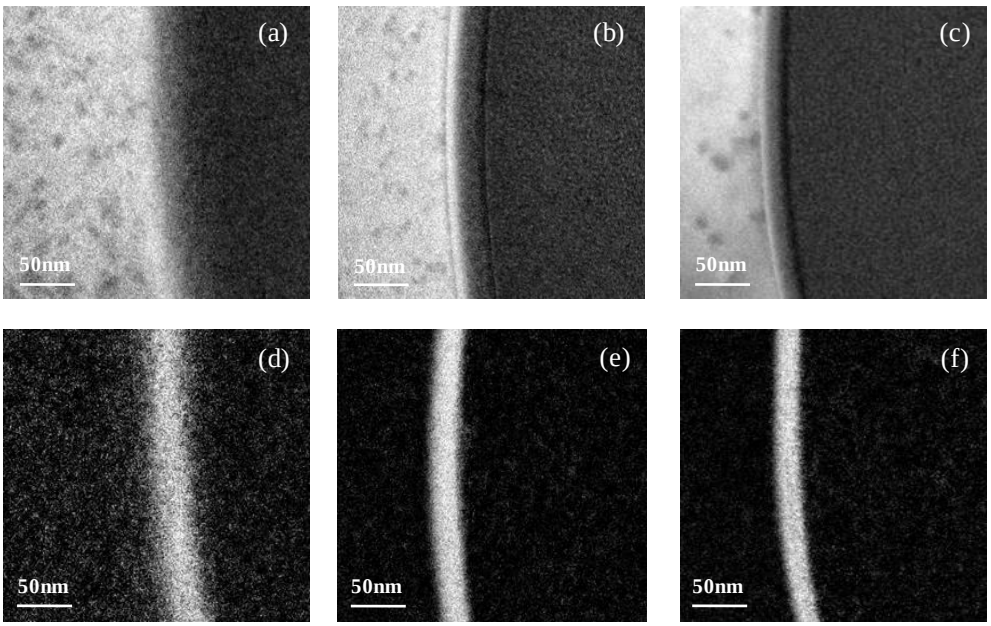

Figure 4-3: EFTEM images of the mapped elements distributions. (a)-(c) represent the mapped carbon distributions; (d)-(f) represent the mapped gallium distributions. (The applied beam voltages are 8 kV (left column), 16 kV (middle column), and 30 kV (right column)).

4.5 Characterization of the damaged region

As discussed above, the thicknesses of the FIB-induced damaged layers in the diamond tool are in a range of tens of nanometres depending on the beam voltage. In order to further characterise the lattice structure of the damaged layer, CBED tests were carried out with the electron beam focusing onto the centre of damaged regions. The diameter of the spot is around 20 nm. For reference, the CBED patterns of the single crystal diamond bulk and the deposited Pt cover were measured and shown in figures 4-4 (a)-(c).

Figures 4-4 (d)-(f) list the CBED patterns of the damaged layers created under beam voltages of 8 kV, 16 kV, and 30 kV, respectively. It is found that the diamond signal in the CBED pattern of low beam energy irradiation (lightly damaged under 8 kV) was remarkably stronger than that of the high energy irradiation (heavily damaged above 16 kV). The

irradiation of the diamond tool at an increasing beam voltage results in a decrease in the lattice short-range order, signifying an increase of the number of non-diamond phase. This increase is associated with the growth of the number of sp^2 bonded C atoms which eventually leads to the formation of a stable amorphous layer at the near surface.

Moreover, since the amorphous signal of the CBED pattern is resonantly enhanced when the high beam voltages were used (figures 4-4 (e)-(f)), the muzzy of the diamond signal in the CBED patterns proves that the irradiation has created non-diamond clusters in the diamond matrix. The highly damaged layer is expected to have lower mechanical properties as compared with the bulk of diamond. Thus, a low FIB processing voltage is recommended when tailing the diamond tool tip.

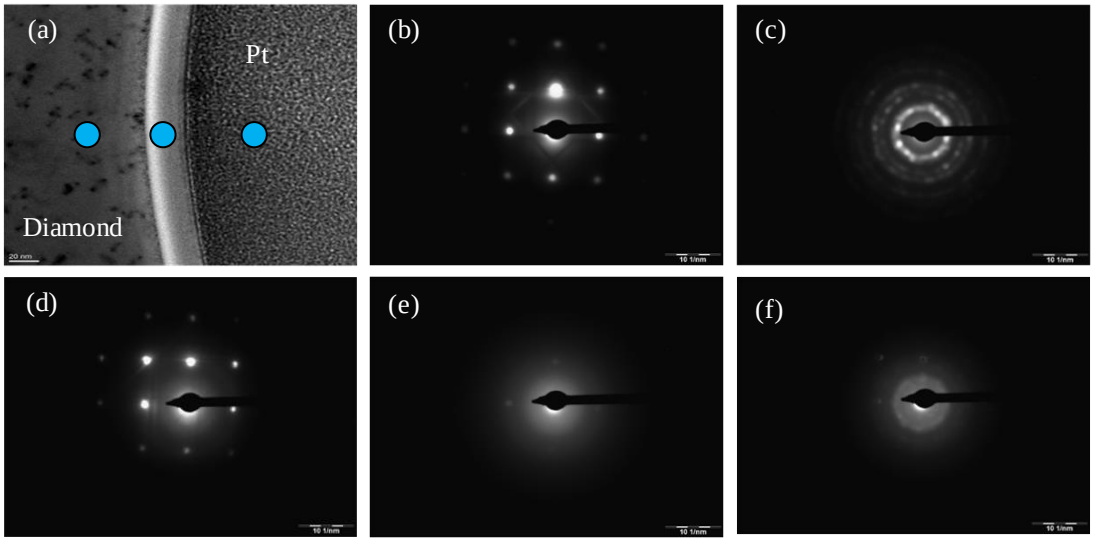

Figure 4-4: CBED analysis of the damage regions under different FIB irradiation voltages. (a) A zero-energy-loss TEM image of FIB irradiated area with the blue spots to schematically indicate the electron beam focusing point when carrying out the CBED tests; (b) CBED pattern of diamond bulk; (c) CBED pattern of Pt cover; (d)-(f) CBED patterns of damaged layers created under beam voltages of 8 kV, 16 kV, and 30 kV, respectively.

4.6 Dynamic ion damage in FIB maching

4.6.1 Damage simulated by multi-particle collision model

Figures 4-5 and 4-6 compare the inside view of the atomic defects formed in diamond as well as the distributions of implanted Ga particles under different beam voltages. The cyan atoms represent the dangling bonded C atoms and purple atoms represent sp^2 bonded C atoms. The simulation results show that the thicknesses of atomic defects formed by 8 keV and 16 keV collisions are all around tens of nanometres. Compared with the 8 keV multi-particle collision, an apparent larger volume of damaged region was formed by the 16 keV collision. The diameters of the core damaged regions are 6.0 nm and 7.2 nm for 8 keV and 16 keV collisions, respectively. The thickness of the residual damaged layer for 8 keV impact is about 14.5 nm, while a larger value of 19.6 nm was found for the 16 keV collision. The atomic defects observed at the bottom of diamond were resulted from the channelling effects [166]. Thus, the MD simulation results compare closely with the corresponding data derived from experiments as discussed above.

Moreover, the maximum depth of the implanted gallium ions (yellow colour) increased with the ion kinetic energy (figure 4-5 (c) and figure 4-6 (c)). The implanted gallium particles tend to distribute in the a-C layer towards the interface of a-C and diamond bulk. No significant gallium particle was found to move deeper into the bulk diamond crystal for the beam voltages applied. As a result of the implantation of gallium particles, the local density of the interface of a-C and diamond bulk is slightly larger than the upper surface. This phenomenon agreed well with the dark patches located at the interface between a-C layer and the diamond bulk observed in the EFTEM images (figures 4-2 (c) and (d)).

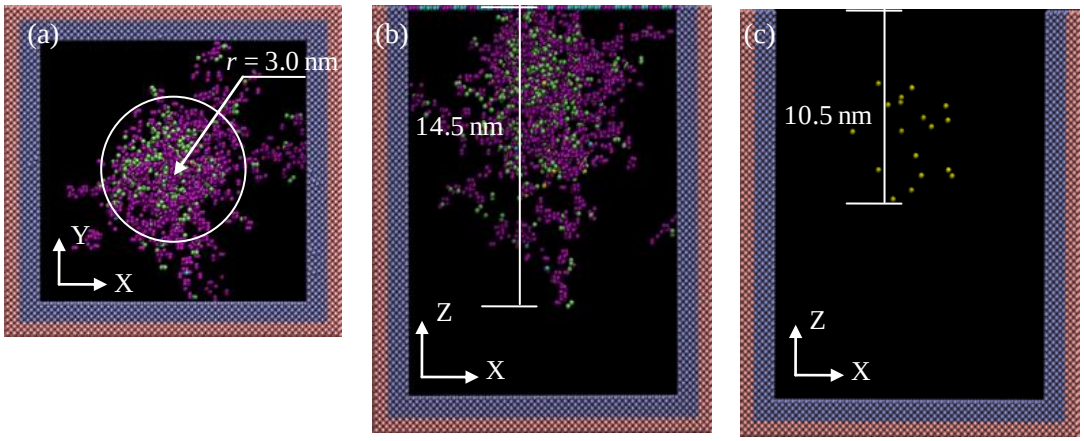

Figure 4-5: The internal images of the damaged area after 8 keV Ga^+ implantation with a fluence of 3.0×10^{14} ions/cm^2. (a) Plan view of amorphous region; (b) cross-sectional view of amorphous region; and (c) the distribution of the implanted gallium particles. The cyan atoms represent the dangling bonded C atoms and purple atoms represent sp^2 bonded C atoms. The yellow atoms represent the implanted gallium particles.

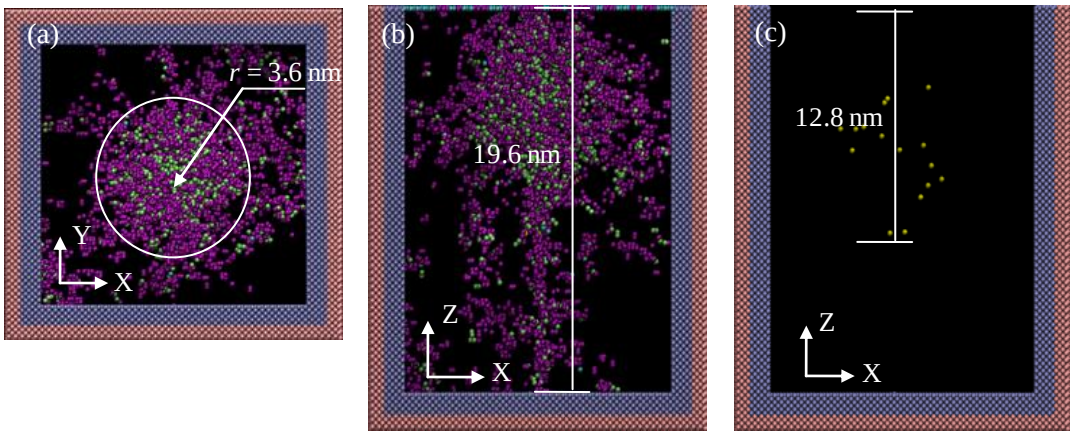

Figure 4-6: The internal images of the damaged area after 16 keV Ga^+ implantation with a fluence of 3.0×10^{14} ions/cm^2. (a) Plan view of amorphous region; (b) cross-sectional view of amorphous region; and (c) the distribution of the implanted gallium particles. The cyan atoms represent the dangling bonded C atoms and purple atoms represent sp^2 bonded C atoms. The yellow atoms represent the implanted gallium particles.

In addition, the radial distribution functions (RDF), g(*r*), of the damaged zones created during the collisions are calculated and shown in figure 4-7. Ideally, for a diamond crystal, g(*r*) is centred at diamond bond length (1.54 Å) for the short-range order. After the collision, the peak values of g(*r*) within a single lattice were reduced and the peak at the shortest distance (1.54 Å) becomes apparently broader, signifying the characteristic to the g(*r*) of amorphous structure. The peak value of g(*r*) was found to be decreased with the increase of the energy incident particles, indicating that high energetic collision can create high disordered clusters in the diamond matrix. Therefore, the simulation results agree with the CBED results discussed before. The nature of FIB-induced damaged layer in the diamond tool is a mixture phase of sp^2 and sp^3 hybridization and accommodates a proportion of the implanted gallium.

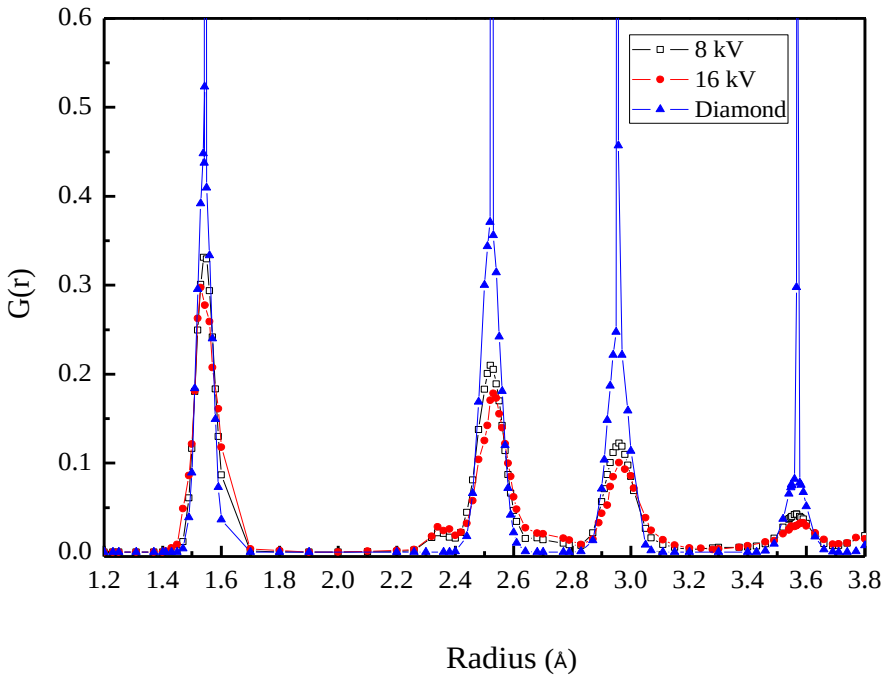

Figure 4-7: The RDF distribution of irradiation area under different beam voltages.

4.6.2 Dynamic damage process under different beam voltages

The phase transition of diamond under energetic ion irradiation has received increasing

interest in recent years [42, 178, 179, 208]. Currently, it is extremely difficult to perform a real-time TEM observation of the dynamic damage process. In contrast, the MD simulation offers an alternative approach in providing both a qualitative and quantitative description of damage production in solids.

Figure 4-8 shows the local temperature evolution of the first ion collision. As compared with the 8 keV collision, a higher peak value of the local temperature (1454.6 K) and a longer life time of the local high temperature spike (above 800 K) were observed for the 16 keV collision. This difference enabled the incident Ga particle with a higher impulse to move deeper into the diamond bulk, and thus generated a thicker atomic defects layer after multi-particle collision. The high local temperature would also soften the C-C bond strength of diamond and provide the necessary thermal energy required by the phase transition from sp^3 hybridization to sp^2 hybridization.

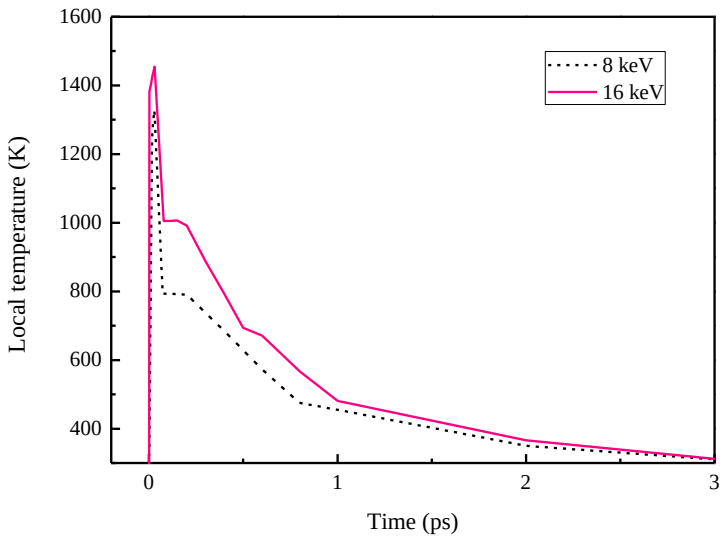

Figure 4-8: The evolution of local temperature for the first ion collision.

Moreover, the high local temperature would also result in a local recrystallisation of the atoms in non-diamond phase. Figure 4-9 compares the evolution of the number of atomic defects for the first ion collision with different energies. It is found that the number of atomic defects reaches a peak value and then partly re-crystallises back to diamond structure. More

atomic defects are created under 16 keV collision. The whole recrystallisation process completed in about 0.8 ps, and the numbers of the residual defects are 271 and 416 for 8 keV and 16 keV collisions, respectively.

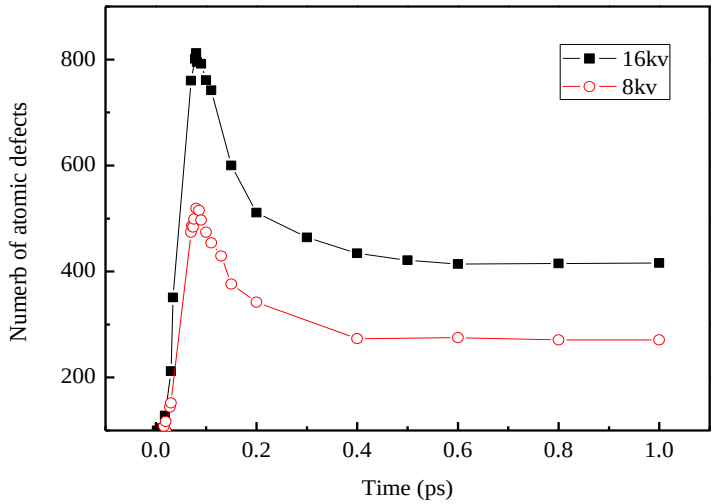

Figure 4-9: The variation of the number of defects during the first ion collision.

Furthermore, with the increase of ion dose, the defects created inside the diamond matrix undergo an accumulation process. The yields of sp^2 bonded atoms per ion were summarized in figure 4-10. It is found that the yield gradually decreases with the increase of ion dose. This might be due to the fact that the atomic defects created by the former ion collision will be annealed in part during the subsequent ion collision process. It is anticipated that as a result of the multiple energetic Ga^+ collisions, a stable a-C layer can be formed when a threshold of damage density was reached [131].

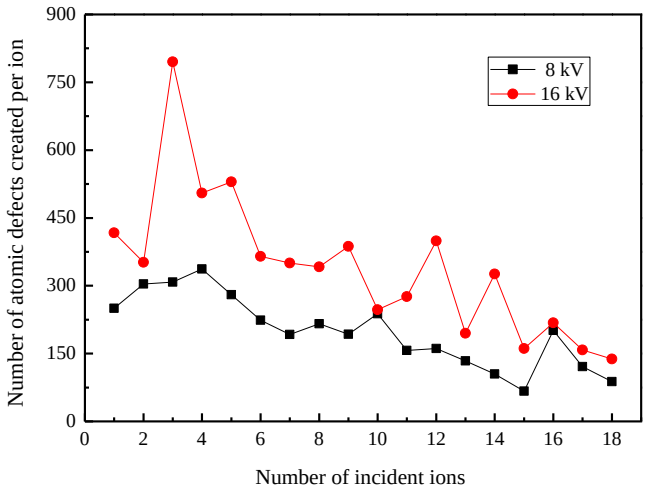

Figure 4-10: The yield of the sp^2 bonded atoms for each ion collision.

Indeed, the non-liner increment of atomic defects indicated that the damaged layer is not a simple accumulation of the defects created by each ion collision. As shown in figure 4-11, the total number of atomic defects is essentially increasing up to an ion fluence of 2.0×10^{14} ions/cm^2; above this ion fluence the curve gradually tends to approach a stable state, depending on the kinetic energy of the incident ion. The reason might be that with the increase of the number of defects, the density of the non-diamond phase's layer increased. The saturation of the non-diamond phase would suppress the formation of new defects. The formation of atomic defects would also result in the alteration of the local physical and chemical properties of diamond, and change in the ion sputter yield. It is therefore anticipated that after reaching a critical ion dose, at which the increased material removal rate reaches the damage formation rate, a stabilization of the a-C layer is likely to be obtained.

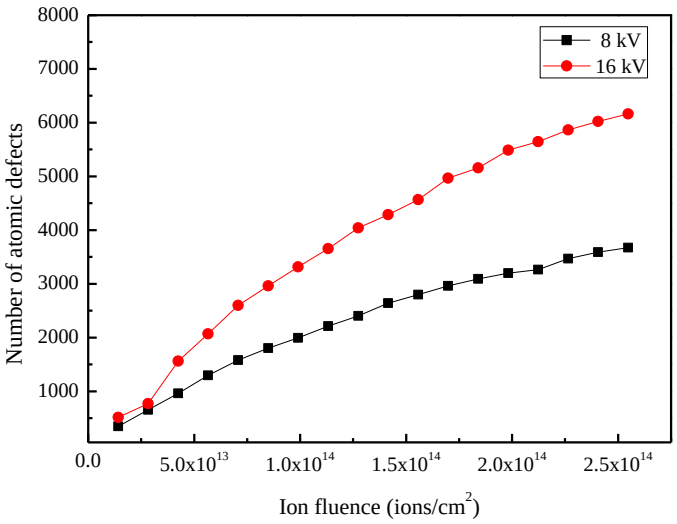

Figure 4-11: The variation of the number of the atomic defects with the ion fluence.

Most recently, few attempts have been made to study the ion-induced amorphisation of diamond. Mckenzie *et al.* [45] studied the near-surface microstructure of a single crystal natural conductive diamond under 30 keV Ga^+ irradiation. Their results show that the near-surface microstructure varies with the increase of ion dose and the critical dose for the amorphisation of the diamond surface is 2.0×10^{14} ions/cm^2. A stable amorphous layer (thickness of 35 nm) was found at a high ion dose of 1.0×10^{15} ions/cm^2. For another study of 30 keV Ga^+ sputtered nanocrystalline diamond films**,** the thickness of the damaged layer was found to grow with the ion dose and achieved an equilibrium value of 44 nm [143]. A linear increase of the Ga peak concentration with fluence was found up to ~2.0×10^{16} ions/cm^2 and the Ga content approached a saturation level at about 2.0×10^{17} ions/cm^2 [143]. Their results qualitatively support the dynamic equilibrium damage process observed in present MD simulations. Therefore, it is concluded that the FIB machining is a dynamic equilibrium material damage and removal process. The thickness of the stable damaged layer depends significantly on the beam voltage.

4.6.3 Discussions on optimal fabrication of nanoscale diamond tools

Figure 4-12 shows the P-T phase diagram of carbon. The stable bonding configuration of

carbon at room temperature conditions is graphite [209]. However, the transition from diamond to the stable phase of graphite at normal conditions is extremely slow because of the high energetic barrier between diamond and graphite. The phase transition from sp^3 hybridization to sp^2 hybridization can occur more rapidly when the diamond is exposed to energetic ion irradiation or a high temperature.

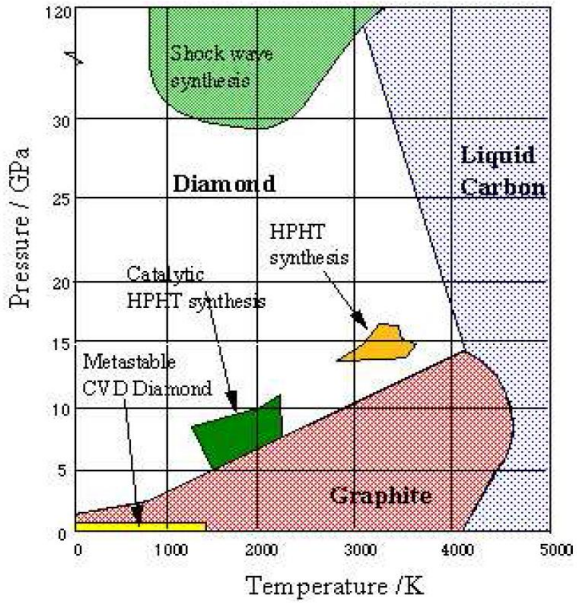

Figure 4-12: P-T phase diagram of carbon [209].

In present study, under all the tested beam voltages, the FIB processing resulted in the amorphisation of diamond. There are two specific amorphous forms of carbon: diamond-like amorphous carbon and graphite-like amorphous carbon. The former has a higher density, and is transparent and much harder than the latter. The EFTEM and CBED measurements indicate that the FIB-induced damaged layer is closer to graphite-like amorphous carbon, especially when the high beam voltage of 30 kV was applied. As a consequence of the large difference in bond strength between the sp^3 hybridization and the sp^2 hybridization, the macroscopic and microscopic properties of the amorphous carbon are quite different from the diamond bulk. Upon cutting, this damaged layer is expected to wear first.

Most recently, Kawasegi *et al.* [147] reported that doping of gallium ion in a diamond tool

(type 1b (1 0 0)-oriented single crystal diamond) can increase the adhesion of work materials to the tool surface and will result in a rapid diamond tool wear. A combination of following heat treatment and aluminium deposition can effectively remove the implanted gallium and improve the tool life of treated tool. However, the wear resistance of the treated tool was still lower than that of a non-irradiated diamond tool, which is mainly due to the residual amorphous layer left on the diamond tool surface.

The present study on ion-induced damage in diamond indicates that the FIB-induced damaged layer should be paid more attention when shaping the cutting edges of diamond tools. The energy-dependent thickness of the damaged layer suggests that finishing the diamond tool with a low beam voltage can minimise the FIB-induced damaged layer during the tool fabrication process. An effective post-processing method is in high demand to further remove the amorphous layer after FIB machining. Future research work is needed to fully explore the advancement of FIB fabrication/shaping technique of diamond tools.

Nevertheless, as the maximum thickness of the damaged layer in diamond tool is about 30 nm, which is 1 part in 10^4 of the functional dimension of a micro cutting tool, the ion damage might be neglected for micro scale applications.

4.7 Summary

In this chapter, a series of experimental works and MD simulations have been carried out to characterise the features of FIB-induced damaged layer in a single crystal diamond tool under different beam voltages. The thickness of ion-induced damaged layer obtained from experiments and simulations has good accordance, which demonstrates the high accuracy achieved by the proposed MD model. The EFTEM measurements of the thickness of the ion-damaged layer, the elemental mapping of the carbon and gallium distribution, and the CBED patterns of the damaged layer demonstrated that the nature of FIB-induced damaged layer in the diamond tool is a mixture phase of sp^2 and sp^3 hybridization and accommodates a proportion of the implanted gallium. The thickness of damaged layer and the

amorphization level of diamond increase with the applied beam voltage.

The MD simulation results informed the interpretation of experimental results by providing both qualitative and quantitative descriptions of the dynamic structural damage production in diamond under different irradiation energies. Compared with the low energy collision, the relatively higher local temperature and the longer life time of thermal spike observed in the high energy collision accelerated the incident Ga particles to move deeper into the diamond bulk, and thus resulted in a thicker damaged layer. The non-liner increment of the atomic defects with the increase of ion fluence signifies that after reaching a critical ion dose, a stabilization of the a-C layer is likely to be obtained. Since the a-C layer will result in early tool wear upon cutting, it should be minimized during the tool fabrication process.

Chapter 5 MD simulation of nanometric cutting of copper by using multi-tip and single tip diamond tools

5.1 Introduction

Although a few introductory reports can be found in the literature describing the high form accuracy and throughput of diamond turning using nanoscale multi-tip diamond tools, the machining mechanisms of nanostructures when using multi-tip tool has not been fully understood up to date. As the tools and the machined structures are in a range of sub-microns or even nanometres, the influence of surface effects such as material side flow and elastic recovery on the integrity of machined nanostructures cannot be ignored. In addition, some critical questions also need to be addressed including the evaluation of the advantages, disadvantages and applicability of this novel technology. The lack of support from a systematic theoretical study has seriously hindered the advance and industrialization of this technique.

As reviewed in section 2.3, the MD simulation method has been effectively used to address some fundamental issues related to nanometric cutting processes of copper such as the emulation of the material removal process [101, 105], the cutting heat generated at different cutting speeds [96], the effect of the depth of cut [210] and the feed rate [101] on the form accuracy of nanostructures, as well as the role of friction in tool wear [95, 96, 104]. Undoubtedly, the theoretic results obtained through simulations will provide valuable feedback and guidance for further development of this new technique.

In this chapter, the nanostructure generation processes, when using a single tip and a multi-tip diamond tool, are modelled by MD simulation method. In order to benchmark the advantages and disadvantages of diamond turning using nanoscale multi-tip diamond tools, a comparison between using single tip and multi-tip nanoscale tools in nanometrc cutting is made from the viewpoint of nanostructure generation, cutting forces and cutting temperature.

5.2 MD nanometric cutting model

5.2.1 Geometric model for MD simulation

The geometry of the cutting tools is shown in figures 5-1 (a) and (b). Both the single tip and the multi-tip diamond tool are created based on perfect diamond crystal structure. The tool-tip width is $W_a = 15a_1$ ($a_1 = 3.567$ Å) with the tool rake angle α being 0 º and the tool clearance angle β being 12 º. To save the computational time, a nanoscale double-tip diamond tool with a pitch of $L = 10a_1$ is employed in current research to represent the nanoscale multi-tip tool. Since the radius of cutting edge of diamond tool is usually larger than the minimum depth of cut in nanometric cutting, in our large-scale MD simulations, all the tool models are built with a round cutting edge with the edge radius of $r = 5a_1$ instead of a sharp cutting tool.

The workpiece has a dimension of $50a_2 \times 80a_2 \times 40a_2$ ($a_2 = 3.615$ Å is the lattice constant of copper) and consists of a boundary layer and a thermostat layer with thicknesses of $2a_2$ and $3a_2$, respectively (as shown in figures 5-1 (c) and (d)). The three orientations of the workpiece are [1 0 0], [0 1 0] and [0 0 1] in the X, Y and Z directions. Free boundary conditions are applied in all directions. Both the nanosized workpiece and the diamond cutting tool were modelled as deformable bodies. During nanometric cutting, the bottom and outer sides of the substrate (atoms in pink colour) are fixed as it has been suggested to be an appropriate configuration to simulate the nanometric cutting process [104, 210].

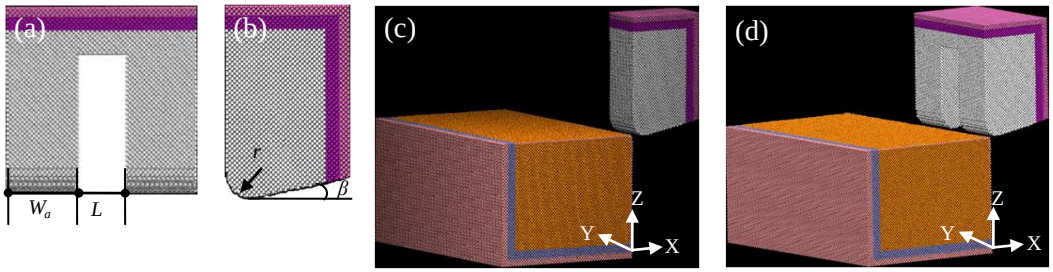

Figure 5-1: Models of MD nanometric cutting simulation. (a) Front view of the multi-tip tool model; (b) right hand end elevation of the tool tip model; (c) single tip tool cutting

model; and (d) multi-tip tool cutting model [211].

5.2.2 Potential functions

In nanometric cutting, hybrid potential functions can be used to describe the interactions between the tool and the workpiece as well as the quantum interactions between electron shells and represent the physical properties of each atom type being simulated, such as elastic constants and lattice parameters. Balamane *et al.* [212] and Smith *et al.* [183] have presented a comprehensive review of the potential energy functions that have been used in recent decades.

In nanometric cutting of copper, there are three different atomic interactions in the MD simulation: (1) the interaction between copper atoms (Cu–Cu) of the workpiece; (2) the interaction between diamond atoms (C–C) of the tool; (3) the interaction between workpiece and tool (Cu–C). For the Cu–Cu interaction the embedded atom method (EAM) potential proposed by Foiles *et al.* [193] is used since it has been widely used in description of metallic materials [96, 105, 213]. As it is shown in Eq. (5-1), the total energy E_{eam} of the atomistic system comprises summation over the atomistic aggregate of the individual embedding energy F^i of atom i and pair potential ϕ_{ij} between atom i and its neighbouring atom j, which can be expressed as:

$$E_{eam} = \sum_i F^i(\sum_{j \neq i}^{n} \rho^i(r^{ij})) + \frac{1}{2} \sum_{ij, i \neq j} \phi_{ij}(r^{ij}) \tag{5-1}$$

where the E_{eam} is the total energy of the atomistic system which comprises summation over the atomistic aggregate of the individual embedding energy F^i of atom i and the pair potential ϕ_{ij} between atom i and its neighbouring atom j. The lower case Latin superscripts i and j refer to different atoms, r^{ij} is the distance between the atoms i and j, and $\rho^i(r^{ij})$ is the electron density of the atom i contributed by atom j.

For C-C atoms, we adopt the Tersoff potential [192] computed as follows:

$$V_{ij} = f_C(r_{ij})[f_R(r_{ij}) + b_{ij} f_A(r_{ij})] \tag{5-2}$$

where V_{ij} is the bond energy, i and j label the atoms of the system, r_{ij} is the length of the ij bond, b_{ij} is the bond order term, f_R is a two-body term and f_A includes three-body interactions, and f_C represents a smooth cut-off function to limit the range of the potential.

The Morse potential function [190] was used to describe the interaction between Cu-C and the total energy E_{tot} is expressed as:

$$E_{tot} = \sum_{ij} D_0 \left[e^{-2\alpha(r-r_p)} - 2e^{-\alpha(r-r_p)} \right] \tag{5-3}$$

where r is the instantaneous distance between atoms i and j. The cohesion energy D_0, the elastic modulus α, and the equilibrium bond distance r_p are 0.087eV, 5.14 $Å^{-1}$, and 2.05 Å respectively [190].

5.2.3 MD simulation set up

All of the cutting tools are applied along the [-1 0 0] direction on the (0 0 1) surface of the copper at a constant cutting speed of 200 m/s. Of course, the simulation may have its own limitations including the need to run at very high cutting speeds, but this may not be a serious limitation as long as we are interested in the general nature of the process without consideration of the speed effects [94]. The main computational parameters used in the MD simulations are summarized in Table 5-1 for reference.

Table 5-1: MD simulation parameters for nanometric cutting of copper [211].

	Single tip with multi-pass	Multi-tip with single pass
Workpiece material	Copper	Copper
Workpiece dimension	$50a_2 \times 80a_2 \times 40a_2$ (a_2 = 3.615 Å)	$50a_2 \times 80a_2 \times 40a_2$ (a_2 = 3.615 Å)
Number of atoms	760, 355	894, 870

Tool tip width	$15a_1$ (a_1 = 3.567 Å)	$15a_1$ (a_1 = 3.567 Å)
Tool rake angle	0 º	0 º
Tool clearance angle	12 º	12 º
Time step	1 fs	1 fs
Initial temperature	293 K	293 K
Depth of cut	1 nm	1 nm
Cutting speed	200 m/s	200 m/s

The equations of atoms motion were integrated using velocity-verlet algorithm with a time step of 1 fs. Moreover, 85,000 time steps were carried out as the relaxation process to adjust the system to 293 K before cutting. During cutting and the thermal annealing processes, the systems were controlled by NVE ensemble and the thermostat atoms were kept at a constant temperature of 293 K through a velocity scaling method to perform the heat dissipation [101]. The velocity scaling method controls the temperature by rescaling the thermal atoms velocities to 293 K if the temperature departs more than 5 K from the specified temperature at a certain time step. Thus, this algorithm allows the heat transferring from shear region to the bulk of the workpiece which conforms to experimental observation.

Figure 5-2 shows the simulation procedure of nanometric cutting and traces of the tool. For single tip tool, it scratched the surface in X-Y plane along the OC direction for the first cutting pass (as shown in figure 5-2 (a)). Then the tool followed trace (C–C1) in the Y–Z plane. The tool moved along line C1A1 and moved down to point A. At last, the tool scratched the second groove along the line AB with same depth of cut (as the dotted line shows). For multi-tip tool, only single pass was taken with the same cutting distance as shown in figure 5-2 (b). All the simulations were performed by high performance computing cluster (HPC) using 24 cores.

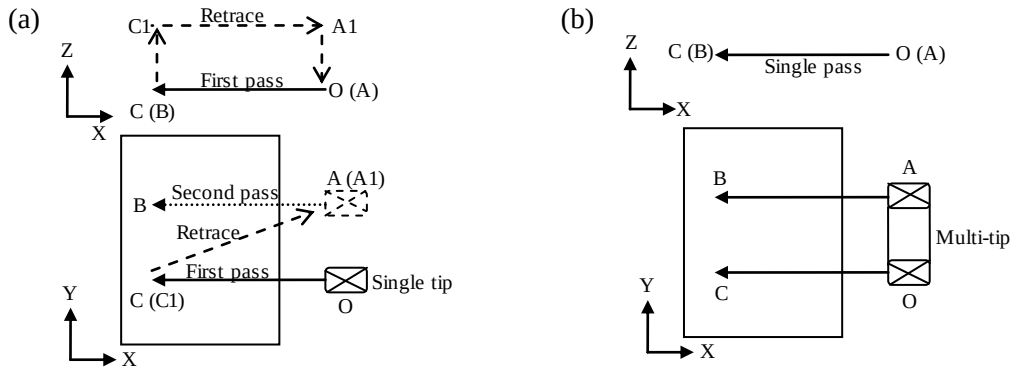

Figure 5-2: Schematic diagram of nanometric cutting traces. (a) Single tip cutting with two passes; (b) Multi-tip cutting with single pass [211].

5.2.4 The post processing methods

5.2.4.1 Calculation of the stresses and cutting forces

In LAMMPS, the stress for each atom is attributed to its interaction with all other atoms in the simulation, and the stress tensor for an atom *i* can be calculated from equation 5-9.

$$S_{ab} = -\left[\begin{array}{l} mv_a v_b + \frac{1}{2}\sum_{n=1}^{N_p}(r_{1a}F_{1b} + r_{2a}F_{2b}) + \frac{1}{2}\sum_{n=1}^{N_b}(r_{1a}F_{1b} + r_{2a}F_{2b}) \\ + \frac{1}{3}\sum_{n=1}^{N_a}(r_{1a}F_{1b} + r_{2a}F_{2b} + r_{3a}F_{3b}) + \frac{1}{4}\sum_{n=1}^{N_d}(r_{1a}F_{1b} + r_{2a}F_{2b} + r_{3a}F_{3b} + r_{4a}F_{4b}) \\ + \frac{1}{4}\sum_{n=1}^{N_i}(r_{1a}F_{1b} + r_{2a}F_{2b} + r_{3a}F_{3b} + r_{4a}F_{4b}) + \mathrm{Kaspace}(r_{ia}, F_{ib}) \end{array}\right] \quad (5\text{-}4)$$

where *a* and *b* denote *x, y, z* to generate 6 components of the symmetric stress tensor. The first term of the equation is a contribution due to the kinetic energy of atom *i*. The second term is a pair-wise energy contribution where *n* loops over the N_p neighbours of atom *i* and r_1 and r_2 are the positions of the two atoms in the pair-wise interaction. F_{1b} and F_{2b} are the forces on the two atoms resulting from the pair-wise interactions. The third term is a bond contribution over the N_b bonds of atom *i*. There are similar terms for N_a angle, N_d dihedral, and N_i improper interactions. Kspace term represents long-range Coulombic interactions.

The tensor for each atom has 6 components and is stored as a 6-element vector in the following order: σ_{xx}, σ_{yy}, σ_{zz}, τ_{xy}, τ_{xz}, τ_{yz}. However, it is noted that the per-atom stress is really a stress-volume formulation. In order to generate continuous matter, it would need to be divided by a per-atom volume to have units of stress. The hydrostatic stress (σ_{hydro}) and von Mises stress (σ_{von}) can be further computed using the following equations:

$$\sigma_{hydro} = \frac{\sigma_{xx} + \sigma_{yy} + \sigma_{zz}}{3} \tag{5-5}$$

$$\sigma_{von} = \sqrt{\frac{(\sigma_{xx} - \sigma_{yy})^2 + (\sigma_{xx} - \sigma_{zz})^2 + (\sigma_{yy} - \sigma_{zz})^2 + 6(\tau_{xy}^2 + \tau_{yz}^2 + \tau_{xz}^2)}{2}} \tag{5-6}$$

For cutting forces, action and reaction are opposite and equal. Since it is quite difficult to accurately measure the volume of the workpiece in cutting zone, the cutting forces were obtained by summing the forces of tool atoms. In LAMMPS, this can be done using "stress/atom" command followed by a "reduce sum" command. A schematic diagram of the forces directions is shown in figure 5-3 (b).

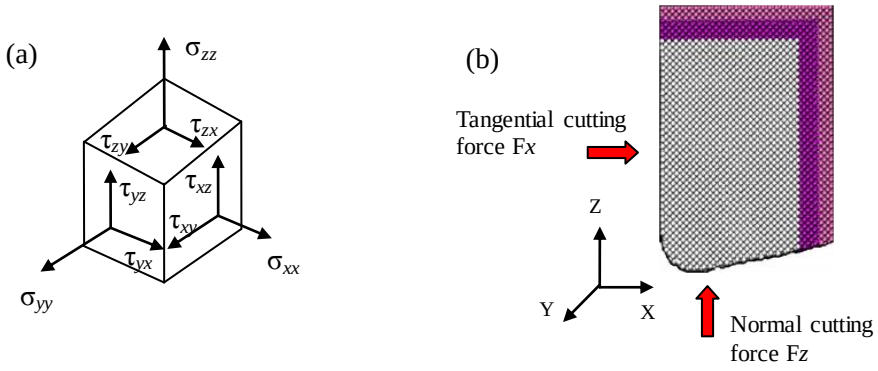

Figure 5-3: Schematical diagrams of the stresses and cutting forces. (a) Stress directions; and (b) the direction of cutting forces.

5.2.4.2 Calculation of the cutting temperature

Cutting heat has been regarded as one of the key factors to influence the quality of the

generated nanostructures as well as the tool life in nanometric cutting process. According to the law of equipartition of energy, the representative temperature of a group of atoms can be calculated from the total atomic kinetic energies of the group. As the nature of the temperature is statistical, the instantaneous kinetic energy of each atom during nanometric cutting differs significantly from the temperature of the bulk. Therefore, the measurement of cutting temperature is not straight forward.

In order to more accurately characterize the variation of temperature during the cutting process, we employed the concept of atomistic equivalent temperature T_i discussed in section 3.3.1 to analyse the cutting temperature. A cut-off distance $r_0 = 4a_0$ was used to select atoms as it can reflect the thermal feature of the short-range structure of copper lattice during nanometric cutting processes. It is noted that only the thermal velocities of atoms are used to compute the temperature. The kinetic energy contributed by the advection movement of the tool should be subtracted beforehand.

5.2.5 CSP

Dislocations play a crucial role in governing the plastic response of ductile materials. The thermal vibration of atoms at finite temperatures makes it difficult to observe dislocations in a thermal sensitive environment. The widely used methods for tracing such dislocations and other lattice defects are coordinate number analysis, slip vector, and centro-symmetry parameter (CSP). It has been reported that centro-symmetry parameter (CSP) is less sensitive to the temperature increase compared with other methods such as atomic coordinate number and the slip vector [50]. The CSP method proposed by Kelchner *et al*. [214] quantifies local deviations from centro-symmetry in a given centro-symmetric structure such as FCC and BCC (body centred cubic). The centro-symmetry parameter P_i is defined as follows,

$$P_i = \sum_{i=1}^{6} \left| \vec{R}_i + \vec{R}_{i+6} \right|^2 \tag{5-7}$$

where $\overrightarrow{R}_i$ and $\overrightarrow{R}_{i+6}$ are the position vectors corresponding to the six pairs of opposite nearest atoms. The parameter P_i increases from 0 for perfect FCC lattice to positive values for defects and for atoms close to free surfaces. In the case of the single crystal copper, the default value of P_i corresponding to those atomic defect structures and its representing colour are indicated in Table 5-2.

Table 5-2: The default value of atomic structural defects in CSP [211].

CSP value P	Lattice structure	Represent atoms colour
P < 3	Ideal FCC structure	Yellow
3 < P < 5	Partial dislocation	Cyan
5 < P < 8	Stacking fault	Blue
8 < P < 21.5	Surface atoms	Orange
P > 21.5	Surface atomic step atoms	Pink

5.3 Results and discussions

5.3.1 Nanostructure generation process

We first simulated the generation process of nanostructures on the copper surface using the single tip tool with two cutting passes. The nanostructure in this thesis means a nano-groove machined on the copper surface by the tools. It should be noted that the distance between two cutting passes is specified as $10a_1$ (a_1 = 3.567 Å) according to the pitch of the multi-tip tool. Figure 5-4 shows the snapshots of nanometric cutting process as well as the atomistic dislocation evolutions in the workpiece when using the single tip tool under a depth of cut of 1.0 nm. Every workpiece atom was coloured by its CSP value. It should be pointed out that the isolated atoms with green colour inside the workpiece are not lattice defects. Those atoms with CSP above three are caused by thermal vibration at a finite temperature [105, 210]. Moreover, the defect-free atoms were removed from the visualizations.

At initial cutting stage, with the penetration of the tool, the lattice of workpiece deformed as buckled, and the outer kinetic energy of tool transmitted onto the workpiece and converted into potential energy stored in the deformed lattice. When the energy or shear stress of copper atoms exceeds a specific level, the atoms tend to re-arrange into lower energy lattice to relax lattice strain through dislocation nucleation (as shown in figure 5-4 (a)). As the tool advances, more dislocations initiate and propagate in preferred (1 1 1) crystal slip planes systems. The pile-ups of atoms in front of the tool rake face lead to the formation of cutting chip (as shown in figure 5-4 (b)). At the same time, dislocations that penetrated the workpiece migrate out towards the machined surface and create atomic sized steps (atoms in pink colour) on the machined surface, which represents the best surface roughness possible. These results agreed well with other analyses on the evolution of dislocation nucleation and propagation during the nanometric cutting process of copper [96, 102].

The second cutting pass was taken along line AB with the same processing parameters (as shown in figure 5-2 (a)). After two consecutive cutting passes, two nano-grooves were machined by the single tip tool (as shown in figure 5-4 (c)). However, it is found that at the end of the second pass, there were some disordered atoms moved into the first nano-groove. This resulted in re-shaping of the right side of the first machined groove due to the lack of support of that side. This phenomenon is recognised as the feed rate effect in the nanometric cutting [101]. When the distance between two passes is less than a critical value, there is a strong possibility that the material plastic side flow (in terms of dislocations movements) created in the second pass will extend to the machined surface of the first cutting, and thus re-shape the first nano-groove. It is noted that this critical value is not fixed as the dislocation nucleation and movements are affected by the tool geometry, depth of cut, cutting speed and local cutting temperature [210].

Similar phenomenon has been reported by Yan *et al*. [101] in their MD study of the AFM scratching of copper. The tool model was built with a round-edged regular three sided pyramid with a hemisphere at the end (radius of the tool cutting edge of 1 nm). Their

investigation showed that the cross-sectional shape of first scratch was very close to that of the second one when the feed reached 3.62 nm [101]. Fang *et al.* [213] qualitatively compared the feed effect behaviour predicted by the MD simulations with the AFM experiments (a diamond AFM tip with radius of 10 nm). Our results agree with their conclusions and further confirm that the feed rate effect also occurs in the rectangular shape tool-tip cutting.

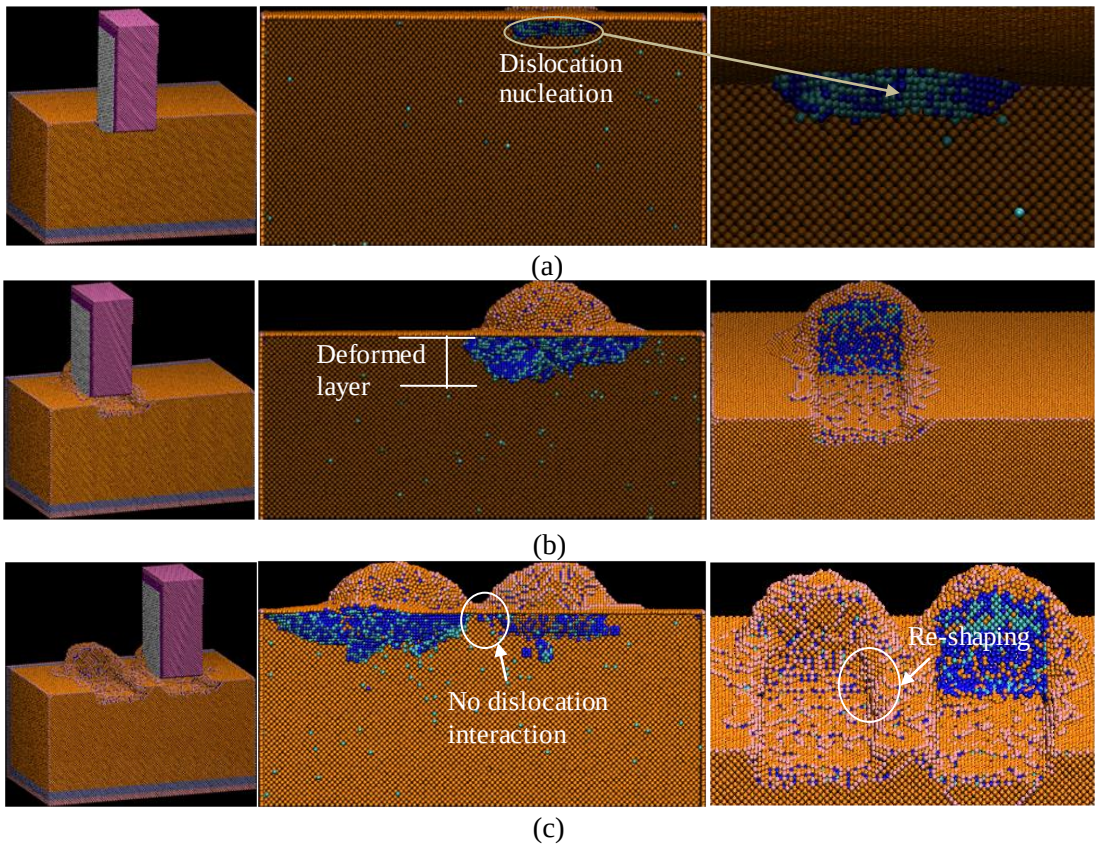

Figure 5-4: Snapshots of cutting process and dislocation evolution of workpiece using a single tip tool with multi-tip passes. (a) Dislocation nucleation; (b) first cutting pass; and (c) the second cutting pass [211].

For multi-tip tool cutting, it can be seen from figures 5-5 (a) and (b) that the initial cutting stage was almost the same as that of single tip tool cutting. The dislocations initiated under

the tool-workpiece contact surface due to the compressive stress induced by the initial impact of the tool tips, and then propagated along the (1 1 1) crystal slip planes. The atoms accumulated and piled up in front of the multi-tip tool, resulting in the formation of two independent initial chips. The increasing of the chip volume indicated that the material deformation states for all cutting conditions were dominated by cutting and accompanied by plough [102].

However, unlike the single tip tool cutting, where the nano-grooves were formed through two cutting passes separately, interactions between the dislocations around tool tips were observed when using the multi-tip tool (as shown by figure 5-5 (b) and (c)). Because two nano-grooves were synchronously generated through a single cutting pass, the effect of feed rate observed in single tip tool cutting can be completely eliminated when using the multi-tip tool. Compared with the nano-grooves machined by the single tip tool cutting, the nano-grooves generated by the multi-tip tool are closer to ideal centre line symmetry (figure 5-5 (c)).

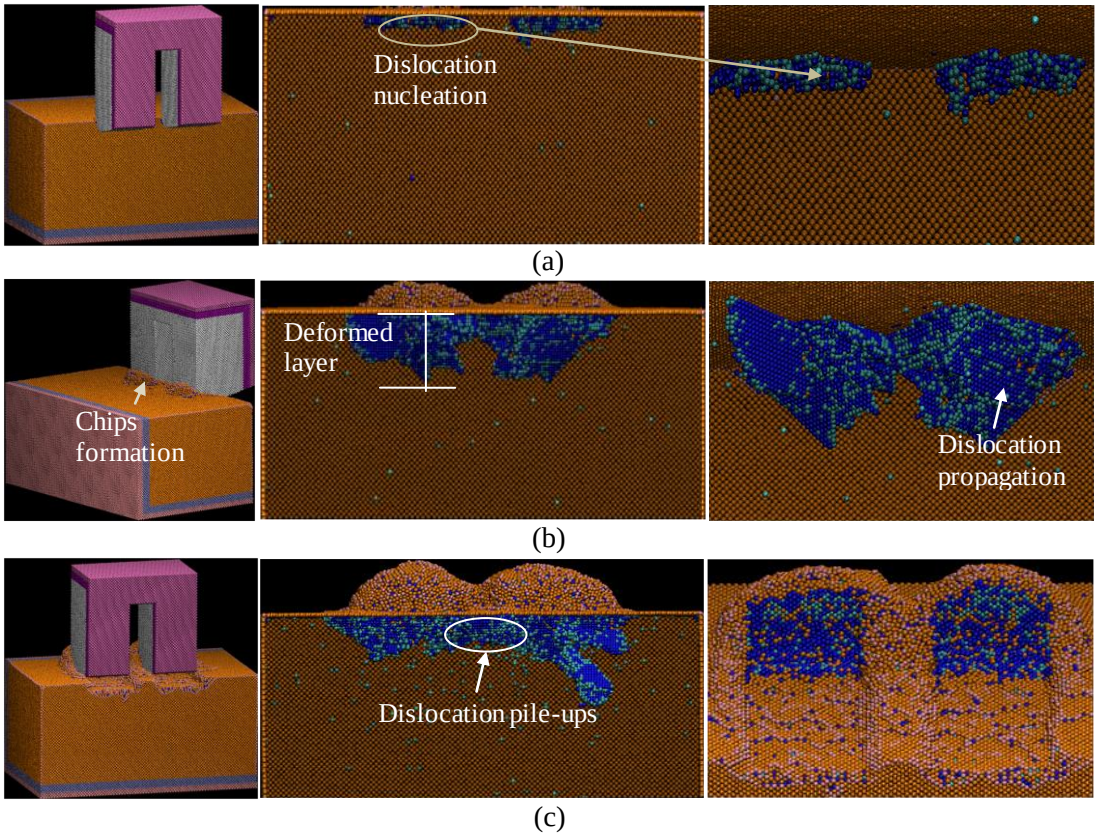

Figure 5-5: Snapshots of cutting process and dislocation evolution in workpiece when using the multi-tip tool at cutting distances of: (a) 2.55 nm; (b) 3.95 nm; and (c) 15.45 nm [211].

5.3.2 Cutting force

The variations of cutting forces during the steady cutting process were summarized in figure 5-6. The comparison was made between the first and the second cutting pass of the single tip tool cutting and the multi-tip tool cutting. The results show that the tangential cutting force F_x and normal cutting force F_z in all simulations are fluctuating around an approximately constant value at the steady cutting stage. The dynamic equilibrium of the tool-workpiece contact area and the activities of dislocations accompanying the material removal process are responsible for the fluctuations. Both the normal and tangential cutting forces of the multi-tip tool cutting were larger than those of the single tip tool cutting (for the first and the second cutting pass). However, the cutting forces in the Y direction were found to have an average

value near zero because of the balanced forces contributing from each side.

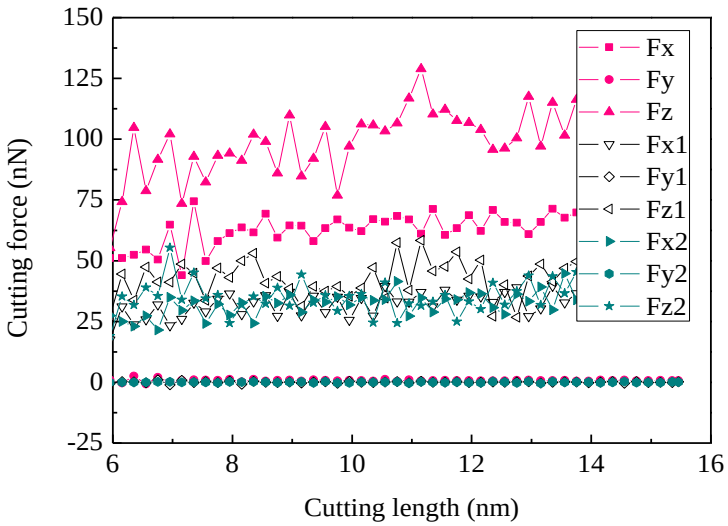

Figure 5-6: The force-displacement curves under a depth of cut of 1.0 nm. F_x, F_y and F_z represent the cutting forces of using the multi-tip tool; F_{x1}, F_{y1}, F_{z1} and F_{x2}, F_{y2} and F_{z2} represent the forces for 1st and 2nd passes when using the single tip tool, respectively [211].

In order to further quantify the difference of cutting forces between using the single tip and the multi-tip tool, the average tangential cutting forces and normal cutting forces at the steady cutting state were calculated (as shown in figure 5-7). It was found that the tangential cutting forces of the first and the second cutting pass when using the single tip tool were nearly the same, but the normal cutting force of second pass was smaller than that of the first pass. The drop of the normal cutting force resulted from the feed rate effect which appeared at the end of the second cutting pass (as shown in figure 5-4 (c)). The material side flows in terms of the dislocation extension released the extra stress during the second pass, and thus lead to a drop of the normal cutting force. For multi-tip tool cutting, while the tangential cutting force per tip has a value of 33.3 nN which is slightly smaller than that of using a single tip tool, the normal cutting force per tip of 54.1 nN is much larger than those observed when using the single tip tool (46.9 nN for the first pass, 38.5 nN for the second pass). The significant dislocations pile-ups beneath the tool tips resulted in a local strengthening of the

material in the normal direction during the multi-tip cutting process.

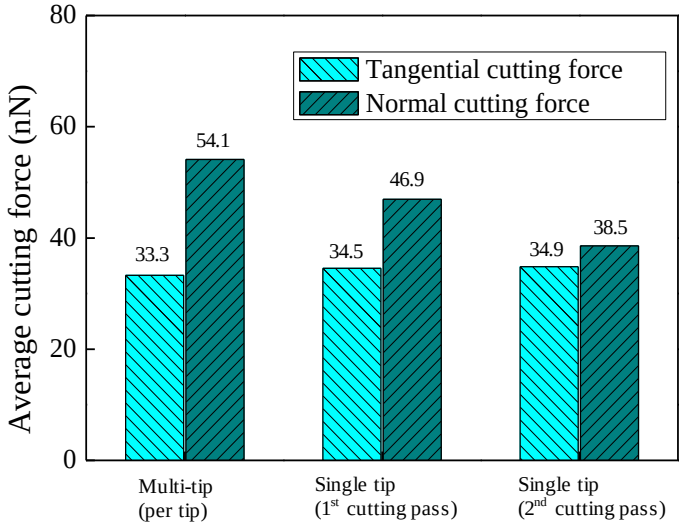

Figure 5-7: The average cutting forces for the single tip tool and multi-tip tool cutting [211].

Moreover, the ratio of tangential cutting force to normal cutting force ($\mu = F_x/F_z$) is used to assess the alteration of local physical property during the nanometric cutting process. From the average forces at the steady stage, we obtain $\mu \approx 0.61$ for multi-tip cutting and a larger average value of 0.82 for the single tip tool cutting. Lin *et al*. have measured the cutting forces in their scratching copper test, and found that the actual tangential cutting force F_x is 2,780.2 nN and the normal cutting force F_z is 5,686.2 nN [104]. The ratio of tangential cutting force to normal cutting force from their experimental data is 0.49. It is noted that our calculated ratio of F_x/F_z is larger than the experimental result because the value also depends on the tool rake angle, and surface smoothness and the crystal structure of materials used. Komanduri *et al.* [215] have investigated the atomic-scale friction at extremely fine scratch depths (from 0.8 nm to almost zero) and pointed out that for tool built with zero rake angle, the force ratio of F_x/F_z can be as large as 1.170.

Recently, Luan and Robbins have argued that the atomic-scale surface roughness produced by discrete atoms had significant effect on the coefficient of friction, and the contact areas and stresses may be changed with the local alteration of friction and lateral contact stiffness

in an order of magnitude [216]. Thus, the difference of the ratio of F_x/F_z observed in the nanometric cuttings between using the single tip tool and the multi-tip tool, may be attributed to the different local tool-workpiece contact status.

5.3.3 Temperature distribution

Figure 5-8 shows the cross-sectional view of the atomistic equivalent temperature distribution for the single tip tool and the multi-tip tool cuttings. Atoms are coloured according to their atomistic equivalent temperature. For better visualization, the white dotted lines are used as the boundaries between the low and high temperature zones (> 550K). It was found that in all simulations, the temperature in shear zone was around 650 K. The range of high temperature region (> 550 K) when using the multi-tip tool was apparently larger than that of using the single tip tool. The highest temperature regions were found at the tool-chip interface slightly towards the workpiece side.

Unlike traditional metal cutting, in this study the diamond tool material is significantly harder than the workpiece material i.e. copper. It is a common knowledge that when the cutting tool material is significantly harder than the substrate, the plastic deformation of the softer work material will be the main heat source [217]. In our MD model, the energy transfer between copper and diamond is described by the selected potential functions. At the interface of the diamond tool and copper substrate, there is an atomic layer (with a thickness of several atoms) which transmits the energy between C and Cu atoms. Copper and the diamond materials both have high thermal conductivity. However, the thermal conductivity of the natural diamond is about 22 W/(cm K) which is five times more than that for copper. As a result, a large temperature gradient towards the cutting tool was observed in figure 5-8. Moreover, the large diamond cutting tool model built in present study also helped to release the cutting heat at the tool cutting edge. Therefore, the diamond cutting tool would have lower temperature than the copper substrate, and the highest temperature regions were found at the tool-chip interface slightly towards the workpiece.

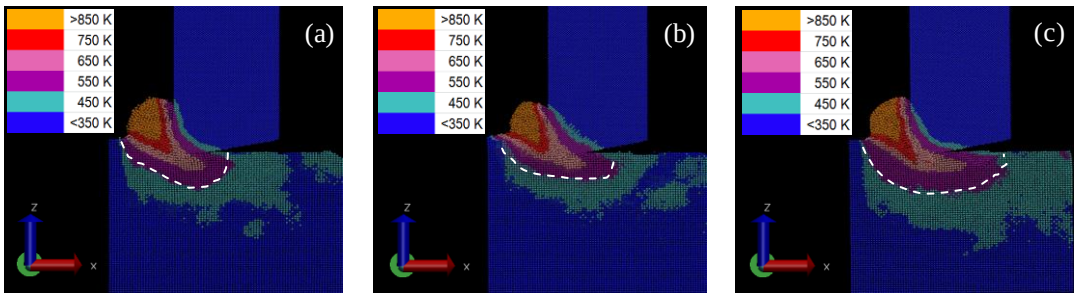

Figure 5-8: The cross-sectional views of the temperature distribution at a depth of cut of 17 nm. (a) Single tip cutting (1st pass); (b) Single tip cutting (2nd pass); (c) Multi-tip cutting with single pass.

In order to further quantify the difference in cutting heat when using different kinds of tools, detailed analysis has been done by comparing the number of atoms in different temperature ranges. For a better comparison, only the workpiece atoms within the cutting zone (z coordinate larger than $20a_2$) were taken into account and the numbers of atoms in different temperature ranges were normalized by the total number of atoms selected (as shown in figure 5-9). It was found that the proportion of atoms with atomistic equivalent temperature larger than 500 K in the multi-tip tool cutting was 8.01% which was apparently larger than that of the single tip tool cutting (being 3.3%). This result quantitatively demonstrated that the cutting heat generated while using the multi-tip tool was much higher than that of the single tip tool cutting.

In addition, the higher cutting temperature observed in the multi-tip cutting also explained the feature of cutting forces discussed in the above section. Although the normal cutting force per tip of the multi-tip cutting was larger than that of using the single tip tool, the tangential cutting force per tip is slightly lower than that of using the single tip tool. This is mainly due to the fact that the much higher local temperature generated during the multi-tip cutting process would result in local weakening of the Cu-Cu bond force, and thus lead to a lower tangential cutting force per tip.

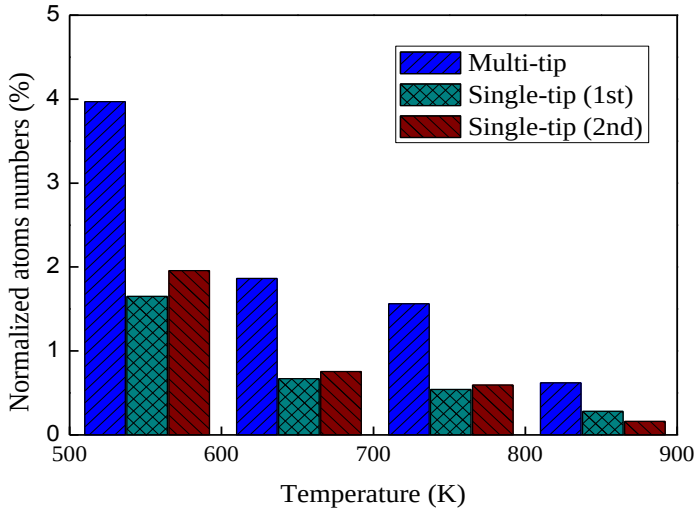

Figure 5-9: The normalized atoms numbers in different temperature ranges [202].

5.3.4 Thermal annealing at machined surface

It has been widely accepted that re-crystallization happens during local annealing process, not only in ductile metallic materials [96] but also in brittle materials such as silicon [174] and diamond [179]. In macro machining practice, after the tool has left the machined region, there is a macroscopic time (~ms) for the machined surface to relax [96]. And by that time, the subsurface atomic defects might be able to get annealed partly. In a nanometric cutting, the thermal effects happen in such a short timescale that to accurately detect and measure the temperature distribution, it requires a thermal measurement system with extremely short response time and high resolution. However, the spectral wavelength of sensors used in most current commercial infra-red thermography are ranging from 0.8 μm to 14 μm with the response time ranging from 2 ms to 120 ms. It is therefore very difficult to detect and monitor the cutting heat accurately by current temperature measurement systems. On the other hand, MD simulation provides an alternative way to solve this problem by allowing the atomistic insight into the material thermal behaviour during nanometric cutting processes.

In present work, in order to investigate the thermal effects when different kinds of tools were used, time relaxations of the machined work material were further performed for both the

single tip and multi-tip tool cuttings. It was found through trial simulations that a period of 50 ps relaxation process was enough for the present system to cool down to 293 K. The CSP and the RDF were used to identify the changes in the lattice structure during the relaxation process.

Figure 5-10 shows the cross-sectional views of the defect zones at 0 ps and 50 ps. It can be seen that before the relaxation, there are large number of dislocations and atomic defects beneath the tool tip (figures 5-10 (a) and (c)). The thickness of the atomic defect layer formed in the multi-tip tool cutting is about ~ 6 nm which is nearly twice the thickness created by the single tip tool cutting (being ~ 3.5 nm). However, as shown in figure 5-10 (b), most of atomic defects and dislocations in the machined area were annealed after 50 ps for the single tip tool cutting. For multi-tip tool cutting, the atomic defects and dislocations were also remarkably annealed after the relaxation process (as shown in figure 5-10 (d)), leaving behind an almost dislocation-free machined workpiece.

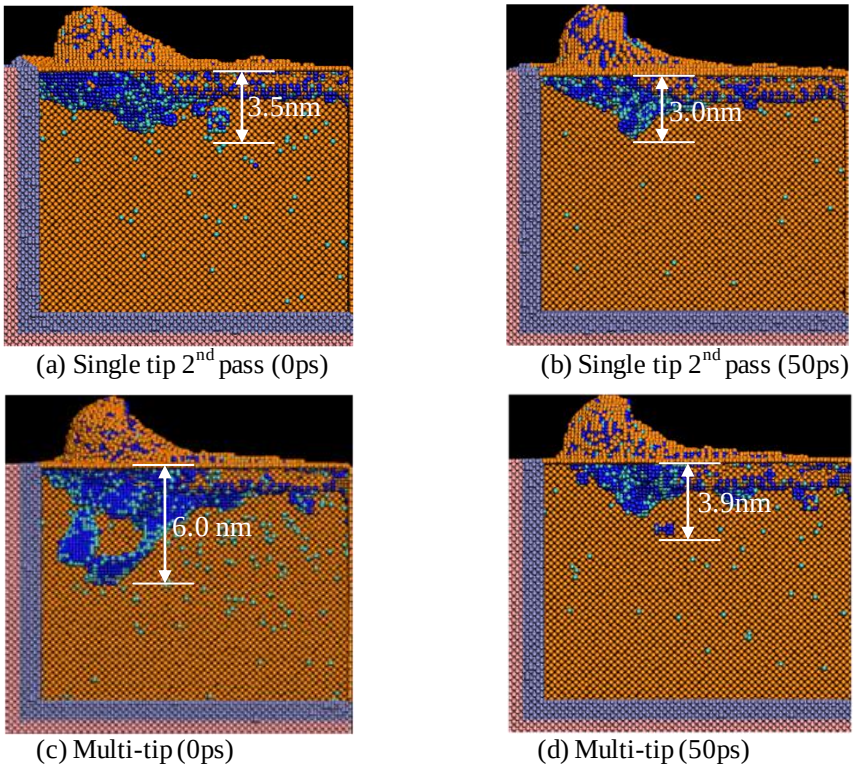

(a) Single tip 2nd pass (0ps)

(b) Single tip 2nd pass (50ps)

(c) Multi-tip (0ps)

(d) Multi-tip (50ps)

Figure 5-10: The cross-sectional views of the defect zones after 0 ps and 50 ps relaxation

process. Cyan and blue atoms represent particle dislocation and stacking fault, respectively [202].

In order to further identify the lattice integrity of the machined structure, the RDFs of the machined nano-grooves were calculated. Compared with the single tip cutting, before relaxation a slightly smaller RDF peak value was found for the nano-grooves machined by the multi-tip tool (figure 5-11 (a)), which indicates that the atoms are in a higher short range disorder in the multi-tip tool cutting. However, after the relaxation process, there is an increase of the first peak value of RDF for both the single tip and the multi-tip tool cutting, and the two RDF curves have nearly the same shape (as shown in figure 5-11 (b)). This result is in good agreement with the CSP result as discussed above and indicates that local re-crystallization takes place on the machined surface during the relaxation process.

Nevertheless, it is noted that the local re-crystallization observed in the multi-tip tool cutting is more noticeable than the single tip tool cutting. Although the thickness of the atomic defect layer before relaxation when using the multi-tip tool was much larger than that of using the single tip tool, most of the defects were annealed and left almost an ideal FCC lattice structure after the relaxation process. As evident from figures 5-10 (b) and (d), the thickness of the residual atomic defect layers are 3.0 nm and 3.9 nm for the single tip and the multi-tip tool cuttings, respectively. Because the dislocation movement is more easily activated at a high temperature, the high local temperature produced during the nanometric cutting process can provide the thermal energy for the defects to get partly annealed.

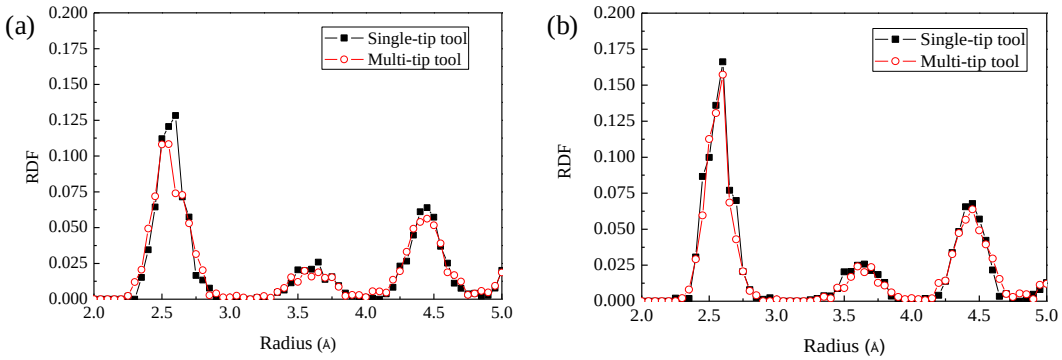

Figure 5-11: RDF of machined nano-grooves. (a) Before the relaxation; and (b) after 50 ps relaxation [202].

5.4 Summary

This chapter was dedicated to provide a detailed understanding on the nanostructure generation processes when using a single tip and a multi-tip diamond tool. To this purpose, this chapter has provided the important parameters which are required for a successful MD simulation of the nanometric cutting process. The post-processing tools of a MD simulation have also been comprehensively described which included the calculation of the cutting forces, the cutting temperature, and the methods used for tracing the atomic defects.

Two large-scale MD nanometric cutting models have been built to simulate the nanometric cutting process when using a single tip and a multi-tip diamond tool, respectively. Compared with the single tip cutting, the new features of multi-tip tool cutting such as the improved centre line symmetry of machined nanostructures, the high cutting temperature, and the high normal cutting force per tip have been identified. The simulation results indicate that, in addition to the high machining efficiency, the effect of feed rate and the alignment issues on machining accuracy associated with the use of separate single tip tool can be completely eliminated when using nanoscale multi-tip tools. The next chapter will further study the shape transferability of nanoscale multi-tip diamond tools in machining nanostructures with various cross-sectional shapes.

Chapter 6 Shape transferability of nanoscale multi-tip diamond tools in nanometric cutting

6.1 Introduction

In the previous chapter, the advantages and disadvantages of diamond turning using the multi-tip tool have been initially addressed with reference to the single tip tool cutting. Nevertheless, the relationship between the geometry of nanostructures pre-fabricated on the tool tip and the form accuracy of nanostructures replicated on the work substrate remains unclear, which has become a significant barrier to the realization of the deterministic nanomanufacturing capability. As the nanostructures are formed synchronously within a single cutting pass, the interactions of the deformed layers created by each tool tip might influence the material removal process and result in unpredictable machining defects. The characterization of the shape transferability of this technique is needed before standardization and commercialization of the nanocale multi-tip diamond tools.

This chapter therefore reports systematic research on the shape transferability of nanoscale multi-tip tools with different designed tool geometries. A hypothesis of a minimum designed ratio of tip distance to tip base width (L/W_f) of the nanoscale multi-tip tool is proposed based on a theoretical study of the effect of tip distance, tip angle, and the tip configuration on the quality of machined nanostructures. Nanometric cutting experiments using nanoscale multi-tip diamond tools are then conducted to verify the hypothesis. The potential of using nanoscale multi-tip diamond tools for the deterministic scale-up fabrication of period and non-periodic nanostructures are discussed in the subsequent section.

6.2 Tool model and MD simulation parameters

In order to obtain in-depth understanding of the shape transferability of nanoscale multi-tip diamond tools, four categories of diamond tool used to machine periodic and non-periodic

nanostructures were studies in this work. The cross-sectional shapes of the tools and the tip configurations are shown in figures 6-1 (a)-(d) (L is defined as the tip distance; θ is the tip angle; W_a and W_f are used to represent the width of the top and bottom of the tool tip respectively). For the purpose of concision, the four types of multi-tip tools are generally labelled as T1, T2, T3, and T4 in this work. All of the tool models built here are based on a deformable body with a round cutting edge radius r of $5a_1$ (a_1 = 3.567 Å), a tool rake angle α of 0 °, and a tool clearance angle β of 10 °(as shown in figure 6-1 (e)). To save computational time, the tools were built with a double-tip to represent the multi-tip tool. The cutting processes using 24 diamond tools with different combinations of cross-sectional geometrical parameters (listed in Table 6-1) are simulated in this study.

The MD nanometric cutting model using multi-tip single crystal diamond tool is developed as shown in figure 6-1 (f). The copper workpiece has dimensions of $50a_2 \times 80a_2 \times 40a_2$ (a_2 = 3.615 Å). It consists of the boundary layer and the thermostat layer with thicknesses of $2a_2$ and $3a_2$, respectively. The three orientations of the workpiece are [1 0 0], [0 1 0], and [0 0 1] in the X, Y, and Z directions respectively.

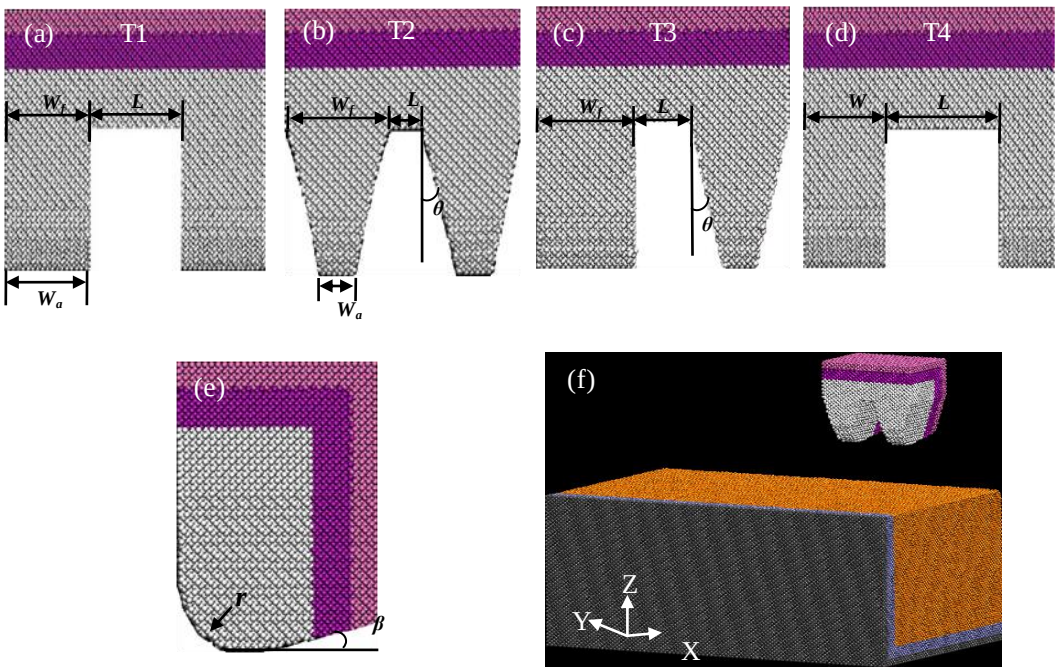

Figure 6-1: MD nanometric cutting models using multi-tip diamond tools. The front view of

multi-tip tool models are (a) periodic tips configuration with rectangular cross-sectional shape (T1), (b) periodic tips configuration with trapezoidal cross-sectional shape (T2), (c) non-periodic tips configuration with a mixture of cross-sectional shapes (T3), and (d) non-periodic tips configuration with a rectangular cross-sectional shape (T4). (e) Right hand end elevation of multi-tip tool models. (f) The nanometric cutting model [35].

Table 6-1: Dimensions of nanoscale multi-tip diamond tool models [35].

	Tip distance (L)	Tip angle (θ)	Tip base width (W_f)
T1	$3a_1, 6a_1, 9a_1, 12a_1, 14a_1$	0 °	$9a_1$
T2	$3a_1, 6a_1, 9a_1, 12a_1, 14a_1$	14.0 °	$9a_1$
	$6a_1$	16.3 °, 14.0 °, 11.8 °, 9.46 °, 7.13 °	$9a_1$
T3	$3a_1, 5a_1, 7a_1, 9a_1, 12a_1$	0 °(left tip); 14.0 °(right tip)	$9a_1$
T4	$4a_1, 6a_1, 7a_1, 9a_1, 12a_1$	0 °	$9a_1$ (left tip); $6a_1$ (right tip)

The potential scheme described in section 5.2.2 of Chapter 5 is used in this study. The EAM potential, the Tersoff potential, and the Morse potential function are employed to describe the interactions between Cu-Cu atoms, C-C atoms, Cu-C atoms, respectively.

Due to the limitation of computational power, a high cutting speed was adopted as other researchers to speed up the MD simulation. In this study all of the cutting tools were applied along the minus X direction at a constant speed of 200 m/s with a depth of cut of 2.5 nm. Two nano-grooves were formed synchronously by a single cutting pass. MD simulations were implemented by using an open source code, LAMMPS, compiled on a high performance computing (HPC) workstation using 32 cores. Before cutting, 85,000 computing time steps were carried out to freely relax the system to 293 K. During cutting processes, the systems were controlled by NVE ensemble and the thermostat atoms were kept at a constant temperature of 293 K through using the velocity scaling method [101] to perform the heat dissipation. After the cutting, all of the models were allowed to relax for 50,000 time steps (50 ps) by holding the tool in the fixed loaded position in order to obtain

the accurate form of nanostructures after elastic/plastic recovery of materials. The visualization of atomistic configurations was realized by VMD software.

6.3 Formation of periodic and nonperiodic nanostructures

Figure 6-2 shows the nano-grooves fabricated by using the four types of nanoscale multi-tip diamond tools with the designed tip distance L being $12a$ ($L/W_f = 1.33$). The atoms with cyan and blue colour represent the particle dislocations and stacking faults, respectively. As is evident from figure 6-2 (the left and middle columns), nano-grooves with different cross-sectional shapes were formed synchronously within a single cutting pass through material plastic deformation dominated by the dislocation nucleation and the extension of the stacking faults. The quality of the machined nanostructures was characterized by both the form accuracy of the machined nanostructures achieved in depth direction and the thickness of the deformed layers. The shape transferability was assessing by quality of machined nanostructures. It is found that the thicknesses of the deformed layer are 4.8 nm and 4.5 nm for type T1 and T2 tools, respectively. However, slightly larger values of 5.0 nm and 5.3 nm were found when type T3 and T4 tools were applied. The results suggest that tools of periodic tip configuration might have better shaping performance than tools with non-periodic tip configuration.

Moreover, the pictures located at the right column of figure 6-2 show the cross-sectional views of the machined nano-grooves after a full relaxation process. The form error was calculated as a deviation of depth of the machined nano-groove from the designed depth. It is found that the form errors of using different types of multi-tip tools are all less than 7.3%, which demonstrates the high machining capacity of using this technique for the fabrication of periodic and non-periodic nanostructures. Further, material elastic recovery was observed when the trapezoidal tips were used (figures 6-2 (b) and (c)). These results signify that employing a tool tip angle would create a heterogeneous distribution of the compressive stress at the side walls of the machined nano-grooves. The effect of tool tip angle on the

integrity of the machined nanostructures will be further discussed in the following section.

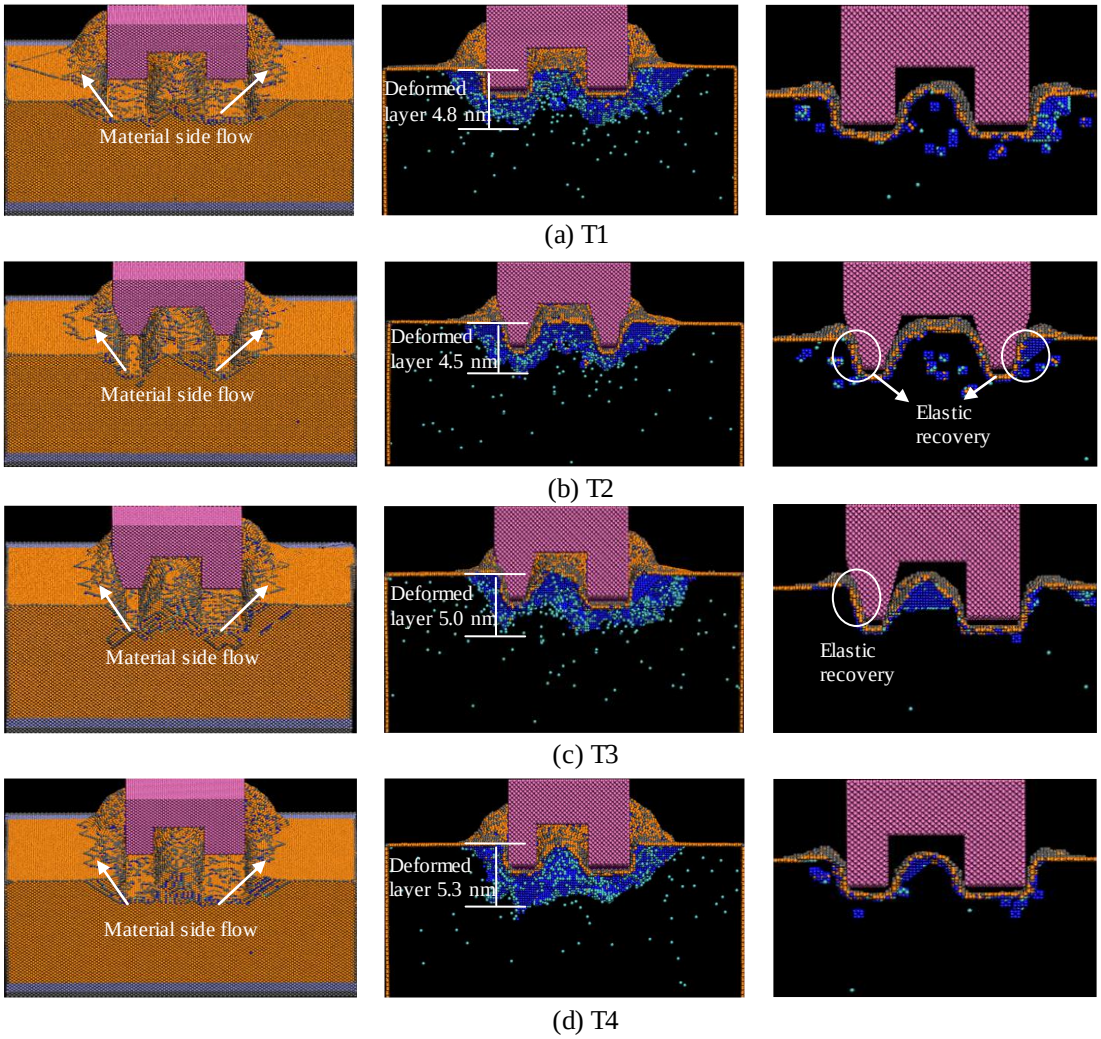

Figure 6-2: Photographs of the nanostructures generated (left), the cross-sectional views of the deformed layer (middle), and the cross-sectional views of the shape of the machined nano-grooves after relaxation (right) when using four types of nanoscale multi-tip diamond tools, labelled as: (a) T1, (b) T2, (c) T3, and (d) T4. Tip distance $L = 12a_1$, depth of cut = 2.5 nm, cutting speed 200 = m/s. Cyan and blue atoms represent particle dislocation and stacking fault, respectively [35].

Additionally, the averaged cutting forces at a steady cutting state are summarized in figure 6-3. It was found that both the tangential cutting force F_x and normal cutting force F_z when using rectangular cross-sectional shape tools (T1 and T4) were larger than when using

trapezoidal cross-sectional shape tool (T2). The value of F_x when using the multi-tip tool with the mixture of tool tip shapes (T3) was 68.2 nN, which was slightly larger than the mean value of the tangential cutting forces (being 65.6 nN) when the T1 and T2 type tools were used . Moreover, the ratios of F_x/F_z were around 1.42 when the T1 and T4 type tools were used. The large ratio of F_x/F_z was attributed to the large depth of cut used with respect to the cutting edge radius. Similar phenomenon has also been observed in [210]. However, the ratios of F_x/F_z reduced to about 1.0 when T2 and T3 type tools were used. The results indicate that trapezoidal tips can minimize the tangential cutting forces and thus reduce the ratio of F_x/F_z. The apparently smaller cutting forces when using the T2 type tool suggest that the periodic trapezoidal cross-sectional shape multi-tip tool offers the best shape transferability among the tools studied in the this work.

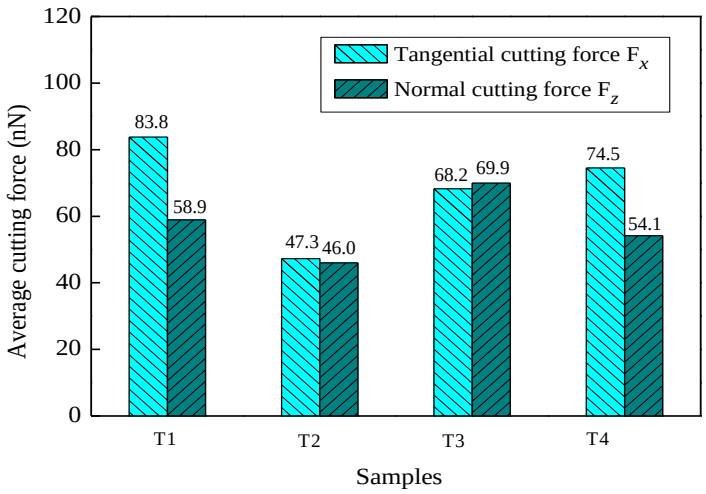

Figure 6-3: The averaged cutting forces when using different types of cutting tools [35].

6.4 Dependence of the shape transferability on the tool

6.4.1 Effects of tool tip distance

The cross-sectional shape of the tool tip and the tip distance are two major geometrical parameters when designing the nanoscale multi-tip cutting tool. In order to quantify the effect of tool geometry on the shape transferability, a series of MD nanometric cutting

simulations were carried out while varying the tip distance of diamond tools (as summarized in Table 6-1).

Figure 6-4 shows the photographs of cross-sectional views of nano-grooves generated by multi-tip diamond tools with different tool tip distances (type T1 tools). It is found that the quality of the machined nano-grooves improves with the increase of the ratio of L/W_f. As shown in figures 6-4 (a) and (d), a large form error was found when L is $6a$ ($L/W_f = 0.67$). Similar results were observed when L equals $3a$ (not shown in the thesis for the purpose of concision). However, the nano-grooves can be well formed when the tip distance is equal to or greater than $9a_1$ ($L/W_f \geqslant 1$). Moreover, as shown in figures 6-4 (e)-(f), the thickness of the deformed layer was found to be decreased with the increase of tool tip distance. The results preliminarily suggest that, for the nanoscale multi-tip tool cutting, there exists a limit of the ratio of L/W_f which can be used to achieve high form accuracy in a single cutting pass.

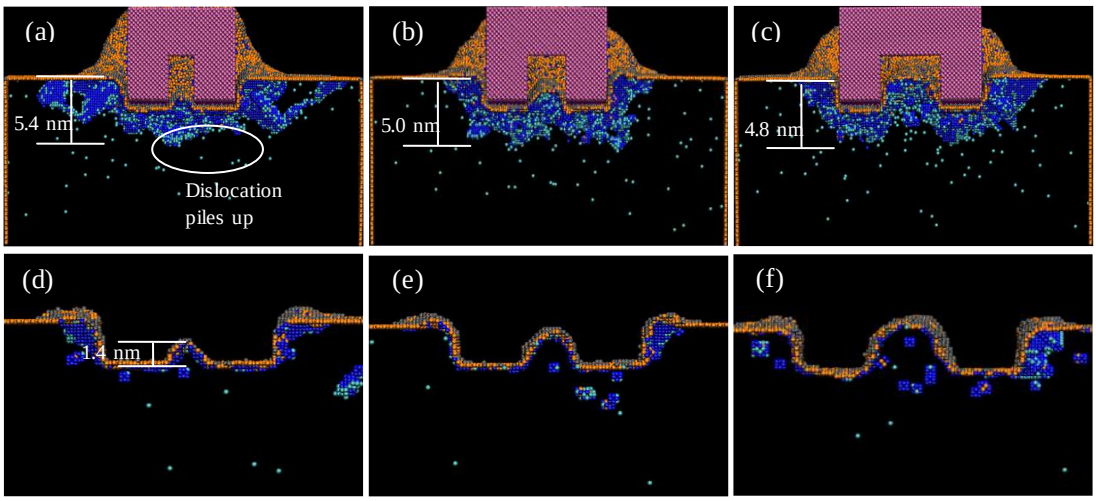

Figure 6-4: Photographs of cross-sectional views of deformed layers when using multi-tip tools with different tip distances: (a) $L = 6a_1$, (b) $L = 9a_1$, (c) $L = 12a_1$; and the corresponding views of machined nano-grooves ((d)-(f)). Cyan and blue atoms represent particle dislocation and stacking fault, respectively [35].

6.4.2 Effects of tool tip angle

The cross-sectional views of nano-grooves generated by tools with different tip angles (tool type T2) are shown in figure 6-5. In order to quantify the effect of the tip angle, the tools were built with the same ratio of L/W_f (0.67). Similarly to the rectangular cross-sectional shape tool cutting, large form errors were found when a tip angle of 7.13° was used. However, as is evident from figures 6-5 (e) and (f), the nano-grooves can be accurately formed when the tip angle is equal to or greater than 11.8°. The deformed layers were found to be decreased with the increase of the tip angle. Thus, applying a multi-tip diamond tool with the proper tool tip angles, the shape transferability can be improved significantly.

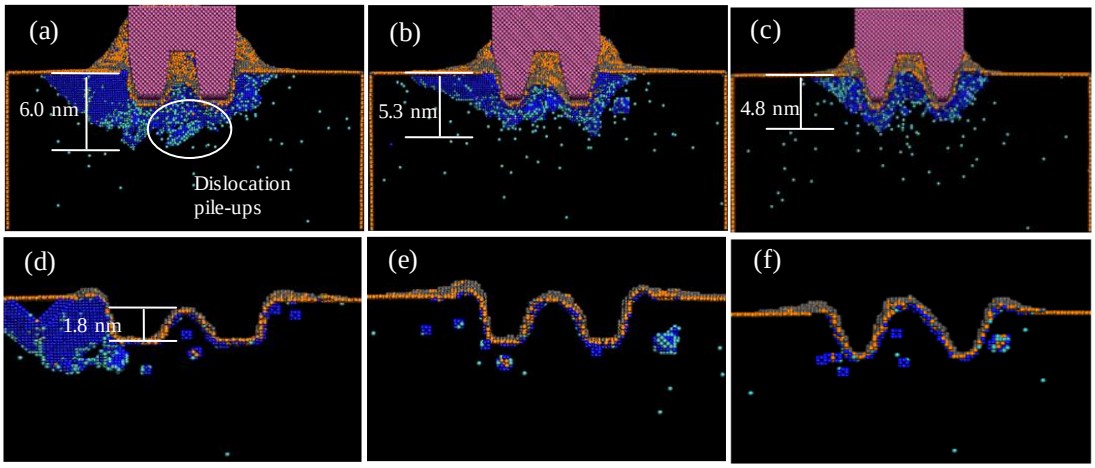

Figure 6-5: Photographs of deformed layer during nanometric cutting process when using multi-tip tools with different tip angles: (a) 7.13°, (b) 11.8°, and (c) 16.3°, and the corresponding views of machined nano-grooves ((d)-(f)). The ratios of L/W_f of the tools are 0.67. Cyan and blue atoms represent particle dislocation and stacking fault, respectively [35].

6.4.3 The critical ratio of L/W_f for different tool geometries

Moreover, the variation of the form errors of the machined nano-grooves against the ratio of L/W_f for the four types of multi-tip tools is summarized in figure 6-6. It was found that the form errors all decreased with the ratio of L/W_f. A critical form error of 10 % can be defined as the upper limit of the deviation of the machined nano-grooves (as indicated by the dashed

line in figure 6-6), and the corresponding critical ratios of L/W_f are 0.93, 0.53, 0.76, and 0.97 for T1, T2, T3, and T4 type tools respectively. The results indicate that the multi-tip tools with trapezoidal tips (T2) have better shape transferability than rectangular cross-sectional shape tools (T1 and T4); and multi-tip tools with periodic tip configuration (T1 and T2) have better shape transferability than those with non-periodic tip configuration (T3 and T4). The shape transferability for tools with mixed shape tips (T3) depends significantly on the geometry of the two adjacent tool tips. The critical ratio of L/W_f lies between the L/W_f ratio of the two adjacent tips calculated from the periodic tip configurations (T1 and T2).

The reasons accounting for the difference are as follows. Since the nano-grooves are formed synchronously in the nanoscale multi-tip tool cutting, the overlap of the deformed layers created by cutting tips should be well controlled. When the tool cuts into the workpiece, each tip will create a deformed layer in its immediate vicinity (also named as work-affected layer). The range of the plastically deformed region is two to ten times the indention radius [218]. Because the trapezoidal cross-sectional shape tip has a smaller contact radius in the YOZ plane as compared to the rectangular cross-sectional shape tip, a smaller region of work-affected area is formed [218, 219]. Thus the overlap of the deformed layer can be effectively minimized when using tools with trapezoidal cross-sectional shape tips. Moreover, the material side flow made a significant contribution to the formation of the nanostructures [211, 219]. As the tool with periodic tip configuration has better central symmetry properties than the tool with non-periodic tips configuration, a uniform material side flow is easily achieved and therefore a smaller critical ratio of L/W_f is required. Additionally, under the same cutting conditions, smaller cutting forces were observed when using trapezoidal cross-sectional shape tips with periodic tips configuration (as discussed in section 6.4.1). Thus, it is concluded that the tool geometry of nanoscale multi-tip diamond tools has significant influence on the quality of machined nanostructures. The tool tip angle can effectively control the material side flow and minimize the interactions of deformed layers beneath the tool tips during the machining process. A minimum ratio of L/W_f should be met

for the high precision machining of nanostructures, based on the MD simulation results as discussed above. The next section will further verify this hypothesis through nanometric cutting trials using nanoscale multi-tip diamond tools.

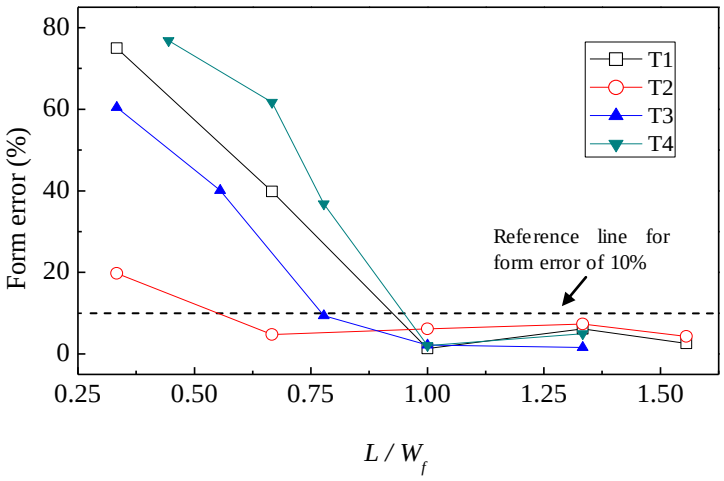

Figure 6-6: The variation of the form error of machined nano-grooves with the ratio of L/W_f for the four types of multi-tip diamond tools [35].

6.5 Inital experimental verification

6.5.1 Tool fabrication

In order to verify the simulation results, two nanoscale multi-tip diamond tools (with different L/W_f) were fabricated by FIB (FEI Quanta3D FEG) using the divergence compensation method proposed by [53]. The FIB machining procedure for nanoscale multi-tip tools is schematically shown in figure 6-7. An ion beam current of 50 pA was applied in rough shaping process. After the rough shaping, a low ion beam current of 10 pA was used to finely trim the profile of the structures as an ion beam cleaning process (beam diameter of 13 nm).

Since the MD simulation results show that the periodic trapezoidal cross-sectional shape offers the best shape transferability, two nanoscale multi-tip diamond tools with such configuration were used in the cutting trials. As shown in figures 6-8 (a) and (b), one is a

four-tip tool with a ratio of tip distance to tip base width (L/W_f) of 1.54, and another one is a seventeen-tip tool with L/W_f of 0.33. They both have trapezoidal cross-sectional shape (tip angle θ of 14.0°) which is the same shape as the corresponding tool tip used in the MD simulations. The ratio of the tool tip distance to the tip base width (L/W_f) is employed as an indicator when comparing the MD simulation and experimental results qualitatively.

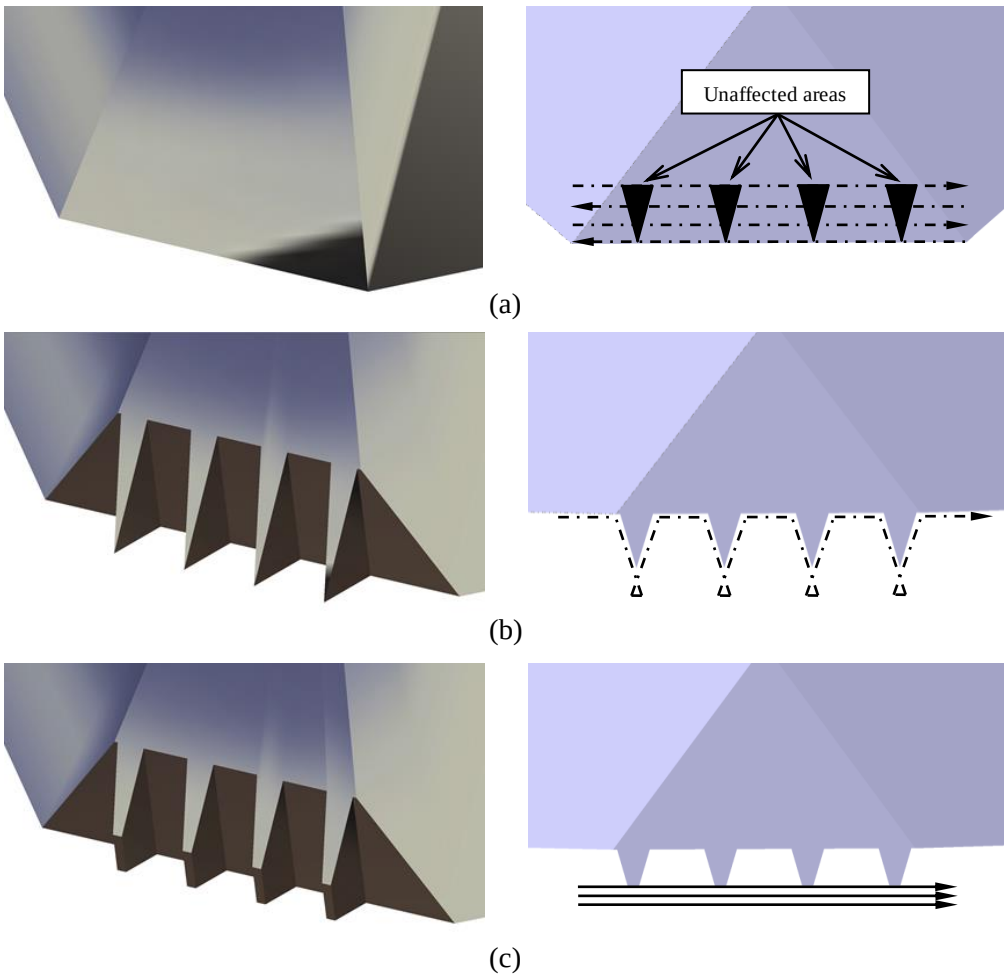

Figure 6-7: The FIB machining procedure for nanoscale multi-tip diamond tools with periodical chisel structures: (a) fabrication of trapezoidal structures on the diamond tip; (b) the ion beam cleaning process; and (c) cutting off the vertexes of the triangular tips [53].

6.5.2 Experimental set up

The nanometric cutting trials on an oxygen free copper (OFC) surface using the nanoscale

multi-tip diamond tools were carried out on a diamond turning machine (Precitech Nanoform 250). In all tests, the same cutting conditions were applied (cutting speed = 0.03 m/s, depth of cut = 100 nm). The nanometric machining process and the fabricated samples are illustrated in figures 6-8 (c) and (d). The machined nanostructure patterns were measured by a SEM integrated in FEI Quanta3D FEG instrument.

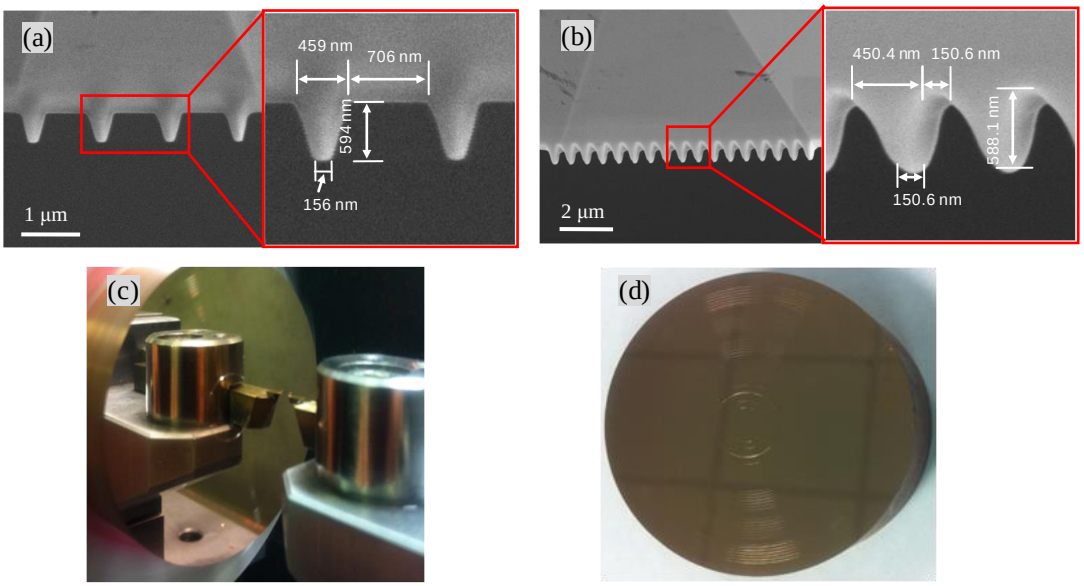

Figure 6-8: Diamond turning using nanoscale multi-tip diamond tools: (a) SEM image of multi-tip tool with L/W_f of 1.54; (b) SEM image of multi-tip tool with L/W_f of 0.33; (c) nanometric cutting operation; (d) the machined surfaces with nanostructures.

6.5.3 Experimental results and discussion

Two sets of experiments were carried out to evaluate the hypothesis proposed based on the MD simulations. In the first experiment, a series of four parallel nano-grooves were successfully formed by the multi-tip tool with L/W_f ratio of 1.54 (as shown in figure 6-9 (a)). The form accuracy of the machined nano-grooves is preliminarily characterized as the deviation of the measured width of nano-grooves (averaged width is 203 nm) to the width of the multi-tip tool (the tip width is 207 nm at the tip height of 100 nm). The divergence value of 4 nm is mainly due to the elastic recovery of the work material after the tool tip is released

from the machined surface. The small form error demonstrates the high machining capacity of using the nanoscale multi-tip tool to cut well-defined trapezoidal nano-grooves on a copper surface. The same cutting operation was then applied for the second multi-tip tool cutting (L/W_f = 0.33). As is evident from figure 6-9 (b), nano-grooves were fabricated with serious machining defects in terms of side burrs and structural damage. Thus, the experimental results qualitatively confirm the hypothesis predicated by MD simulations.

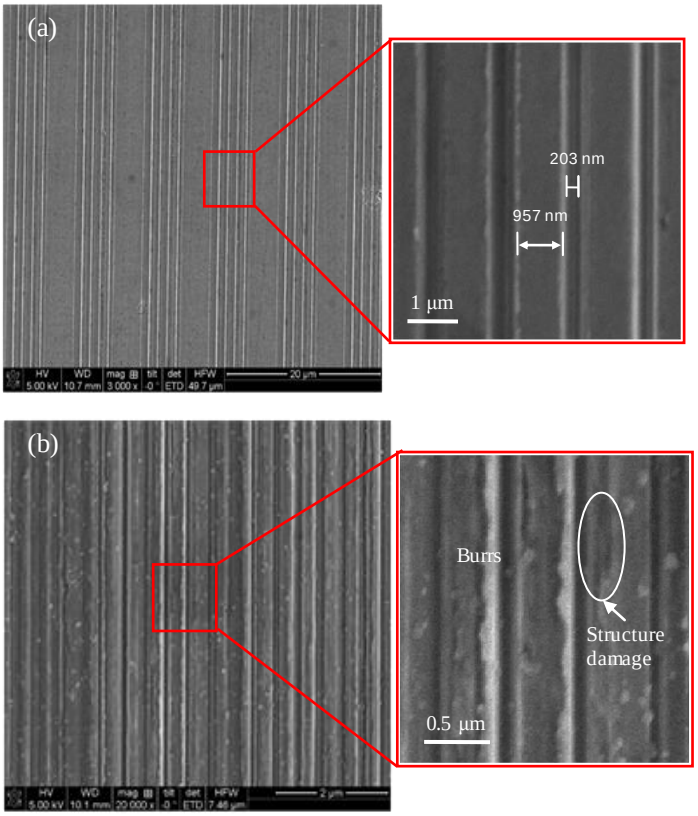

Figure 6-9: SEM images of the nanostructures fabricated by nanoscale multi-tip diamond tools with different ratio of tip distance to tip base width (L/W_f): (a) L/W_f 1.54; (b) L/W_f 0.33. (Cutting speed = 0.03 m/s, depth of cut = 100 nm) [35].

Nevertheless, it is noted that the critical value of the ratio of tool tip distance to tool tip width (L/W_f) needs be clarified through more quantitative experiment and theoretical analysis in the future. Currently, it is still quite difficult to compare MD simulation and experimental results in the same spatial and time scale. The difficulties in answering this fundamental question

from experimental side have been the limitation of using FIB to fabricate multi-tip diamond tool in several nanometres, and the time resolution that is needed for a detection equipment to capture the transient process of defects formation which evolve on time scales of some nanoseconds. On the MD simulation side the difficulties lie in developing a super high performance computing system for solving a highly inhomogeneous many body problem in the same spatial and time scales as experiments, as well as an effective visualization technique for analysing the MD simulation results.

In order to overcome these limitations, in this study the ratio of tool tip distance to tool tip width (L/W_f) was employed as an indicator when qualitatively comparing the results between the MD simulation and the experiments focusing on the dimensional accuracy of machined nanostructures. As the plastic deformation zone below the cutting tool tip also increases with the increase of the size of the tool tip, this assumption is reasonable at current spatial scale. Moreover, Komanduri *et al*. [94] commented that the effect of high cutting speed used in MD simulations can be minimized when analysing the general nature of the process. In the present study, the phenomenon of formation of nanostructures observed in the MD simulation is in good agreement with the initial experimental test.

Theoretically, based on Hill's elastic—plastic theory Taniguchi has proposed a method of using c/*a*, the ratio between the radii of the plastically deformed zone and the indentation, to determine the extent of plastically deformed zones as schematically shown in figure 6-10. The value of c/*a* is calculated as follows [218]:

$$\left(\frac{c}{a}\right)^3 = \frac{E_c}{3(1-\upsilon)Y} \tag{6-1}$$

where E_c is the modulus of elasticity, Y is the yield stress, and υ is the Poisson's ratio. For a ductile metal material such as copper, the measured c/*a* ratio is around 8.0 [218] which theoretically predicts that the deformed layer during the nanometric cutting of copper would have a thickness of up to eight times the contact radius of the tool tip. For single tip tool

cutting, it is reported that the deformed layer of the subsequent cutting pass will reshape the former machined nanostructures if the distance between the two cutting passes is smaller than a critical value [99, 101]. For multi-tip tool cutting, the feed rate issue can be avoided because the nanostructures are formed synchronously by the multi-tip tool with a single cutting pass [211]. However, this advantage only works when the ratio L/W_f of the multi-tip tool is larger than a critical value. Below this value, the overlap of the deformed layers created by each tool tip might affect the material plastic flow and degrade the form accuracy of the machined nanostructures. Because a tool with trapezoidal cross-sectional shape tips would create a smaller region of the deformed layer than a tool with rectangular tips, a smaller tip distance can be used in the tool design process. The overlap of the deformed layers has been vividly evidenced by the MD simulation results, showing the dislocation pile-ups beneath the tool tips (as shown in figures 6-4 and 6-5).

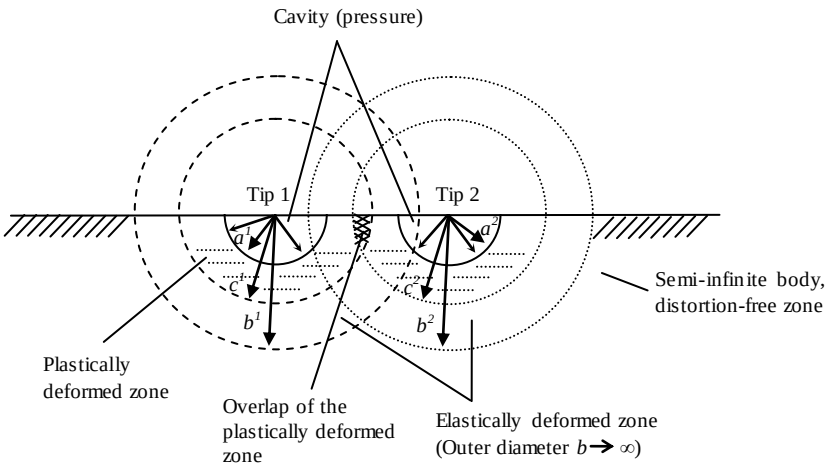

Figure 6-10: Schematic illustration of the overlap of the deformed zone during a multi-tip tool cutting process based on Hill's shell expansion theory.

In general, any complex tool face geometry is possible. As the tools and the machined structures are in a range of sub-micrometres or dozens of nanometres, even tiny machining defects caused by the improper design of the tool geometry might seriously degrade the form accuracy of machined nanostructures. Nevertheless, as evidenced by both the experimental

results and the simulation data presented here, when the value of L/W_f of the tool is sufficiently large, the side effect of the overlap of deformed layers can be minimized or even totally overcome. This result indicates the great potential for improving the form accuracy of nanostructures by minimizing the overlap of work-affected layers through an optimal design of the geometry of nanoscale multi-tip diamond tools.

6.6 Summary

This chapter has explored the potential of using nanoscale multi-tip diamond tools for the deterministic fabrication of periodic and non-periodic nanostructures with different cross-sectional shapes. In order to identify the effect of tool geometrical parameters on the shape transferability of the nanoscale multi-tip tool, four categories of multi-tip diamond tools have been designed. The nanometric cutting processes of using these tools have been modelled and simulated by large-scale MD simulations method.

Based on the theoretical study of the effect of the tip distance, the tip angle, and the tip configuration on the quality of machined nanostructures, a hypothesis of a minimum designed ratio of tip distance to tip base width (L/W_f) of the nanoscale multi-tip tool has been proposed. The hypothesis has been qualitatively validated by nanometric cutting experiments. The MD nanometric cutting model developed in this chapter and a new nanoscale multi-tip diamond tool fabricated with L/W_f of 1.54 were used in Chapter 7 to study the influence of processing parameters and tool wear in diamond turning using nanoscale multi-tip tools.

Chapter 7 Influence of processing parameters and tool wear during a nanoscale multi-tip tool cutting

7.1 Introduction

In diamond turning using nanoscale multi-tip diamond tools, as the tools and the machined structures are in a range of sub-micron or even dozens of nanometres, even tiny (nanometre level) machining defects can degrade the form accuracy and the integrity of machined nanostructures. In-depth understanding of the machining process, especially knowing the nanomanufacturing capability under different cutting conditions is of great significance to full exploration of the advancement of this technique.

In Chapter 6, we demonstrate that the tools having trapezoidal cross-sectional shape had the best shape transferability among other tool designs. In this chapter, the focus will be on the influence of processing parameters on the accuracy and the integrity of machined nanostructures as well as the tool wear. A series of nanometric cutting trials (under 15 different cutting conditions) on copper substrates are carried out using the nanoscale multi-tip diamond tool fabricated with L/W_f of 1.54. In order to reveal the underlying mechanism for machining defects and the initialization of tool wear observed in experiments, MD simulations are carried out to gain atomistic insight into the work material behaviour during the nanometric cutting process.

7.2 Experiment setup

7.2.1 Facilities for diamond turning experiments

The nanometric face cutting trials using a nanoscale multi-tip diamond tool were carried out on a diamond turning machine (Precitech Nanoform 250). The configuration of the cutting trials is shown in figure 7-1. The cutting tools were mounted on a tool holder. An optical tool setter with a 20x long working distance objective lens was used to set the tools.

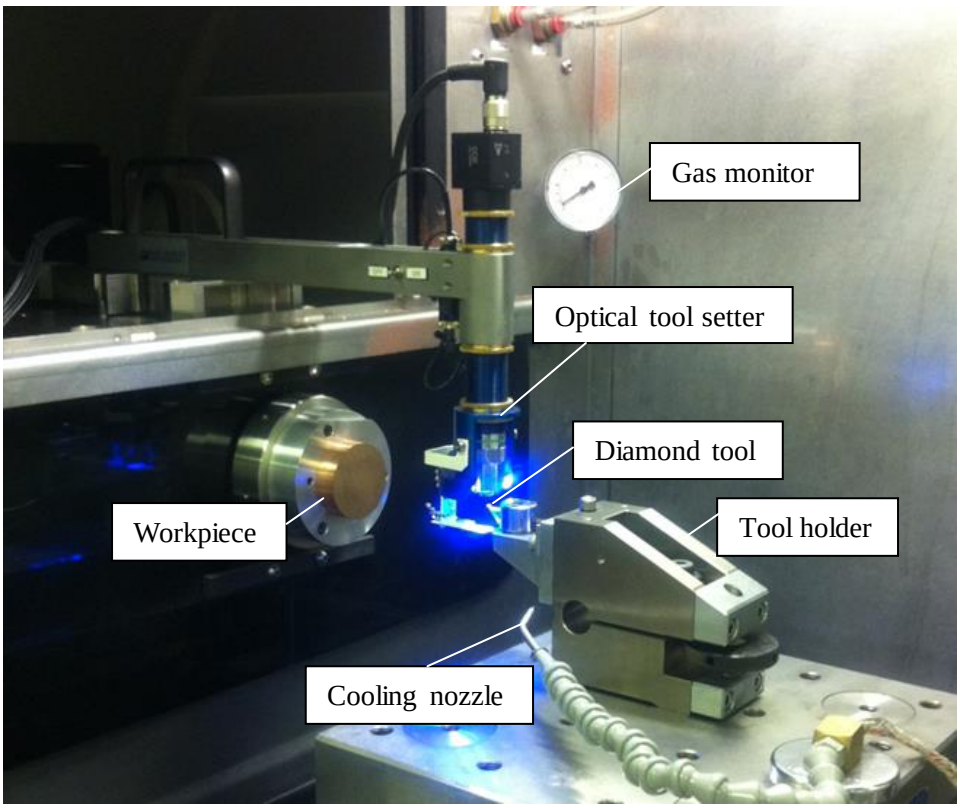

Figure 7-1: Experimental configuration and tooling set up.

7.2.2 Workpiece material for diamond turning trials

Nanometric machining was conducted on an oxygen free copper (OFC) wafer. It had a diameter of 50 mm and the following properties: hardness 89HV50, density 8.94 g/cm^3, shear modules 44.0 GPa, Poisson's ratio 0.31, annealing temperature 375-650 ℃.

7.2.3 Cutting tools

Three diamond cutting tools were used in the experiment. Before the multi-tip diamond tool cutting, a flat copper substrate surface was prepared by face diamond turning using two normal diamond tools. One conventional roughing tool was used for rough cutting of the copper surface. After the rough cutting, a controlled waviness diamond tool was used to generate the surface with mirror finish. The cutting fluid (CLAIRSOL 330 special kerosine) was applied in these steps. Then, the multi-tip diamond tool was used to generate

nano-grooves on the flat copper surface. The multi-tip tool had a tip height of 589.8 nm, a tip width of 152.9 nm and a tip base width of 458.5nm with the tip distance being 706 nm. The geometrical features of the cutting tools are listed in Table 7-1.

Table 7-1: Geometric features of the cutting tools used in the cutting trials

	Tool nose radius (mm)	Rake angle (°)	Clearance angle (°)	Cutting edge radius
Roughing tool	0.5 mm	0°	10°	Standard
Controlled waviness tool	0.5 mm	0°	10°	Standard
Nanoscale Multi-tip tool	—	0°	10°	40 nm

7.2.4 Plan for nanometric cutting

Three spindle speeds tested were 12 rpm (low), 60 rpm (medium), and 120 rpm (high). For each spindle speed, the value of depth of cut was set at five different levels, from 100 nm to 500 nm with an increment of 100 nm. The parameters are list in Table 7-2.

Table 7-2: Operational variables and their levels in face turning trials.

Face cutting	**No. of cut**	**Depth of cut (nm)**	**Spindle speed (rpm)**	**Radius of start point (mm)**	**Cutting speed (m/s)**	**Feed rate (μm/re)**
Group A	1st	100	12	23.0	0.02890	9
	2nd	200	12	22.5	0.02827	9
	3rd	300	12	22.0	0.02765	9
	4th	400	12	21.5	0.02702	9
	5th	500	12	21.0	0.02639	9
Group B	6th	100	60	19.0	0.11938	9
	7th	200	60	18.5	0.11624	9
	8th	300	60	18.0	0.11310	9
	9th	400	60	17.5	0.10996	9
	10th	500	60	17.0	0.10681	9
Group C	11th	100	120	15.0	0.18850	9
	12th	200	120	14.5	0.18221	9

Group C	13th	300	120	14.0	0.17593	9
	14th	400	120	13.5	0.16965	9
	15th	500	120	13.0	0.16336	9

The procedure of the diamond turning using the nanoscale multi-tip diamond tool and the fabricated samples are illustrated in figure 7-2. After the machining trials, the machined surface roughness and the nanostructure pattern were measured by using a white light interferomter (Form TalySurf CCI 3000) and a Scanning Electron Microscope (FEI Quanta3D FEG), respectively.

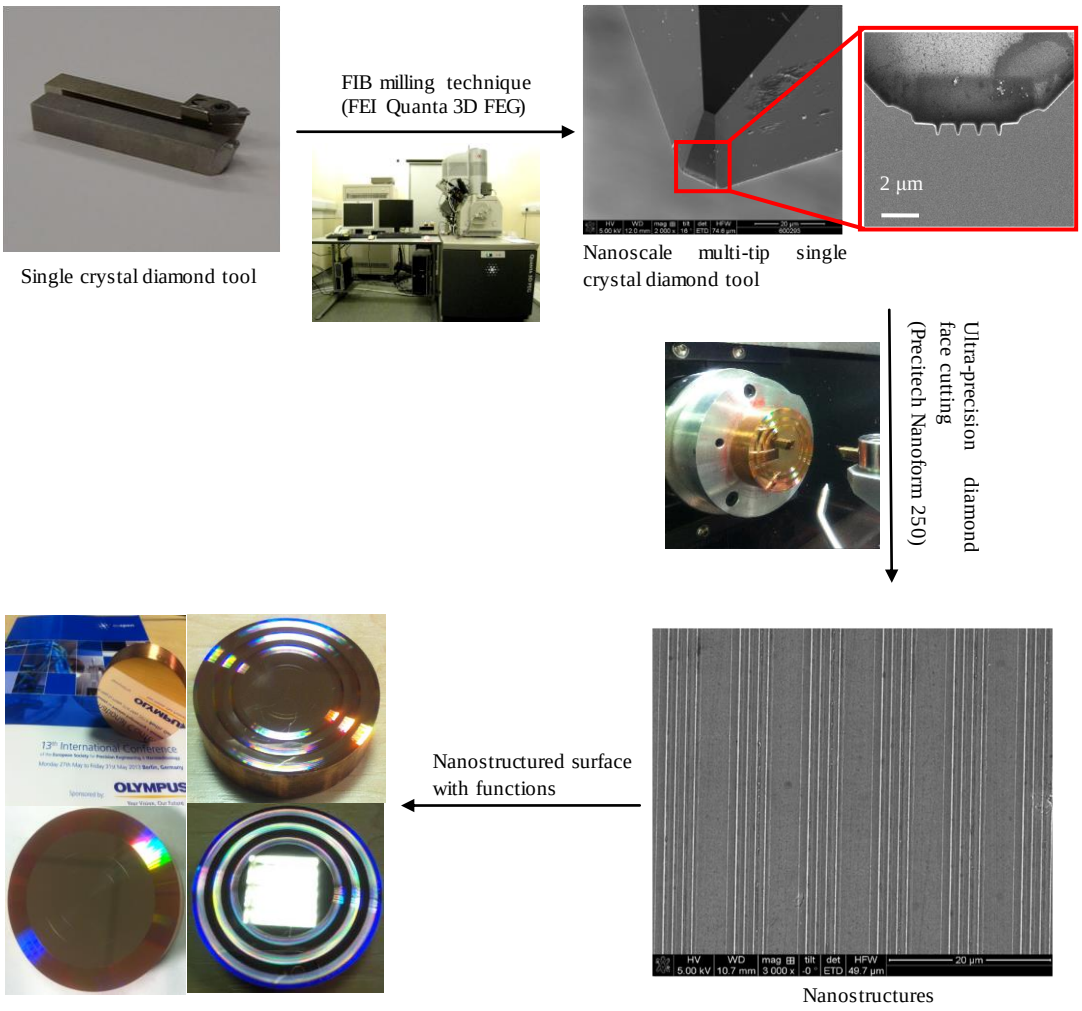

Figure 7-2: Procedure of diamond turning using nanoscale multi-tip diamond tools.

7.3 MD simulation setup

The MD nanometric cutting model was developed as shown in figure 7-3. The geometrical parameters of the tool were built according to the shape of the multi-tip tool tips fabricated by FIB. The tool had a tip width W_a of $3a_1$ (a_1 = 3.567 Å), a tip base width W_f of $9a_1$, a tool rake angle α of 0°, a tool clearance angle β of 10°, a tip angle θ of 14°, and a cutting edge radius r of $5a_1$. To save the computational time, a double-tip nanoscale diamond tool with the tool tip distance L of $14a_1$ was employed in present work to represent the nanoscale multi-tip diamond tool (as shown in figure 7-3 (a)). The systems were controlled by NVE ensemble and the thermostat atoms were kept at a constant temperature of 293 K through a velocity scaling method to perform the heat dissipation [101]. The other computational parameters used in the MD simulations are summarized in Table 7-3 for reference.

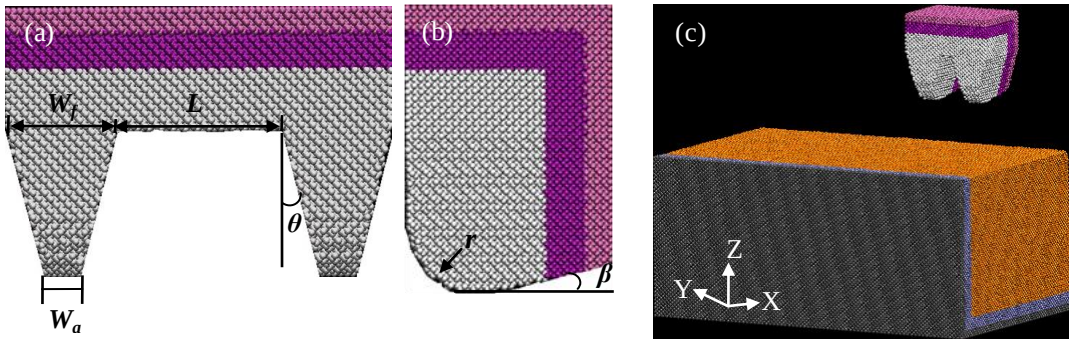

Figure 7-3: Molecular dynamics simulation model. (a) Front view of the multi-tip tool model; (b) right hand end elevation of the multi-tip tool model; and (c) nanometric cutting model.

Table 7-3: Simulation parameters of MD nanometric cutting model.

Workpiece materials	Copper
Workpiece dimensions	$50a_2 \times 80a_2 \times 40a_2$ (a_2 = 3.615 Å)
number of atoms	714,707
Time step	1 fs

Initial temperature	293 K
Depth of cut (cutting speed = 200 m/s)	2.0 nm, 2.5 nm, 3.0 nm, 3.5 nm, 4.0 nm
Cutting speed (depth of cut = 2.0 nm)	10 m/s, 50 m/s, 100 m/s, 160 m/s, 200 m/s, 250 m/s

7.4 Results and discussions

7.4.1 Nanostructures formed under different cutting conditions

As shown in figure 7-4 (a), the surface roughness S_a of the copper substrate was 1.85 nm prepared by the face diamond turning. The surface was then machined by the nanoscale multi-tip diamond tool with a depth of cut of 100 nm (a cutting speed of 0.03 m/s, a feed rate of 9 μm/rev).

The SEM images of several machined grooves using different depths of cut are shown in figure 7-5. In general, the periodic nanostructures on the diamond tool tip were successfully replicated on the surface of the copper substrate when the depths of cut of 100 nm and 200 nm were used. As shown in figure 7-5 (a), the measured bottom widths of the nano-grooves generated under the depth of cut 100 nm ranged from 142.3 nm to 150.2 nm, which are slightly less than the tool tip width of 152.9 nm. The deviation is mainly due to the elastic recovery of the work material after the tool tip released from the surface. Moreover, the surface roughness S_a of the region between each cutting pass was found to be slightly increased to 2.50 nm (as shown in figure 7-4 (b)), which is mainly caused by the material squeezed from the adjacent cutting passes.

However, the form accuracy and integrity of the machined nano-grooves were found to be degraded with the increase of depth of cut. Lots of side burrs were observed when the depth of cut was equal or larger than 300 nm (figure 7-5 (c)). Structure damage was found when a depth of cut of 400 nm was used (figure 7-5 (d)). The results indicate that there exists an upper limit of depth of cut when machining nano-grooves using nanoscale multi-tip diamond tools.

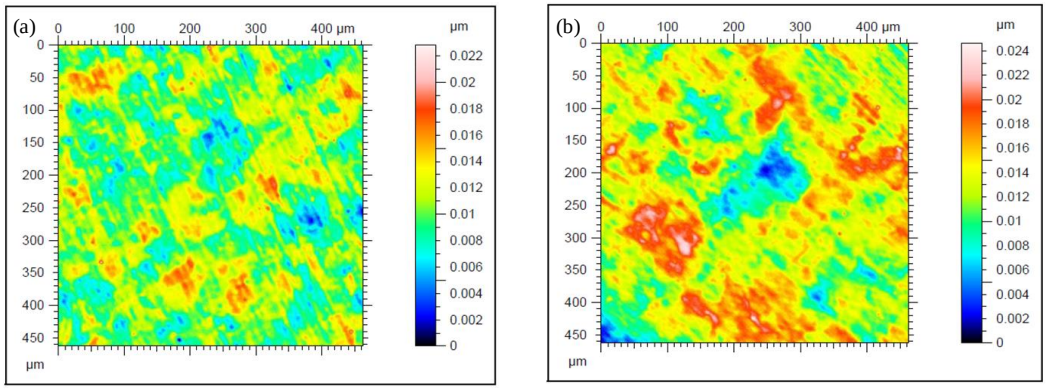

Parameters calculated on the surface before cutting (form removed, polynomial of order 2)

Amplitude Parameters:
S_a = 0.0018541 μm
S_q = 0.0023312 μm
S_z = 0.019278 μm

Parameters calculated on the surface after cutting (form removed, polynomial of order 2)

Amplitude Parameters:
S_a = 0.0025008 μm
S_q = 0.0031812 μm
S_z = 0.019631 μm

Figure 7-4: The surface roughness of workpiece (a) before nanoscale multi-tip tool cutting, and (b) after nanoscale multi-tip tool cutting (the lens was focused on the surface region between each cutting pass).

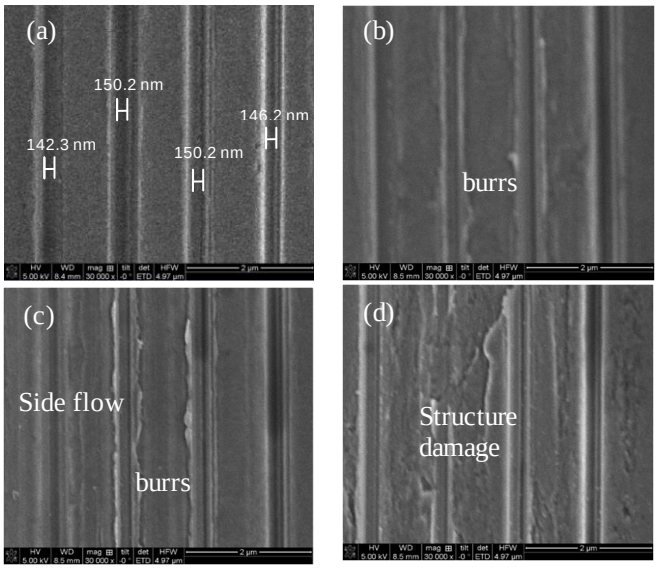

Figure 7-5: SEM images of nano-grooves machined using different depth of cut. (a) 100 nm; (b) 200 nm; (c) 300 nm; (d) 400 nm. (Cutting speed = 0.03 m/s, feed rate = 9 μm/re).

The SEM images of nanostructures machined at different cutting speeds are shown in figure 7-6 (depth of cut = 100 nm). The results show that the form accuracy of the machined

nano-grooves degrades with the increase of the cutting speed. No visible defect was found in the case of cutting speed being 0.03 m/s and 0.12 m/s. However, side burrs were observed when the cutting speed increased to 0.18 m/s. A similar cutting speed effect was observed when a depth of cut of 200 nm was used (figure 7-7). However, under a large depth of cut of 300 nm (figure 7-8), the increase of high cutting speed finally resulted in a seriously structure damage.

Therefore, it can be concluded that the burr and the structure damage are the two major types of machining defects when improper processing parameters are used in the nanoscale multi-tip tool cutting. The atomistic insight into the work material behaviour responsible for the formation of the machining defects will be discussed in the next section.

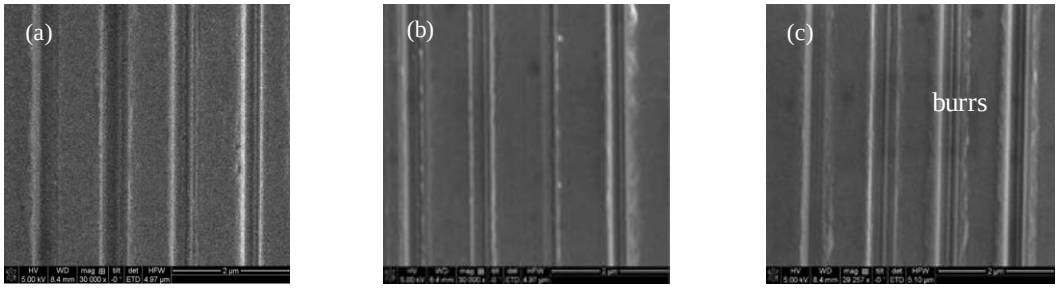

Figure 7-6: SEM images of nano-grooves machined under different cutting speed. (a) 0.03 m/s; (b) 0.12 m/s; (c) 0.18 m/s. (Depth of cut = 100 nm, feed rate = 9 μm/re).

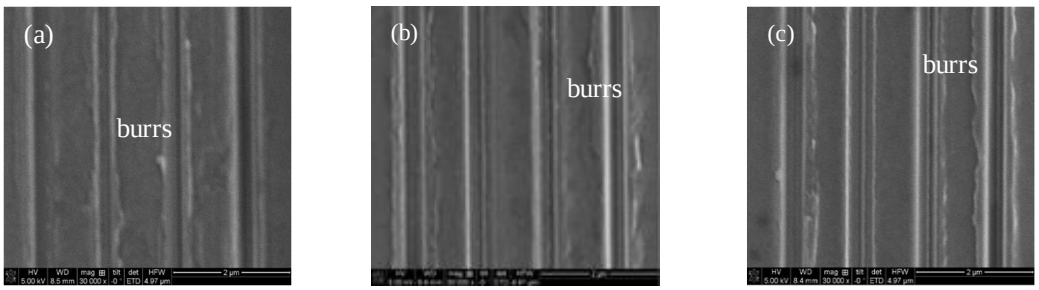

Figure 7-7: SEM images of nano-grooves machined under different cutting speed. (a) 0.03 m/s; (b) 0.12 m/s; (c) 0.18 m/s. (Depth of cut = 200 nm, feed rate = 9 μm/re).

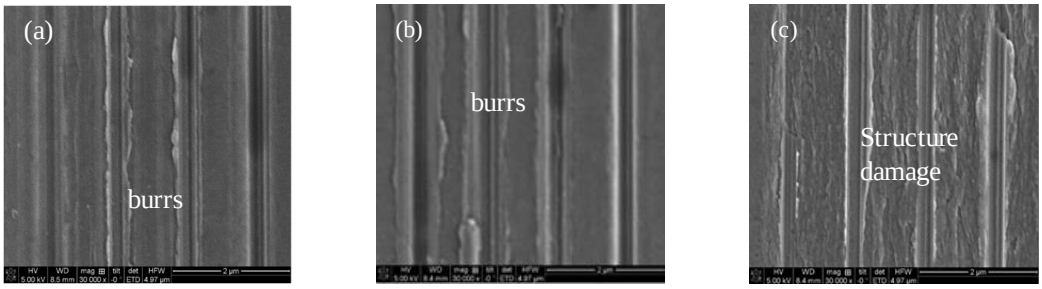

Figure 7-8: SEM images of nano-grooves machined under different cutting speed. (a) 0.03 m/s; (b) 0.12 m/s; (c) 0.18 m/s. (Depth of cut = 300 nm, feed rate = 9 μm/re).

7.4.2 Atomistic observation of the machining defects

7.4.2.1 Effects of depth of cut

In order to reveal the underlying mechanism for machining defects, an MD nanometric cutting model was built to simulate the nanometric cutting process when using a nanoscale multi-tip diamond tool. For better comparison, a ratio of depth of cut to tip height (d/h) was employed when comparing the simulation results with the experimental results. The quality of the machined nanostructures was characterized by both the form accuracy of the machined nanostructures achieved in depth direction and the thickness of the deformed layers. The form error was calculated by the deviation of the depth of machined nano-groove to the design dimension.

The machined nanostructures under different depths of cut are shown in figure 7-9. Two nano-grooves were successfully generated when a depth of cut of 2.0 nm (d/h = 0.46) was applied (figure 7-9 (a)). However, as evident from figures 7-9 (b)-(e), the form accuracy is degraded with the further increase of the depth of cut. Apparent side burrs were observed on both edges of the machined nano-grooves. The form error of nano-grooves in the depth direction is 4.0% when a depth of cut of 2.5 nm was used. It increased to 20% when cutting under the depth of cut of 4.0 nm.

Moreover, the wedge of cutting tool resulted in material pile-ups around tool tips. Visible

material bulge between the machined nano-grooves was found when a depth of cut of 2.5 nm was used (figure 7-9 (b)), mainly due to the overlap effect of the multi-tip tool cutting. However, with further increase of the depth of cut, the height of bulge reduced and it disappeared when a depth of cut of 3.5 nm (d/h = 0.81) was applied (figure 7-9 (d)). Apparently structure damage was found when a depth of cut of 4.0 nm (d/h = 0.93) was used (figure 7-9 (e)).

The thicknesses of the deformed layer when using different depths of cut are shown in the middle column of figure 7-9. Significant dislocation pile-ups were observed beneath the tool tips. The larger the depth of cut, the larger the range of the deformed layer and the dislocations pile-ups were observed. The dislocation pile-ups would result in local strengthening of the work material in the normal direction. The resistance force makes work materials in front of each tip and between the tips flow up. This trend resulted in the built up volume of each cutting tip merging into one big chip as shown in figures 7-9 (c)-(e). Due to the chip merging, the volume of chip and the height of the tool-chip separation point significantly increased. When the static friction force between the inner side of tool tip and the workpiece is large enough, adhesion slip takes place, and results in burrs and structure damage between the tool tips.

In the experimental work (figure 7-5), the visible machining defects are observed when the depth of cut is equal and larger than 300 nm (d/h = 0.51). In the MD simulation, the critical value of d/h for the onset of visible form errors (larger than 13.3%) is 0.70. It is larger than the experimental result which is mainly due to the ideally perfect single crystal structure of copper material and the cutting tool assumed in the MD simulation model. In practice, a small depth of cut is usually a necessary condition of improving the machining precision [220]. The current experimental and simulation results indicate that this rule also works for the nanoscale multi-tip diamond tool cutting.

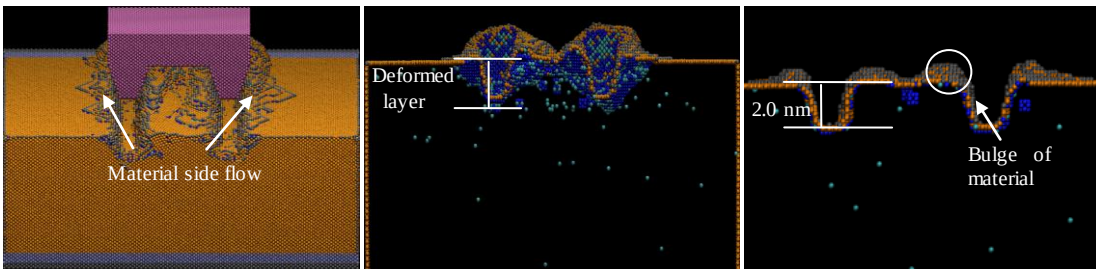

(a) 2.0 nm (d/h = 0.46)

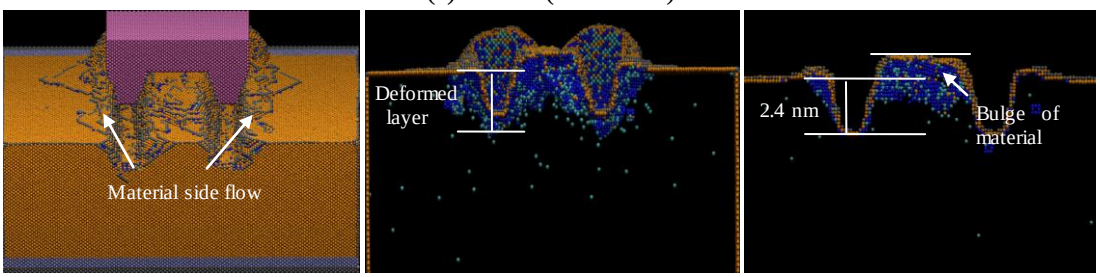

(b) 2.5 nm (d/h = 0.58)

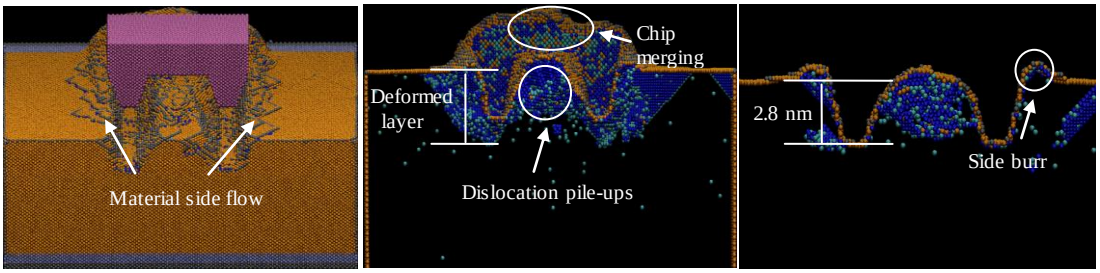

(c) 3.0 nm (d/h = 0.70)

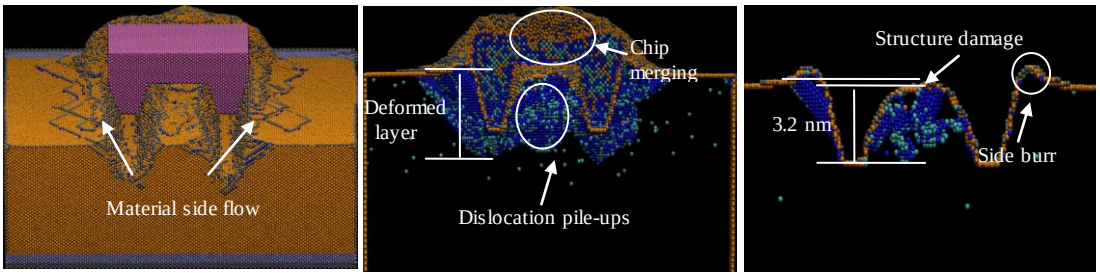

(d) 3.5 nm (d/h = 0.81)

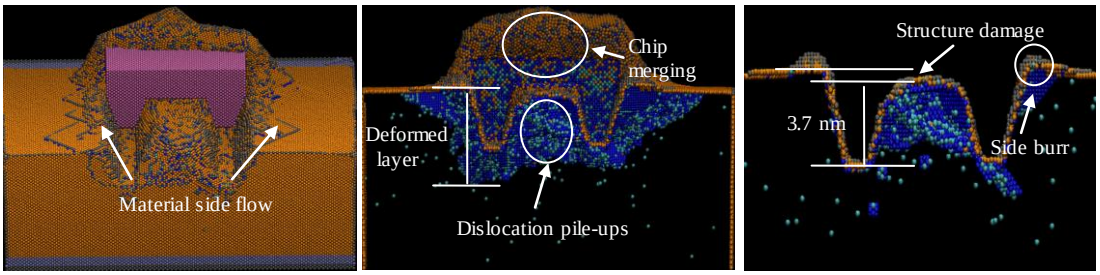

(e) 4.0 nm (d/h = 0.93)

Figure 7-9: MD simulation results of machined nanostructures (left), the cross-sectional views of deformed layers (middle), and the cross-sectional views of machined nano-grooves (right) using different depth of cut: (a) 2.0 nm, (b) 2.5 nm, (c) 3.0 nm, (d) 3.5 nm, (e) 4.0 nm.

7.4.2.2 Effects of cutting speed

In order to obtain in-depth understanding of the effect of cutting speed observed in the experiments, simulations of a nanometric cutting process using a multi-tip tool were performed over a wide range of cutting speeds (10–250 m/s) using the same depth of cut of 2.0 nm.

As shown in figure 7-10, nano-grooves were indicated when the cutting speed was lower than 160 m/s. With the wedge of cutting tool, each tip created a built up volume around tool tip. Although the tiny bulge of materials was observed when the cutting speed increase to 100 m/s, visible side burrs were found when the cutting speed was equal or higher than 200 m/s (figure 7-10 (e)). Moreover, dislocation pile-ups were found when the cutting speed increased to 160 m/s (right column of figure 7-10). This phenomenon indicates that the overlap effect took place when a high cutting speed was used.

Figure 7-11 summarizes the distributions of local cutting temperatures under different cutting speeds. As expected, the range of the high temperature region (> 450 K) significantly increases with the cutting speed. The high cutting temperature indicated in the high speed cutting would soften the work material at the cutting zone and extend the range of material plastic deformation zone, finally resulting in the overlap effect between the tool tips and the formation of the side burr. Although the range of the cutting speed used in simulations is still higher than the cutting speed used in experiment, the trend of the cutting speed effect obtained from simulations agreed with the experimental results qualitatively. The form accuracy of the machined nano-grooves degraded with the increase of cutting speed due to the formation of side burrs.

Nevertheless, it is noted that the form errors of the machined nanostructures in depth direction are all less than 5% for the cutting speed applied. Visible side burrs were observed only when the dislocation pile-ups took place. Thus it is predicted that, in nanoscale multi-tip tool cutting, there is a critical cutting speed below which the overlap effect can be ignored in

machining nanostructures under a certain acceptable accuracy. More nanometric cutting experiments need to be carried out in the future for a fully quantitative validation.

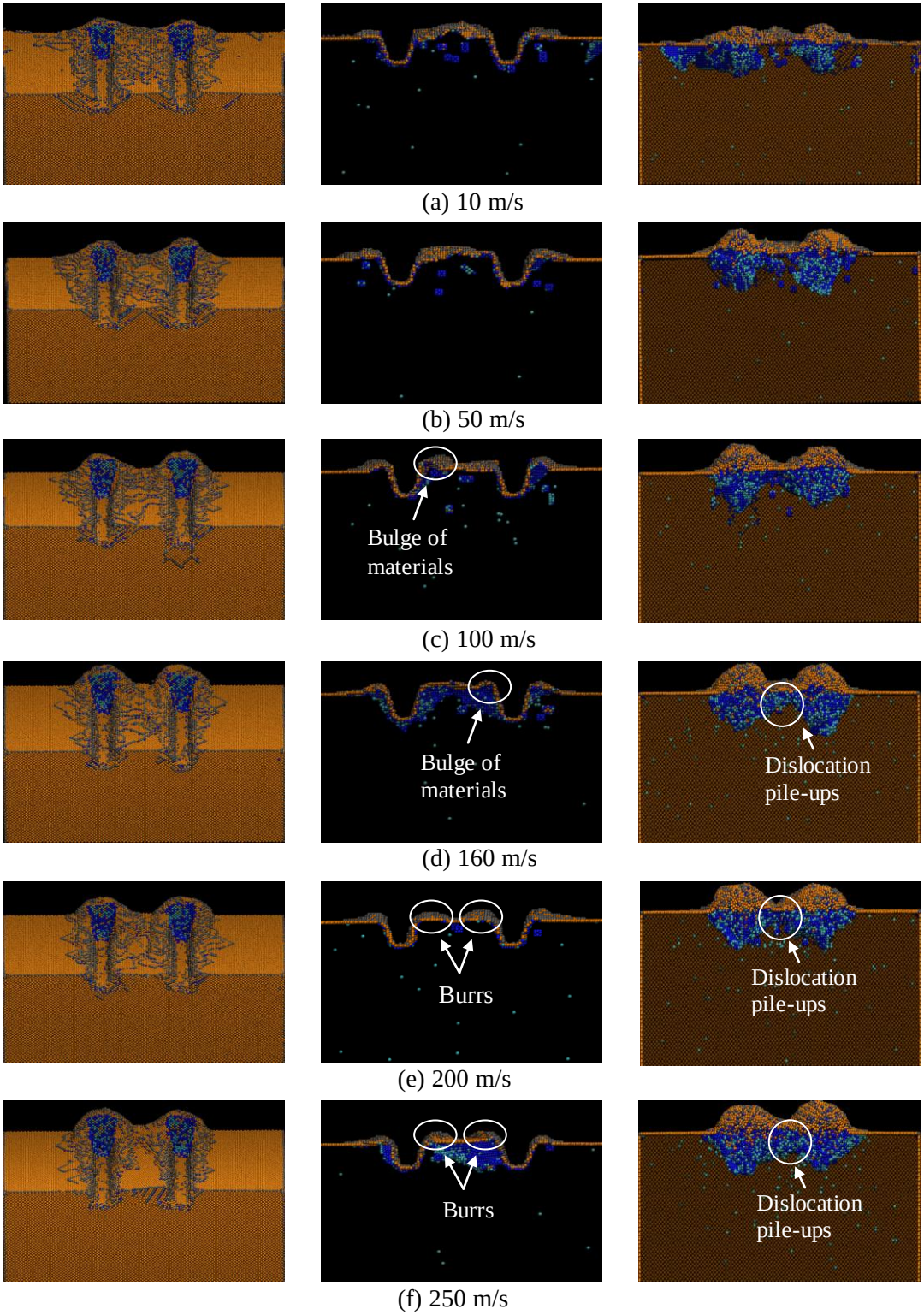

Figure 7-10: The MD simulation results of nanostructures formed using the cutting speed of:

(a) 10 m/s; (b) 50 m/s; (c) 100 m/s; (d) 160 m/s; (e) 200 m/s; (f) 250 m/s. The left column shows the surface of machined nanostructures; the middle column shows the cross-sectional view of formed nanostructures; the right column shows the inside view of the dislocation distribution under the cutting tool tips.

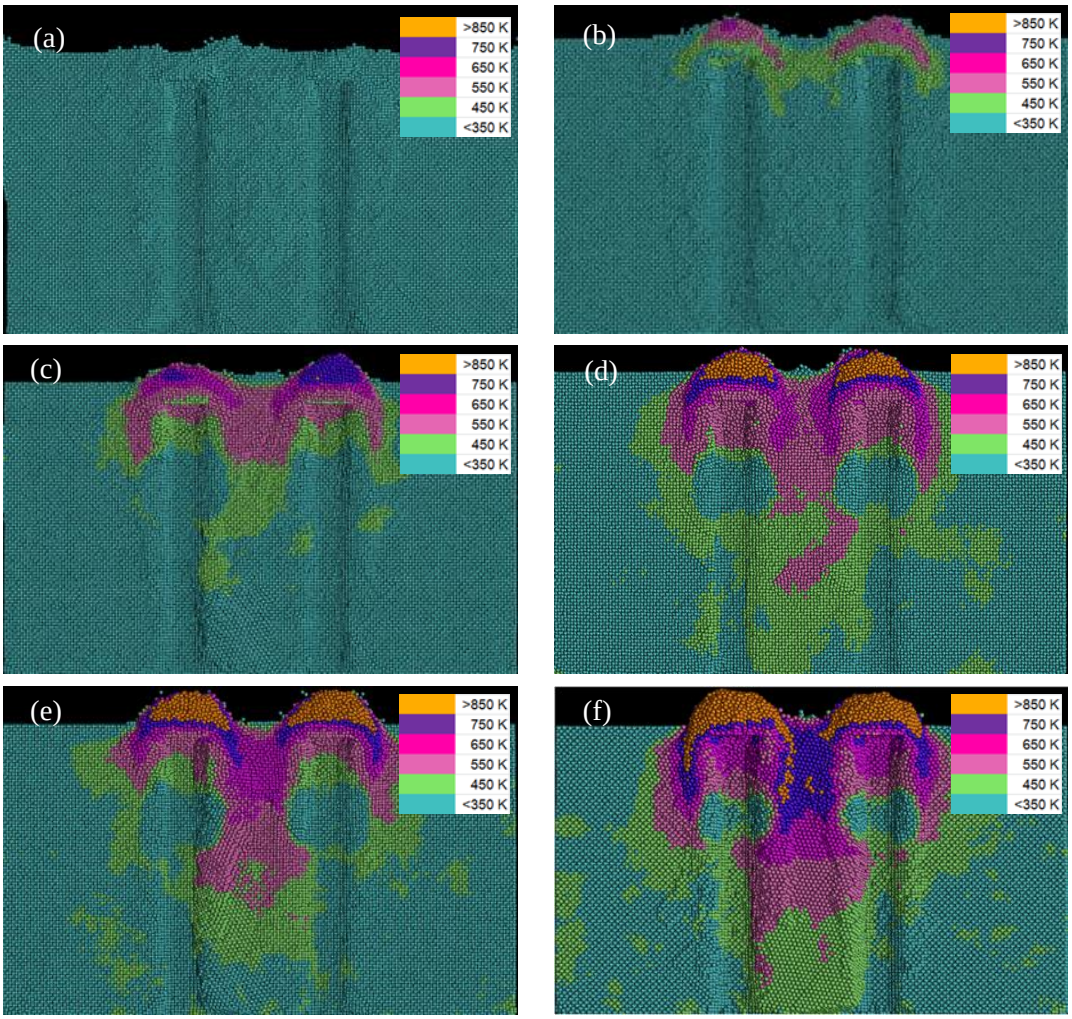

Figure 7-11: Temperature distribution under different cutting speed. (a) 10 m/s; (b) 50 m/s; (c) 100 m/s; (d) 160 m/s; (e) 200 m/s; (f) 250 m/s.

7.4.3 Tool wear

The SEM images of the nanoscale multi-tip diamond tool before and after the cutting trials are shown in figure 7-12. Unlike the conventional single tip diamond tool cutting where the

initial tool wear was mostly found at the clearance face near the tool cutting edges, the tool wear in the multi-tip tool cutting was found on both the clearance face and the sides of the tool tips after a cutting distance of 2.5 km. No visible wear marks were observed at the rake face of the tool tips. The measured tip distance enlarged from 706 nm to 743 nm because of the wear on the sides of the tool tips. The main reason of tool wear is that for multi-tip tool cutting, the nanostructures are formed synchronously within a single cutting pass. The sides of the tool tips are involved in the formation of nanostructures. The compressive stress produced at the sides of the tool tips results in the friction between the tool tip and workpiece, and thus results in the initiation of tool wear in this region.

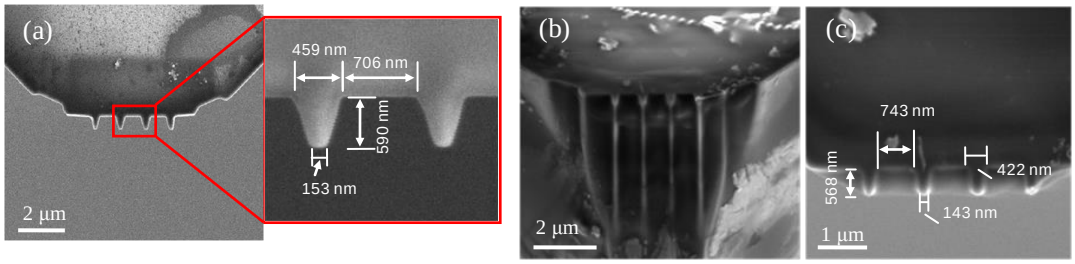

Figure 7-12: SEM images of the nanoscale multi-tip diamond tool. (a) SEM image of the tool before cutting; (b) SEM image of the tool cutting edges after cutting; and (c) a close up view of the shape of tool tips after cutting.

Moreover, the tool wear is closely related to the local cutting temperature. Many research works have emphasized the significance of thermal effects on tool wear and suggested that an important way to control the tool wear is to reduce the cutting temperature in the cutting zone [92, 95, 202]. Figures 7-13 (a)-(c) suggest the temperature distributions of tool tips for different depths of cut. It is found that the temperature was uniformly distributed at the tool tip when a small depth of cut of 2.0 nm was used. However, when cutting under a depth of cut of 3.0 nm, a high local temperature (> 620 K) was generated both at the cutting edges and the side edges of the tool tips. Similar results were observed when the depth of cut increased to 4.0 nm. This high local temperature would soften the C-C bonds and accelerate

the tool wear process in these regions.

In addition, it has been shown that a high cutting speed will apparently increase the cutting temperature at the cutting zone. It is anticipated that the tool wear rate will increase with the cutting speed as well.

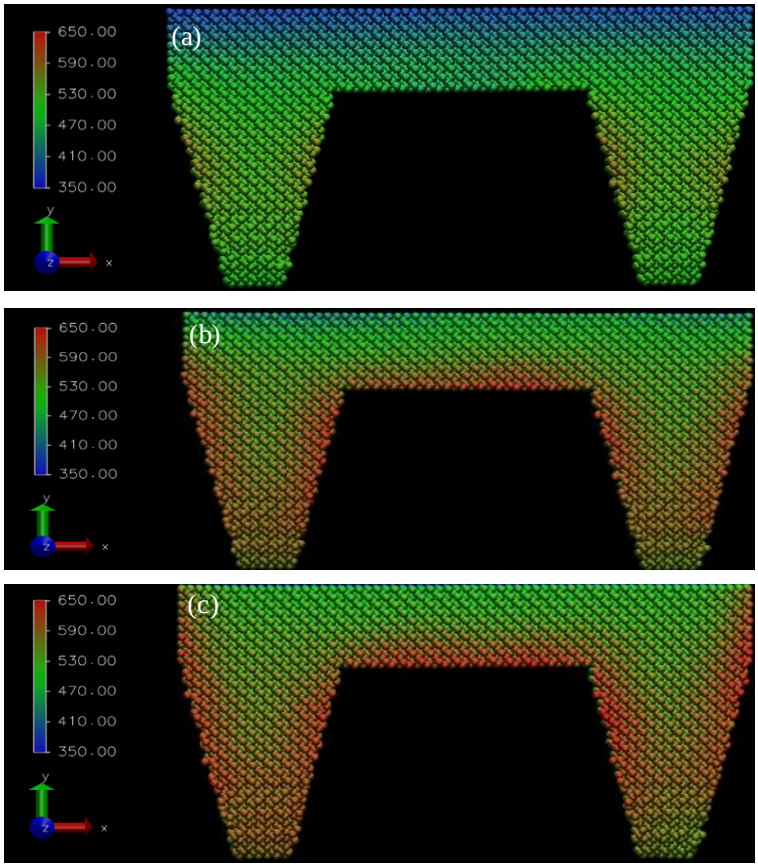

Figure 7-13: MD simulation results of the temperature distributions on the nanoscale multi-tip diamond tools for different depths of cut. (a) 2 nm; (b) 3.0 nm; and (c) 4.0 nm.

Usually, the progressive thermo-chemical wear of diamond tool is mainly attributed to the oxidation, graphitization, diffusion, and carbide formation during the long term cutting process. For FIB-shaped diamond tools, the ion irradiation induced doping and defects will also degrade the property of cutting tools. As a final note, previous study on ion-induced damaged layer during tool fabrication process (section 4.4-4.6 of Chapter 4) has shown that the energetic ion collision can result in an amorphous carbon layer around the tool tips. This

damaged layer would increase the adhesion between tool and work materials [147]. As schematically shown in figure 7-14, during the nanometric cutting process, the FIB-induced damaged layer was expected to worn away firstly because of its non-diamond phase. Most recently, similar phenomenon has been reported in micro machining of NiP using a FIB-irradiated single tip diamond tool [147, 221]. The present study, for the first time, provides significant information about the initial tool wear in the nanometric cutting of copper using a nanoscale multi-tip diamond tool. More research work needs to be carried out in the future to obtain a sufficient data for building a rigorous tool-life management and prediction program.

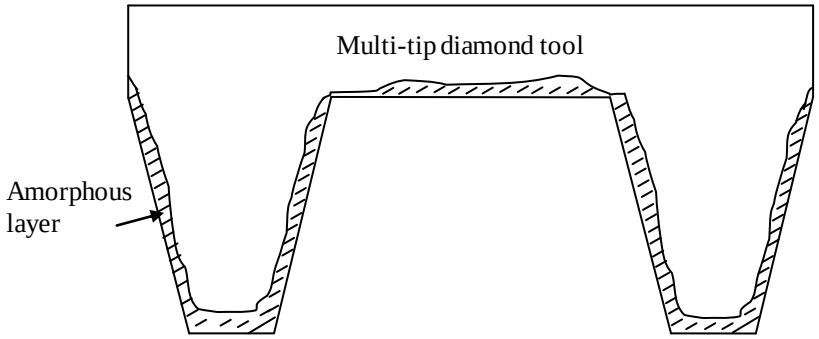

Figure 7-14: Schematical illustration of the early tool wear region of a multi-tip diamond tool resulting from FIB-induced damage.

To sum up, due to the limitation of current computational power, performing molecular dynamics (MD) simulation on nanometric cutting with the same physical size and small cutting speed used in experiments remains a big challenge, especially for the large scale MD model built in present work. However, this does not affect our analysis of the general nature of machining. Although it is not possible to have quantitative comparison to the experimental measurement, the MD nanometric cutting model allows the atomistic insight into the work material behaviour and reveals the underlying mechanisms for the machining defects as well as the tool wear during nanometric cutting process. The research findings obtained from MD simulations can help interpret the experimental data. The present analysis

will be valuable to any nanomanufacturing practice where a nanoscale multi-tip diamond tool is used. Therefore, if the full advantages of nanometric cutting using multi-tip diamond tool predicated by the MD simulations are to be realized, selection of parameters used in tool fabrication, optimal design of tool geometry, and optimization of processing parameters used in nanometric cutting practice, are critical to provide high performance and efficient machining when using nanoscale multi-tip diamond tools.

7.5 Summary

In this chapter, nanometric cutting experiments and MD simulations have been carried out to study the processing capability of diamond turning using a nanoscale multi-tip diamond tool. The operational parameters significantly affect the quality of the machined nanostructures. The high precision nanostructures were successfully produced by diamond face cutting under a depth of cut of 100 nm and a cutting speed of 0.03m/s. Under the studied cutting conditions, the burr and structure damage are the two major types of machining defects. The formation of machining defects has been emulated by MD simulations. The investigation showed that with the increase of the depth of cut and the cutting speed, the increasing overlap effect between the tool tips is responsible for the formation of side burr and structural damage. Moreover, the multi-tip tool wear has been initially characterized. The FIB-induced damaged layer, the cutting speed, and the depth of cut have significant effects on the tool wear. Based on the obtained results, it is reasonable to anticipate that, in nanoscale multi-tip tool cutting, high precision nanostructures can be achieved under an optimal cutting condition where the overlap effect can be ignored in the nanostructure generation process. More nanometric cutting experiments need to be carried out in the future for a fully quantitative validation.

Chapter 8 Conclusions and recommendations for future work

8.1 Assessment of the research

This research primarily aims at providing a fundamental understanding of the nanometric cutting using nanoscale multi-tip diamond tools fabricated by FIB. With this aim, atomic scale simulations and well-designed experiments have been performed to deliver a thorough investigation of the FIB-induced damage during the tool fabrication process, the geometry-dependent shape transferability of the nanoscale multi-tip diamond tools, and the multi-tip tool cutting technologies for nanostructures. The thesis has provided state-of-the-art insight in the development of manufacturing of nanostructures using nanoscale multi-tip diamond tools.

The novelty and contribution to knowledge from this research lie in:

- The development of a new multi-particle collision MD model to simulate the energetic ion irradiation process, which can provide both qualitative and quantitative descriptions of the dynamic structural damage produced in diamond under different FIB irradiation conditions.
- The nanocharacterization of FIB-induced damaged layer in a single crystal diamond tool, and the quantification and analysis of the effects of the beam voltage on the characteristics of the damaged layer.
- The development of the large scale MD simulation model to simulate the nanometric cutting process, which can represent the advantages and disadvantages of machining nanostructures between using a single tip and a multi-tip diamond tool.
- A comprehensive investigation and clarification, concerning the tool geometry-dependent shape transferability of nanoscale multi-tip diamond tools, has demonstrated the high processing capacity of using multi-tip diamond tools to fabricate high precision periodic and non-periodic nanostructures with various kinds

of cross-sectional shapes.

- The in-depth investigation of diamond turning using nanoscale multi-tip diamond tools under various cutting conditions, and the quantification of the influence of processing parameters on the formation of machining defects, the integrity of machined nanostructures, and the initialization of tool wear.

8.2 Conclusions

Using parallel molecular dynamics simulations in junction with TEM experiments, this thesis provides quantitative understanding of the dynamic damage process of FIB machining and the characteristics of the FIB-induced damaged layer in a single crystal diamond tool under different beam voltages.

The nanometric cutting processes using nanoscale multi-tip diamond tools are modelled and simulated by MD simulation method. The distinct MD algorithm developed in this work provides an in-depth understanding of the nanostructure generation process, the cutting force, the thermal effect, the tool geometry-dependent shape transferability, and the influence of machining parameters on the integrity of the machined nanostructures and tool wear. The simulation results have been qualitatively validated by nanometric cutting experiments using nanoscale multi-tip diamond tools.

The major results meeting the research objectives can be summarised as follows:

(a) During FIB processing of cutting tools made of natural single crystal diamond, the energetic Ga^+ collision will create a damaged layer (a mixture phase of sp^2 and sp^3 hybridization carbon and a proportion of the implanted gallium) around tool tips. For the tested beam voltages in a typical FIB system (from 8 kV to 30 kV), the thicknesses of the damaged layers formed on a diamond tool surface increased from 11.5 nm to 27.6 nm. Because the residual damaged layer around tool tips will wear first during nanometric cutting, low-energy FIB polishing is recommended when milling the diamond tool tip by FIB.

(b) Through MD simulation of energetic ion collisions with diamond, it is found that the thickness and the amorphization level of the damaged layer in diamond depend significantly on the kinetic energy of incident gallium particles. The formation of atomic defects, the thermal spike, and the local recrystallization of atomic defects indicate the dynamic nature of diamond amorphization.

(c) The MD simulations results show that the mechanisms of nanostructure formation by using single tip tools and multi-tip tools are different. Compared with the single tip tool cutting, a higher cutting temperature and a higher average normal cutting force per tip were found in the multi-tip tool cutting. Since the nanostructures are synchronously formed by a single cutting pass, the effect of feed rate and the alignment issues associated with the use of single tip tools can be completely eliminated when using nanoscale multi-tip tools. This unique feature makes the multi-tip tool cutting more practicable and applicable than the single tip cutting for scale-up fabrication of periodic nanostructures.

(d) The MD simulation results indicate that tool geometrical parameters have significant influence on the shape transferability of the nanoscale multi-tip diamond tool. The ratio of L/W_f should be carefully considered when designing nanoscale multi-tip diamond tools. A multi-tip tool with a tip angle equal to or greater than $11.8°$ can improve the form accuracy of the nanostructures by reducing the cutting force and the interactions of the deformed layers beneath the tool tips. The periodic tip configuration has better shape transferability than the non-periodic tip configuration.

(e) The overlap of the work-affected layers significantly affects the shaping capacity of the nanoscale multi-tip tools. The MD simulation results show that, in nanometric cutting process, the significant dislocation pile-ups beneath the tips would result in a local strengthening of the work material in the normal direction. The resistant force drives the material to flow plastically in the upward direction. When the ratio of L/W_f, or the depth of cut, or the cutting speed exceed their critical values, the overlap of

the material plastic deformation will cause the formation of side burrs and structure damage. The side burr and structure damage are the two major types of machining defects found in this study.

(f) The tool wear is initially found at both the clearance cutting edge and the side edges of tool tips after a cutting distance of 2.5 km. The FIB-induced damaged layer and the friction produced at each side of the tool tip are responsible for the tool wear.

(g) The operational parameters significantly affect the quality of the machined nanostructures. The high precision nanostructures were successfully produced by diamond face cutting under a depth of cut of 100 nm and a cutting speed of 0.03m/s. An optimization of the cutting conditions, by which the overlap effect can be ignored in the nanostructure generation process, is recommended in the future work to obtain high precision nanostructures when using nanoscale multi-tip diamond tools.

8.3 Limitations of the research

Currently, it is still quite difficult to compare MD simulations with experimental results in the same spatial and time scale. From the MD simulation side, the difficulties lie in developing a super high performance computing system for solving a highly inhomogeneous multi body problem having the same spatial and time scales as experiments, as well as an effective visualization technique for analysing the large-scale MD simulation results. The difficulties from experimental side have been the limitation of using FIB to fabricate multi-tip diamond tool with tool tips in several nanometres, and the time resolution that is needed for a detection equipment to capture the transient process of defects formation which evolve on time scales of some nanoseconds.

In this research work, the cutting speeds used in the MD simulations are much higher than those applied in the experiments in order to speed up the MD computations. The tip geometry of the tool model is a scaled down version of the tools used in experiments. The ratio of tool tip distance to tool tip base width (L/W_f), and the ratio of depth of cut to tool tip

height (d/h) were employed as indicators when comparing the MD simulation results with the experiments. By considering these geometrical details, the simulation results of the shape transferability of a nanoscale multi-tip diamond tool were qualitatively verified by the nanometric cutting experiments. However, due to the high cutting speeds used in simulations, the thermal effects on the formation of nanostructures and tool wear obtained from the MD simulations could not verified by experiments. More experimental tests are needed in the future to determine the critical values of tool geometrical parameters and processing parameters to be used in practice for specific applications.

8.4 Recommendations for future work

8.4.1 Developing an effective post-processing method for tool fabrication

The present study on FIB-induced damage in diamond has demonstrated that the energetic ion collision can result in a damaged zone (a mixture phase of sp^2 and sp^3 hybridization and the implanted gallium), which is much larger than the defined ion irradiated area, even under the low beam energy of 8 kV. Most recently, it has been reported that the doping of gallium ions at tool rake face would result in a rapid diamond tool wear due to the increase of the adhesion of work materials to the tool surface [147]. Thus, the ion irradiation induced doping and defects will unavoidably degrade the cutting performance of the micro- and nanoscale diamond tools fabricated by FIB. An effective post-processing method which is able to remove/minimize the damaged layers after FIB machining is in high demand. The minimization of the FIB-induced damaged layer will become more important when the dimensions of a multi-tip diamond tool are approaching their ultimate values.

8.4.2 Optimization of the design of multi-tip diamond tools

It is widely known in conventional cutting that the tool geometrical parameters such as the rake angle, clearance angle, and the cutting edge radius can influence the material removal

process. As shown in this study, the unique tool geometrical parameters of a multi-tip tool including the tool tip distance, tip angle, and tip configuration can play an important role in achieving high the accuracy of the machined nanostructures. It seems to be a complex interplay of all these variables in order to obtain a deterministic fabrication of high quality nanostructures. Therefore, an optimization of the tool design by considering all these parameters, can further improve the shape transferability of multi-tip diamond tools in an SPDT operation.

8.4.3 Setting up a processing database of the multi-tip tool cutting

The processing parameters such as depth of cut and cutting speed significantly affect the attainable integrity of machined nanostructures as well as the tool life. Due to the limitations of time and the high research cost of using relevant equipment, the experimental results obtained in the present study were not sufficient to set up a processing database for the nanometric cutting of copper using nanoscale multi-tip diamond tools. Currently, the processing parameters such as the maximum feed rate, depth of cut, and cutting speed for a specialized workpiece material have not yet been established. For the commercialization of this technique in industry, more research work needs to be carried out in the future to obtain sufficient database for building a rigorous tool-life management and predication program, and eventually an expert system for intelligently selecting optimal processing parameters for the cost effective scale-up manufacturing of nanostructures.

References

[1] S. Holmberg, A. Perebikovsky, L. Kulinsky, and M. Madou, "3-D Micro and Nano Technologies for Improvements in Electrochemical Power Devices," *Micromachines,* vol. 5, pp. 171-203, 2014.

[2] P. Bartolo, J.-P. Kruth, J. Silva, G. Levy, A. Malshe, K. Rajurkar, *et al.*, "Biomedical production of implants by additive electro-chemical and physical processes," *CIRP Annals-Manufacturing Technology,* vol. 61, pp. 635-655, 2012.

[3] D. Berman and J. Krim, "Surface science, MEMS and NEMS: Progress and opportunities for surface science research performed on, or by, microdevices," *Progress in Surface Science,* vol. 88, pp. 171-211, 2013.

[4] I. P. Kaur and H. Singh, "Nanostructured drug delivery for better management of tuberculosis," *Journal of Controlled Release,* vol. 184, pp. 36-50, 2014.

[5] C. Vieu, F. Carcenac, A. Pepin, Y. Chen, M. Mejias, A. Lebib, *et al.*, "Electron beam lithography: resolution limits and applications," *Applied Surface Science,* vol. 164, pp. 111-117, 2000.

[6] W. Chen and H. Ahmed, "Fabrication of 5 – 7 nm wide etched lines in silicon using 100 keV electron - beam lithography and polymethylmethacrylate resist," *Applied physics letters,* vol. 62, pp. 1499-1501, 1993.

[7] C. M. Kolodziej and H. D. Maynard, "Electron-beam lithography for patterning biomolecules at the micron and nanometer scale," *Chemistry of materials,* vol. 24, pp. 774-780, 2012.

[8] M. Urbánek, V. Uhlíř, P. Bábor, E. Kolíbalová, T. Hrnčíř, J. Spousta, *et al.*, "Focused ion beam fabrication of spintronic nanostructures: an optimization of the milling process," *Nanotechnology,* vol. 21, p. 145304, 2010.

[9] H. W. Li, D. J. Kang, M. Blamire, and W. T. Huck, "Focused ion beam fabrication of silicon print masters," *Nanotechnology,* vol. 14, p. 220, 2003.

[10] A. A. Tseng, "Recent developments in nanofabrication using focused ion beams," *Small,* vol. 1, pp. 924-939, 2005.

[11] A. A. Tseng, "Recent developments in micromilling using focused ion beam technology," *Journal of Micromechanics and Microengineering,* vol. 14, p. R15, 2004.

[12] K. Salaita, Y. Wang, and C. A. Mirkin, "Applications of dip-pen nanolithography," *Nature Nanotechnology,* vol. 2, pp. 145-155, 2007.

[13] J. Kim, Y. H. Shin, S. H. Yun, D. S. Choi, J. H. Nam, S. R. Kim, *et al.*, "Direct-write patterning of bacterial cells by dip-pen nanolithography," *Journal of the American Chemical Society,* vol. 134, pp. 16500-16503, 2012.

[14] D. S. Ginger, H. Zhang, and C. A. Mirkin, "The Evolution of Dip‐Pen Nanolithography," *Angewandte Chemie International Edition,* vol. 43, pp. 30-45, 2004.

[15] L. J. Guo, "Nanoimprint lithography: methods and material requirements," *Advanced Materials,* vol. 19, pp. 495-513, 2007.

[16] A. Chimmalgi, C. Grigoropoulos, and K. Komvopoulos, "Surface nanostructuring by nano-/femtosecond laser-assisted scanning force microscopy," *Journal of Applied Physics,* vol. 97, p. 104319, 2005.

[17] M. Meunier, B. Fisette, A. Houle, A. V. Kabashin, S. V. Broude, and P. Miller, "Processing of metals and semiconductors by a femtosecond laser-based microfabrication system," in *High-Power Lasers and Applications*, 2003, pp. 169-179.

[18] B. Poumellec, M. Lancry, A. Chahid-Erraji, and P. Kazansky, "Modification thresholds in femtosecond laser processing of pure silica: review of dependencies on laser parameters [Invited]," *Optical Materials Express,* vol. 1, pp. 766-782, 2011.

[19] K. Sugioka and Y. Cheng, "Femtosecond laser processing for optofluidic fabrication," *Lab on a Chip,* vol. 12, pp. 3576-3589, 2012.

[20] X. Luo, K. Cheng, D. Webb, and F. Wardle, "Design of ultraprecision machine tools with applications to manufacture of miniature and micro components," *Journal of Materials*

Processing Technology, vol. 167, pp. 515-528, 2005.

[21] E. Brinksmeier, R. Gläbe, and L. Schönemann, "Diamond Micro Chiseling of large-scale retroreflective arrays," *Precision Engineering,* vol. 36, pp. 650-657, 2012.

[22] J. Yan, K. Maekawa, J. i. Tamaki, and T. Kuriyagawa, "Micro grooving on single-crystal germanium for infrared Fresnel lenses," *Journal of micromechanics and microengineering,* vol. 15, p. 1925, 2005.

[23] F. Fang and Y. Liu, "On minimum exit-burr in micro cutting," *Journal of Micromechanics and Microengineering,* vol. 14, p. 984, 2004.

[24] E. Brinksmeier, R. Gläbe, and L. Schönemann, "Review on diamond-machining processes for the generation of functional surface structures," *CIRP Journal of Manufacturing Science and Technology,* vol. 5, pp. 1-7, 2012.

[25] Z. Gan, Y. Cao, R. A. Evans, and M. Gu, "Three-dimensional deep sub-diffraction optical beam lithography with 9 nm feature size," *Nature communications,* vol. 4, 2013.

[26] V. R. Manfrinato, L. Zhang, D. Su, H. Duan, R. G. Hobbs, E. A. Stach, *et al.*, "Resolution limits of electron-beam lithography toward the atomic scale," *Nano letters,* vol. 13, pp. 1555-1558, 2013.

[27] A. Lugstein, B. Basnar, J. Smoliner, and E. Bertagnolli, "FIB processing of silicon in the nanoscale regime," *Applied Physics A,* vol. 76, pp. 545-548, 2003.

[28] L. D. Menard and J. M. Ramsey, "Fabrication of sub-5 nm nanochannels in insulating substrates using focused ion beam milling," *Nano letters,* vol. 11, pp. 512-517, 2010.

[29] D. Pires, J. L. Hedrick, A. De Silva, J. Frommer, B. Gotsmann, H. Wolf, *et al.*, "Nanoscale three-dimensional patterning of molecular resists by scanning probes," *Science,* vol. 328, pp. 732-735, 2010.

[30] X. Ding, D. Butler, G. Lim, C. Cheng, K. Shaw, K. Liu, *et al.*, "Machining with micro-size single crystalline diamond tools fabricated by a focused ion beam," *Journal of Micromechanics and Microengineering,* vol. 19, p. 025005, 2009.

[31] D. Banks, *Microengineering, MEMS, and interfacing: a practical guide*: CRC press,

2006.

[32] Y. N. Picard, D. Adams, M. Vasile, and M. Ritchey, "Focused ion beam-shaped microtools for ultra-precision machining of cylindrical components," *Precision Engineering*, vol. 27, pp. 59-69, Jan 2003.

[33] X. Ding, G. Lim, C. Cheng, D. L. Butler, K. Shaw, K. Liu, *et al.*, "Fabrication of a micro-size diamond tool using a focused ion beam," *Journal of Micromechanics and Microengineering*, vol. 18, p. 075017, 2008.

[34] Z. Xu, F. Fang, S. Zhang, X. Zhang, X. Hu, Y. Fu, *et al.*, "Fabrication of micro DOE using micro tools shaped with focused ion beam," *Optics express*, vol. 18, pp. 8025-8032, 2010.

[35] X. Luo, Z. Tong, and Y. Liang, "Investigation of the shape transferability of nanoscale multi-tip diamond tools in the diamond turning of nanostructures," *Applied Surface Science*, vol. 321, pp. 495-502, 2014.

[36] J. Sun and X. Luo, *Deterministic Fabrication of Micro-and Nanostructures by Focused Ion Beam*: Springer, 2013.

[37] H. Kanda and S. Yamaoka, "Inhomogeneous distribution of nitrogen impurities in {111} growth sectors of high pressure synthetic diamond," *Diamond and Related Materials*, vol. 2, pp. 1420-1423, 1993.

[38] M. Kamo, Y. Sato, S. Matsumoto, and N. Setaka, "Diamond synthesis from gas phase in microwave plasma," *Journal of Crystal Growth*, vol. 62, pp. 642-644, 1983.

[39] M. Werner and R. Locher, "Growth and application of undoped and doped diamond films," *Reports on Progress in Physics*, vol. 61, p. 1665, 1998.

[40] T. N. Makgato, "Formation of surface diamond-like nanostructures on graphite induced by highly charged ion irradiation," Faculty of Science, University of the Witwatersrand, 2010.

[41] T. Meguro, Y. Yamaguchi, H. Fukagawa, H. Takai, N. Hanano, Y. Yamamoto, *et al.*, "Nanoscale modification of electronic states of HOPG by the single impact of HCI," *Nuclear*

Instruments and Methods in Physics Research Section B: Beam Interactions with Materials and Atoms, vol. 235, pp. 431-437, 2005.

[42] F. Picollo, P. Olivero, F. Bellotti, Ž. Pastuović, N. Skukan, A. L. Giudice, *et al.*, "Formation of buried conductive micro-channels in single crystal diamond with MeV C and He implantation," *Diamond and Related Materials,* vol. 19, pp. 466-469, 2010.

[43] D. D. Cheam, K. A. Walczak, M. Archaya, C. R. Friedrich, and P. L. Bergstrom, "Leakage current in single electron device due to implanted gallium dopants by focus ion beam," *Microelectronic Engineering,* vol. 88, pp. 1906-1909, 2011.

[44] I. Jain and G. Agarwal, "Ion beam induced surface and interface engineering," *Surface Science Reports,* vol. 66, pp. 77-172, 2011.

[45] W. McKenzie, M. Z. Quadir, M. Gass, and P. Munroe, "Focused ion beam implantation of diamond," *Diamond and Related Materials,* vol. 20, pp. 1125-1128, 2011.

[46] S. Rubanov and A. Suvorova, "Ion implantation in diamond using 30keV Ga+ focused ion beam," *Diamond and Related Materials*, vol. 20, pp. 1160-1164, 2011.

[47] W. Zong, T. Sun, D. Li, K. Cheng, and Z. Li, "Nano-precision diamond cutting tools achieved by mechanical lapping versus thermo-mechanical lapping," *Diamond and Related Materials,* vol. 17, pp. 954-961, 2008.

[48] H. Ohmori, K. Katahira, T. Naruse, Y. Uehara, A. Nakao, and M. Mizutani, "Microscopic grinding effects on fabrication of ultra-fine micro tools," *CIRP Annals-Manufacturing Technology,* vol. 56, pp. 569-572, 2007.

[49] C. J. Morgan, R. R. Vallance, and E. R. Marsh, "Micro machining glass with polycrystalline diamond tools shaped by micro electro discharge machining," *Journal of Micromechanics and Microengineering*, vol. 14, p. 1687, 2004.

[50] W. Zong, Z. Li, T. Sun, K. Cheng, D. Li, and S. Dong, "The basic issues in design and fabrication of diamond-cutting tools for ultra-precision and nanometric machining," *International Journal of Machine Tools and Manufacture,* vol. 50, pp. 411-419, 2010.

[51] S. Zhang, F. Fang, Z. Xu, and X. Hu, "Controlled morphology of microtools shaped

using focused ion beam milling technique," *Journal of Vacuum Science & Technology B,* vol. 27, pp. 1304-1309, 2009.

[52] C. R. Friedrich and M. J. Vasile, "Development of the micromilling process for high-aspect-ratio microstructures," *Microelectromechanical Systems, Journal of,* vol. 5, pp. 33-38, 1996.

[53] J. Sun, X. Luo, W. Chang, J. Ritchie, J. Chien, and A. Lee, "Fabrication of periodic nanostructures by single-point diamond turning with focused ion beam built tool tips," *Journal of Micromechanics and Microengineering,* vol. 22, p. 115014, 2012.

[54] D. Adams, M. Vasile, T. Mayer, and V. Hodges, "Focused ion beam milling of diamond: effects of H 2 O on yield, surface morphology and microstructure," *Journal of Vacuum Science & Technology B: Microelectronics and Nanometer Structures,* vol. 21, pp. 2334-2343, 2003.

[55] M. J. Vasile, R. Nassar, J. Xie, and H. Guo, "Microfabrication techniques using focused ion beams and emergent applications," *Micron,* vol. 30, pp. 235-244, 1999.

[56] M. J. Vasile, C. R. Friedrich, B. Kikkeri, and R. McElhannon, "Micrometer-scale machining: tool fabrication and initial results," *Precision Engineering,* vol. 19, pp. 180-186, 1996.

[57] C. Friedrich, P. Coane, and M. Vasile, "Micromilling development and applications for microfabrication," *Microelectronic engineering,* vol. 35, pp. 367-372, 1997.

[58] X. Ding, A. Jarfors, G. Lim, K. Shaw, Y. Liu, and L. Tang, "A study of the cutting performance of poly-crystalline oxygen free copper with single crystalline diamond micro-tools," *Precision engineering,* vol. 36, pp. 141-152, 2012.

[59] F. Fang, X. Zhang, A. Weckenmann, G. Zhang, and C. Evans, "Manufacturing and measurement of freeform optics," *CIRP Annals-Manufacturing Technology,* vol. 62, pp. 823-846, 2013.

[60] D. L. Trumper and X. Lu, "Fast tool servos: advances in precision, acceleration, and bandwidth," in *Towards Synthesis of Micro-/Nano-systems,* ed: Springer, 2007, pp. 11-19.

[61] E. Brinksmeier, O. Riemer, R. Gläbe, B. Lünemann, C. Kopylow, C. Dankwart, *et al.*, "Submicron functional surfaces generated by diamond machining," *CIRP Annals-Manufacturing Technology,* vol. 59, pp. 535-538, 2010.

[62] Y. E. Tohme and J. A. Lowe, "Machining of freeform optical surfaces by slow slide servo method," in *Proceedings of the American Society for Precision Engineering*, 2003.

[63] Y. Dai, C. Guan, Z. Yin, G. Tie, H. Chen, and J. Wang, "Tool decentration effect in slow tool servo diamond turning off-axis conic aspheric surface," in *5th International Symposium on Advanced Optical Manufacturing and Testing Technologies*, 2010, pp. 76550P-76550P-6.

[64] F. Fang, X. Zhang, and X. Hu, "Cylindrical coordinate machining of optical freeform surfaces," *Optics Express,* vol. 16, pp. 7323-7329, 2008.

[65] C. Huang, L. Li, and Y. Y. Allen, "Design and fabrication of a micro Alvarez lens array with a variable focal length," *Microsystem Technologies,* vol. 15, pp. 559-563, 2009.

[66] D. W. K. Neo, A. S. Kumar, and M. Rahman, "A novel surface analytical model for cutting linearization error in fast tool/slow slide servo diamond turning," *Precision Engineering,* 2014.

[67] Z. Yin, Y. Dai, S. Li, C. Guan, and G. Tie, "Fabrication of off-axis aspheric surfaces using a slow tool servo," *International Journal of Machine Tools and Manufacture,* vol. 51, pp. 404-410, 2011.

[68] W. K. Neo, M. D. Nadhan, A. S. Kumar, and M. Rahman, "A Novel Method for Profile Error Analysis of Freeform Surfaces in FTS/STS Diamond Turning," in *Key Engineering Materials*, 2014, pp. 101-107.

[69] X. Zhang, F. Fang, Q. Wu, X. Liu, and H. Gao, "Coordinate transformation machining of off-axis aspheric mirrors," *The International Journal of Advanced Manufacturing Technology,* vol. 67, pp. 2217-2224, 2013.

[70] D. P. Adams, M. J. Vasile, G. Benavides, and A. N. Campbell, "Micromilling of metal alloys with focused ion beam–fabricated tools," *Precision Engineering,* vol. 25, pp. 107-113,

2001.

[71] R. M. Bradley and J. M. Harper, "Theory of ripple topography induced by ion bombardment," *Journal of Vacuum Science & Technology A*, vol. 6, pp. 2390-2395, 1988.

[72] H. B. Kim, G. Hobler, A. Lugstein, and E. Bertagnolli, "Simulation of ion beam induced micro/nano fabrication," *Journal of Micromechanics and Microengineering*, vol. 17, p. 1178, 2007.

[73] J. F. Ziegler, "SRIM-2003," *Nuclear instruments and methods in physics research section B: Beam interactions with materials and atoms*, vol. 219, pp. 1027-1036, 2004.

[74] W. Möller and W. Eckstein, "Tridyn—a TRIM simulation code including dynamic composition changes," *Nuclear Instruments and Methods in Physics Research Section B: Beam Interactions with Materials and Atoms*, vol. 2, pp. 814-818, 1984.

[75] W. Möller, W. Eckstein, and J. Biersack, "Tridyn-binary collision simulation of atomic collisions and dynamic composition changes in solids," *computer physics communications*, vol. 51, pp. 355-368, 1988.

[76] C.S. Kim, S.H. Ahn, and D.Y. Jang, "Review: developments in micro/nanoscale fabrication by focused ion beams," *Vacuum*, vol. 86, pp. 1014-1035, 2012.

[77] M. Solar, H. Meyer, C. Gauthier, C. Fond, O. Benzerara, R. Schirrer, *et al.*, "Mechanical behavior of linear amorphous polymers: Comparison between molecular dynamics and finite-element simulations," *Physical Review E*, vol. 85, p. 021808, 2012.

[78] P. J. Arrazola and T. Özel, "Investigations on the effects of friction modeling in finite element simulation of machining," *International Journal of Mechanical Sciences*, vol. 52, pp. 31-42, 2010.

[79] K. Liu and S. N. Melkote, "Finite element analysis of the influence of tool edge radius on size effect in orthogonal micro-cutting process," *International Journal of Mechanical Sciences*, vol. 49, pp. 650-660, 2007.

[80] K. Bobzin, N. Bagcivan, D. Parkot, T. Kashko, G. Laschet, and J. Scheele, "Influence of the definition of the representative volume element on effective thermoelastic properties

of thermal barrier coatings with random microstructure," *Journal of Thermal Spray Technology,* vol. 18, pp. 988-995, 2009.

[81] T. Kanit, S. Forest, I. Galliet, V. Mounoury, and D. Jeulin, "Determination of the size of the representative volume element for random composites: statistical and numerical approach," *International Journal of Solids and Structures,* vol. 40, pp. 3647-3679, 2003.

[82] W. Drugan and J. Willis, "A micromechanics-based nonlocal constitutive equation and estimates of representative volume element size for elastic composites," *Journal of the Mechanics and Physics of Solids,* vol. 44, pp. 497-524, 1996.

[83] S. Abolfazl Zahedi, M. Demiral, A. Roy, and V. V. Silberschmidt, "FE/SPH modelling of orthogonal micro-machining of fcc single crystal," *Computational Materials Science,* vol. 78, pp. 104-109, 2013.

[84] P. Arrazola, T. Özel, D. Umbrello, M. Davies, and I. Jawahir, "Recent advances in modelling of metal machining processes," *CIRP Annals-Manufacturing Technology,* vol. 62, pp. 695-718, 2013.

[85] B. Alder and T. Wainwright, "Phase transition for a hard sphere system," *The Journal of Chemical Physics,* vol. 27, pp. 1208-1209, 1957.

[86] J. Belak, D. B. Boercker, and I. F. Stowers, "Simulation of nanometer-scale deformation of metallic and ceramic surfaces," *MRS Bulletin,* vol. 18, pp. 55-60, 1993.

[87] T. Inamura, N. Takezawa, Y. Kumaki, and T. Sata, "On a possible mechanism of shear deformation in nanoscale cutting," *CIRP Annals-Manufacturing Technology,* vol. 43, pp. 47-50, 1994.

[88] T. Inamura, N. Takezawa, and Y. Kumaki, "Mechanics and energy dissipation in nanoscale cutting," *CIRP Annals-Manufacturing Technology,* vol. 42, pp. 79-82, 1993.

[89] S. Shimada, N. Ikawa, H. Tanaka, and J. Uchikoshi, "Structure of micromachined surface simulated by molecular dynamics analysis," *CIRP Annals-Manufacturing Technology,* vol. 43, pp. 51-54, 1994.

[90] S. Shimada and N. Ikawa, "Molecular dynamics analysis as compared with

experimental results of micromachining," *CIRP Annals-Manufacturing Technology,* vol. 41, pp. 117-120, 1992.

[91] N. Ikawa, S. Shimada, and H. Tanaka, "Minimum thickness of cut in micromachining," *Nanotechnology,* vol. 3, p. 6, 1992.

[92] N. Ikawa, R. Donaldson, R. Komanduri, W. König, P. McKeown, T. Moriwaki, *et al.*, "Ultraprecision metal cutting—the past, the present and the future," *CIRP Annals-Manufacturing Technology,* vol. 40, pp. 587-594, 1991.

[93] D. Lucca, R. Rhorer, and R. Komanduri, "Energy dissipation in the ultraprecision machining of copper," *CIRP Annals-Manufacturing Technology,* vol. 40, pp. 69-72, 1991.

[94] R. Komanduri, Ch, N. rasekaran, and L. Raff, "Molecular dynamics simulation of the nanometric cutting of silicon," *Philosophical Magazine B,* vol. 81, pp. 1989-2019, 2001.

[95] K. Cheng, X. Luo, R. Ward, and R. Holt, "Modeling and simulation of the tool wear in nanometric cutting," *Wear,* vol. 255, pp. 1427-1432, 2003.

[96] Y. Ye, R. Biswas, J. Morris, A. Bastawros, and A. Chandra, "Molecular dynamics simulation of nanoscale machining of copper," *Nanotechnology,* vol. 14, p. 390, 2003.

[97] R. Komanduri, N. Chandrasekaran, and L. Raff, "MD simulation of indentation and scratching of single crystal aluminum," *Wear,* vol. 240, pp. 113-143, 2000.

[98] R. Komanduri, N. Chandrasekaran, and L. Raff, "Effect of tool geometry in nanometric cutting: a molecular dynamics simulation approach," *Wear,* vol. 219, pp. 84-97, 1998.

[99] T. H. Fang and C. I. Weng, "Three-dimensional molecular dynamics analysis of processing using a pin tool on the atomic scale," *Nanotechnology,* vol. 11, p. 148, 2000.

[100] M. Cho, S. Kim, D.-S. Lim, and H. Jang, "Atomic scale stick-slip caused by dislocation nucleation and propagation during scratching of a Cu substrate with a nanoindenter: a molecular dynamics simulation," *Wear,* vol. 259, pp. 1392-1399, 2005.

[101] Y. Yan, T. Sun, S. Dong, and Y. Liang, "Study on effects of the feed on AFM-based nano-scratching process using MD simulation," *Computational Materials Science,* vol. 40,

pp. 1-5, 2007.

[102] Y. Yan, T. Sun, S. Dong, X. Luo, and Y. Liang, "Molecular dynamics simulation of processing using AFM pin tool," *Applied Surface Science*, vol. 252, pp. 7523-7531, 2006.

[103] K. Maekawa and A. Itoh, "Friction and tool wear in nano-scale machining—a molecular dynamics approach," *Wear*, vol. 188, pp. 115-122, 1995.

[104] Z. Lin and J. Huang, "A study of the estimation method of the cutting force for a conical tool under nanoscale depth of cut by molecular dynamics," *Nanotechnology*, vol. 19, p. 115701, 2008.

[105] Q. Pei, C. Lu, H. Lee, and Y. Zhang, "Study of materials deformation in nanometric cutting by large-scale molecular dynamics simulations," *Nanoscale Research Letters*, vol. 4, pp. 444-451, 2009.

[106] Q. Pei, C. Lu, and H. Lee, "Large scale molecular dynamics study of nanometric machining of copper," *Computational Materials Science*, vol. 41, pp. 177-185, 2007.

[107] E. B. Tadmor, M. Ortiz, and R. Phillips, "Quasicontinuum analysis of defects in solids," *Philosophical Magazine A*, vol. 73, pp. 1529-1563, 1996.

[108] J. Q. Broughton, F. F. Abraham, N. Bernstein, and E. Kaxiras, "Concurrent coupling of length scales: methodology and application," *Physical Review B*, vol. 60, p. 2391, 1999.

[109] L. Shilkrot, W. A. Curtin, and R. E. Miller, "A coupled atomistic/continuum model of defects in solids," *Journal of the Mechanics and Physics of Solids*, vol. 50, pp. 2085-2106, 2002.

[110] B. Shiari, R. E. Miller, and D. D. Klug, "Multiscale simulation of material removal processes at the nanoscale," *Journal of the Mechanics and Physics of Solids*, vol. 55, pp. 2384-2405, 2007.

[111] M. Aly, E. Ng, S. Veldhuis, and M. Elbestawi, "Prediction of cutting forces in the micro-machining of silicon using a “hybrid molecular dynamic-finite element analysis” force model," *International Journal of Machine Tools and Manufacture*, vol. 46, pp. 1727-1739, 2006.

[112] X. Sun and K. Cheng, "Multi-scale simulation of the nano-metric cutting process," *The International Journal of Advanced Manufacturing Technology,* vol. 47, pp. 891-901, 2010.

[113] X. Sun, S. Chen, K. Cheng, D. Huo, and W. Chu, "Multiscale simulation on nanometric cutting of single crystal copper," *Proceedings of the Institution of Mechanical Engineers, Part B: Journal of Engineering Manufacture,* vol. 220, pp. 1217-1222, 2006.

[114] H. Pen, Y. Liang, X. Luo, Q. Bai, S. Goel, and J. Ritchie, "Multiscale simulation of nanometric cutting of single crystal copper and its experimental validation," *Computational Materials Science,* vol. 50, pp. 3431-3441, 2011.

[115] V. Krohn and G. Ringo, "Ion source of high brightness using liquid metal," *Applied Physics Letters,* vol. 27, pp. 479-481, 1975.

[116] W. Escovitz, T. Fox, and R. Levi-Setti, "Scanning transmission ion microscope with a field ion source," *Proceedings of the National Academy of Sciences,* vol. 72, pp. 1826-1828, 1975.

[117] J. Orloff and L. Swanson, "Study of a field‐ionization source for microprobe applications," *Journal of Vacuum Science and Technology,* vol. 12, pp. 1209-1213, 1975.

[118] C. Volkert and A. Minor, "Focused ion beam microscopy and micromachining," *MRS bulletin,* vol. 32, pp. 389-399, 2007.

[119] B. Schmidt and K. Wetzig, *Ion beams in materials processing and analysis*: Springer, 2012.

[120] J. Orloff, *Handbook of charged particle optics*: CRC press, 2008.

[121] S. Reyntjens and R. Puers, "A review of focused ion beam applications in microsystem technology," *Journal of Micromechanics and Microengineering,* vol. 11, p. 287, 2001.

[122] J. Gierak, "Focused ion beam technology and ultimate applications," *Semiconductor Science and Technology,* vol. 24, p. 043001, 2009.

[123] K. Kant and D. Losic, "Focused Ion Beam (FIB) Technology for Micro-and Nanoscale Fabrications," in *FIB Nanostructures*, ed: Springer, 2013, pp. 1-22.

[124] S. N. Bhavsar, S. Aravindan, and P. V. Rao, "A critical review on microtools fabrication by focused ion beam (FIB) technology," in *Proceedings of the World Congress on Engineering*, 2009, pp. 1510-1515.

[125] A. Arnau, F. Aumayr, P. Echenique, M. Grether, W. Heiland, J. Limburg, *et al.*, "Interaction of slow multicharged ions with solid surfaces," *Surface Science Reports*, vol. 27, pp. 113-239, 1997.

[126] T. Neidhart, F. Pichler, F. Aumayr, H. Winter, M. Schmid, and P. Varga, "Potential sputtering of lithium fluoride by slow multicharged ions," *Physical Review Letters*, vol. 74, p. 5280, 1995.

[127] M. Sporn, G. Libiseller, T. Neidhart, M. Schmid, F. Aumayr, H. Winter, *et al.*, "Potential sputtering of clean SiO 2 by slow highly charged ions," *Physical Review Letters*, vol. 79, p. 945, 1997.

[128] K. Kuroki, N. Okabayashi, H. Torii, K. Komaki, and Y. Yamazaki, "Potential sputtering of proton from hydrogen-terminated Si (100) surfaces induced with slow highly charged ions," *Applied Physics Letters*, vol. 81, pp. 3561-3563, 2002.

[129] N. Okabayashi, K. Komaki, and Y. Yamazaki, "Potential sputtering and kinetic sputtering from a water adsorbed Si (100) surface with slow highly charged ions," *Nuclear Instruments and Methods in Physics Research Section B: Beam Interactions with Materials and Atoms*, vol. 232, pp. 244-248, 2005.

[130] J. Orwa, K. Nugent, D. Jamieson, and S. Prawer, "Raman investigation of damage caused by deep ion implantation in diamond," *Physical Review B*, vol. 62, p. 5461, 2000.

[131] R. Brunetto, G. A. Baratta, and G. Strazzulla, "Amorphization of diamond by ion irradiation: a Raman study," in *Journal of Physics: Conference Series*, 2005, p. 120.

[132] A. Khomich, R. Khmelnitskiy, V. Dravin, A. Gippius, E. Zavedeev, and I. Vlasov, "Radiation damage in diamonds subjected to helium implantation," *Physics of the Solid State*, vol. 49, pp. 1661-1665, 2007.

[133] V. Popok, J. Samela, K. Nordlund, and V. Popov, "Implantation of keV-energy argon

clusters and radiation damage in diamond," *Physical Review B,* vol. 85, p. 033405, 2012.

[134] G. Dantelle, A. Slablab, L. Rondin, F. Lainé, F. Carrel, P. Bergonzo, *et al.*, "Efficient production of NV colour centres in nanodiamonds using high-energy electron irradiation," *Journal of Luminescence,* vol. 130, pp. 1655-1658, 2010.

[135] J. Mayer, L. A. Giannuzzi, T. Kamino, and J. Michael, "TEM sample preparation and FIB-induced damage," *Mrs Bulletin,* vol. 32, pp. 400-407, 2007.

[136] B. Campbell and A. Mainwood, "Radiation damage of diamond by electron and gamma irradiation," *Physica Status Solidi (a),* vol. 181, pp. 99-107, 2000.

[137] A. Lohstroh, P. Sellin, S. Gkoumas, H. Al-Barakaty, P. Veeramani, M. Özsan, *et al.*, "The effect of fast neutron irradiation on the performance of synthetic single crystal diamond particle detectors," *Diamond and Related Materials,* vol. 19, pp. 841-845, 2010.

[138] J. Schwartz, S. Aloni, D. F. Ogletree, and T. Schenkel, "Effects of low-energy electron irradiation on formation of nitrogen–vacancy centers in single-crystal diamond," *New Journal of Physics,* vol. 14, p. 043024, 2012.

[139] R. Newton, J. Davidson, and M. Lance, "Raman microscopic characterization of proton-irradiated polycrystalline diamond films," *Diamond and Related Materials,* vol. 14, pp. 173-178, 2005.

[140] M. Hamada, T. Teraji, and T. Ito, "Field-induced effects of implanted Ga on high electric field diamond devices fabricated by focused ion beam," *Applied Surface Science,* vol. 216, pp. 65-71, 2003.

[141] P. Lardon, C. Mer, P. Delacour, B. Bazin, D. Tromson, S. Normand, *et al.*, "Investigations of high quality diamond detectors for neutron fluency monitoring in a nuclear reactor," *Diamond and Related Materials,* vol. 15, pp. 815-821, 2006.

[142] F. Aumayr, S. Facsko, A. S. El-Said, C. Trautmann, and M. Schleberger, "Single ion induced surface nanostructures: a comparison between slow highly charged and swift heavy ions," *Journal of Physics: Condensed Matter,* vol. 23, p. 393001, 2011.

[143] H. Gnaser, B. Reuscher, and A. Brodyanski, "Focused ion beam implantation of Ga in

nanocrystalline diamond: Fluence-dependent retention and sputtering," *Nuclear Instruments and Methods in Physics Research Section B: Beam Interactions with Materials and Atoms,* vol. 266, pp. 1666-1670, 2008.

[144] P. Philipp and L. Bischoff, "Investigation of conducting nano-structures on ta-C films made by FIB lithography," *Nuclear Instruments and Methods in Physics Research Section B: Beam Interactions with Materials and Atoms,* vol. 282, pp. 121-124, 2012.

[145] B. Z. Kupfer, R. K. Ahmad, A. Zainal, and R. B. Jackman, "Fabrication and characterisation of triangle-faced single crystal diamond micro-cantilevers," *Diamond and Related Materials,* vol. 19, pp. 742-747, 2010.

[146] W. Wu, Z. Xu, F. Fang, B. Liu, Y. Xiao, J. Chen, *et al.*, "Decrease of FIB-induced lateral damage for diamond tool used in nano cutting," *Nuclear Instruments and Methods in Physics Research Section B: Beam Interactions with Materials and Atoms,* vol. 330, pp. 91-98, 2014.

[147] N. Kawasegi, T. Niwata, N. Morita, K. Nishimura, and H. Sasaoka, "Improving machining performance of single-crystal diamond tools irradiated by a focused ion beam," *Precision Engineering,* vol. 38, pp. 174-182, 2014.

[148] L. Bukonte, F. Djurabekova, J. Samela, K. Nordlund, S. Norris, and M. Aziz, "Comparison of molecular dynamics and binary collision approximation simulations for atom displacement analysis," *Nuclear Instruments and Methods in Physics Research Section B: Beam Interactions with Materials and Atoms,* vol. 297, pp. 23-28, 2013.

[149] J. F. Ziegler and J. P. Biersack, "The stopping and range of ions in matter," in *Treatise on Heavy-Ion Science*, ed: Springer, 1985, pp. 93-129.

[150] J. F. Ziegler, J. P. Biersack, and M. D. Ziegler, *SRIM, the stopping and range of ions in matter*: Lulu. com, 2008.

[151] K. Nordlund, "Molecular dynamics simulation of ion ranges in the 1–100 keV energy range," *Computational Materials Science,* vol. 3, pp. 448-456, 1995.

[152] M. T. Robinson and I. M. Torrens, "Computer simulation of atomic-displacement

cascades in solids in the binary-collision approximation," *Physical Review B,* vol. 9, p. 5008, 1974.

[153] M. T. Robinson, "Computer simulation studies of high-energy collision cascades," *Nuclear Instruments and Methods in Physics Research Section B: Beam Interactions with Materials and Atoms,* vol. 67, pp. 396-400, 1992.

[154] M. Posselt and J. Biersack, "Computer simulation of ion implantation into crystalline targets," *Nuclear Instruments and Methods in Physics Research Section B: Beam Interactions with Materials and Atoms,* vol. 64, pp. 706-710, 1992.

[155] M. Posselt, "Crystal-TRIM and its application to investigations on channeling effects during ion implantation," *Radiation Effects and Defects in Solids,* vol. 130, pp. 87-119, 1994.

[156] K. Nordlund, "Atomistic simulation of radiation effects in carbon-based materials and nitrides," *Nuclear Instruments and Methods in Physics Research Section B: Beam Interactions with Materials and Atoms,* vol. 218, pp. 9-18, 2004.

[157] K. Nordlund and F. Djurabekova, "Multiscale modelling of irradiation in nanostructures," *Journal of Computational Electronics,* vol. 13, pp. 122-141, 2014.

[158] M. Backman, F. Djurabekova, O. H. Pakarinen, K. Nordlund, Y. Zhang, M. Toulemonde, *et al.*, "Cooperative effect of electronic and nuclear stopping on ion irradiation damage in silica," *Journal of Physics D: Applied Physics,* vol. 45, p. 505305, 2012.

[159] M. Backman, M. Toulemonde, O. H. Pakarinen, N. Juslin, F. Djurabekova, K. Nordlund, *et al.*, "Molecular dynamics simulations of swift heavy ion induced defect recovery in SiC," *Computational Materials Science,* vol. 67, pp. 261-265, 2013.

[160] J. Tersoff, "New empirical approach for the structure and energy of covalent systems," *Physical Review B,* vol. 37, p. 6991, 1988.

[161] K.O. Henriksson, K. Vörtler, S. Dreißigacker, K. Nordlund, and J. Keinonen, "Sticking of atomic hydrogen on the tungsten (001) surface," *Surface Science,* vol. 600, pp. 3167-3174, 2006.

[162] K. Nordlund, "Computational materials science of ion irradiation," *Nuclear*

Instruments and Methods in Physics Research Section B: Beam Interactions with Materials and Atoms, vol. 188, pp. 41-48, 2002.

[163] J. A. Brinkman, "On the nature of radiation damage in metals," *Journal of Applied Physics*, vol. 25, pp. 961-970, 1954.

[164] R. Averback, "Atomic displacement processes in irradiated metals," *Journal of Nuclear Materials,* vol. 216, pp. 49-62, 1994.

[165] D. E. Harrison Jr, "Application of molecular dynamics simulations to the study of ion-bombarded metal surfaces," *Critical Reviews in Solid State and Material Sciences,* vol. 14, pp. s1-s78, 1988.

[166] R. Webb and D. Harrison Jr, "Bombardment induced cascade mixing and the importance of post-cascade relaxation," *Nuclear Instruments and Methods in Physics Research,* vol. 218, pp. 697-702, 1983.

[167] T.D. De La Rubia, R. S. Averback, R. Benedek, and W. King, "Role of thermal spikes in energetic displacement cascades," *Physical Review Letters,* vol. 59, p. 1930, 1987.

[168] D. Bacon, A. Calder, F. Gao, V. Kapinos, and S. Wooding, "Computer simulation of defect production by displacement cascades in metals," *Nuclear Instruments and Methods in Physics Research Section B: Beam Interactions with Materials and Atoms,* vol. 102, pp. 37-46, 1995.

[169] M. Caturla, T. Diaz de la Rubia, and G. H. Gilmer, "Disordering and defect production in silicon by keV ion irradiation studied by molecular dynamics," *Nuclear Instruments and Methods in Physics Research Section B: Beam Interactions with Materials and Atoms,* vol. 106, pp. 1-8, 1995.

[170] H. Gades and H. M. Urbassek, "Dimer emission in alloy sputtering and the concept of the “clustering probability”," *Nuclear Instruments and Methods in Physics Research Section B: Beam Interactions with Materials and Atoms,* vol. 103, pp. 131-138, 1995.

[171] W. Phythian, R. Stoller, A. Foreman, A. Calder, and D. Bacon, "A comparison of displacement cascades in copper and iron by molecular dynamics and its application to

microstructural evolution," *Journal of Nuclear Materials*, vol. 223, pp. 245-261, 1995.

[172] M. Ghaly, R. Averback, and T. Diaz De La Rubia, "Surface effects on damage production during ion bombardment: A molecular dynamics study," *Nuclear Instruments and Methods in Physics Research Section B: Beam Interactions with Materials and Atoms*, vol. 102, pp. 51-57, 1995.

[173] G. Gilmer, T. Diaz de la Rubia, D. Stock, and M. Jaraiz, "Diffusion and interactions of point defects in silicon: Molecular dynamics simulations," *Nuclear Instruments and Methods in Physics Research Section B: Beam Interactions with Materials and Atoms*, vol. 102, pp. 247-255, 1995.

[174] K. Nordlund and R. Averback, "Point defect movement and annealing in collision cascades," *Physical Review B*, vol. 56, p. 2421, 1997.

[175] J. Nord, K. Nordlund, and J. Keinonen, "Amorphization mechanism and defect structures in ion-beam-amorphized Si, Ge, and GaAs," *Physical Review B*, vol. 65, p. 165329, 2002.

[176] D. Saada, J. Adler, and R. Kalish, "Transformation of Diamond (sp3) to Graphite (sp2) Bonds by Ion-Impact," *International Journal of Modern Physics C*, vol. 9, pp. 61-69, 1998.

[177] D. Saada, J. Adler, and R. Kalish, "Computer simulation of damage in diamond due to ion impact and its annealing," *Physical Review B*, vol. 59, p. 6650, 1999.

[178] R. Kalish, A. Reznik, K. Nugent, and S. Prawer, 'The nature of damage in ion-implanted and annealed diamond," *Nuclear Instruments and Methods in Physics Research Section B: Beam Interactions with Materials and Atoms*, vol. 148, pp. 626-633, 1999.

[179] R. Kalish, A. Reznik, S. Prawer, D. Saada, and J. Adler, "Ion‐Implantation‐Induced Defects in Diamond and Their Annealing: Experiment and Simulation," *Physica Status Solidi (a)*, vol. 174, pp. 83-99, 1999.

[180] A. Sorkin, J. Adler, and R. Kalish, "Simulation of nanodiamond and nanographite

formation from molten carbon in the presence of hydrogen," *Physical Review B*, vol. 78, p. 155435, 2008.

[181] S. Satake, N. Inoue, J. Taniguchi, and M. Shibahara, "Molecular dynamics simulation for focused ion beam processing: a comparison between computational domain and potential energy," in *Journal of Physics: Conference Series*, 2008, p. 012013.

[182] L. Li, M. Xu, W. Song, A. Ovcharenko, G. Zhang, and D. Jia, "The effect of empirical potential functions on modeling of amorphous carbon using molecular dynamics method," *Applied Surface Science*, vol. 286, pp. 287-297, 2013.

[183] R. Smith, S. D. Kenny, and D. Ramasawmy, "Molecular-dynamics simulations of sputtering," *Philosophical Transactions of the Royal Society of London. Series A: Mathematical, Physical and Engineering Sciences*, vol. 362, pp. 157-176, 2004.

[184] S. Satake, S. Momota, S. Yamashina, M. Shibahara, and J. Taniguchi, "Surface deformation of Ar^+ ion collision process via molecular dynamics simulation with comparison to experiment," *Journal of Applied Physics*, vol. 106, p. 044910, 2009.

[185] S. Satake, S. Momota, A. Fukushige, S. Yamashina, M. Shibahara, and J. Taniguchi, "Molecular dynamics simulation of surface deformation via Ar^+ ion collision process," *Nuclear Instruments and Methods in Physics Research Section B: Beam Interactions with Materials and Atoms*, vol. 272, pp. 5-8, 2012.

[186] A. Burenkov, M. Sekowski, V. Belko, and H. Ryssel, "Angular distributions of sputtered silicon at grazing gallium ion beam incidence," *Nuclear Instruments and Methods in Physics Research Section B: Beam Interactions with Materials and Atoms*, vol. 272, pp. 23-27, 2012.

[187] X. Li, P. Ke, K.R. Lee, and A. Wang, "Molecular dynamics simulation for the influence of incident angles of energetic carbon atoms on the structure and properties of diamond-like carbon films," *Thin Solid Films*, vol. 552, pp. 136-140, 2014.

[188] W. L. Jorgensen, J. Chandrasekhar, J. D. Madura, R. W. Impey, and M. L. Klein, "Comparison of simple potential functions for simulating liquid water," *The Journal of*

Chemical Physics, vol. 79, pp. 926-935, 1983.

[189] L. Verlet, "Computer" experiments" on classical fluids. I. Thermodynamical properties of Lennard-Jones molecules," *Physical Review*, vol. 159, p. 98, 1967.

[190] N. Ikawa, S. Shimada, H. Tanaka, and G. Ohmori, "An atomistic analysis of nanometric chip removal as affected by tool-work interaction in diamond turning," *CIRP Annals-Manufacturing Technology*, vol. 40, pp. 551-554, 1991.

[191] L. A. Girifalco and V. G. Weizer, "Application of the Morse potential function to cubic metals," *Physical Review*, vol. 114, p. 687, 1959.

[192] J. Tersoff, "Modeling solid-state chemistry: Interatomic potentials for multicomponent systems," *Physical Review B*, vol. 39, p. 5566, 1989.

[193] M. S. Daw, S. M. Foiles, and M. I. Baskes, "The embedded-atom method: a review of theory and applications," *Materials Science Reports*, vol. 9, pp. 251-310, 1993.

[194] F. Cleri and V. Rosato, "Tight-binding potentials for transition metals and alloys," *Physical Review B*, vol. 48, p. 22, 1993.

[195] S. Satake, N. Inoue, T. Kunugi, M. Shibahara, and H. Kasahara, "Large-scale molecular dynamics simulation for two Ar clusters impact on 4H–SiC," *Nuclear Instruments and Methods in Physics Research Section B: Beam Interactions with Materials and Atoms*, vol. 257, pp. 639-644, 2007.

[196] M. F. Russo Jr, M. Maazouz, L. A. Giannuzzi, C. Chandler, M. Utlaut, and B. J. Garrison, "Trench formation and lateral damage induced by gallium milling of silicon," *Applied Surface Science*, vol. 255, pp. 828-830, 2008.

[197] J. D. Honeycutt and H. C. Andersen, "Molecular dynamics study of melting and freezing of small Lennard-Jones clusters," *Journal of Physical Chemistry*, vol. 91, pp. 4950-4963, 1987.

[198] D. Faken and H. Jónsson, "Systematic analysis of local atomic structure combined with 3D computer graphics," *Computational Materials Science*, vol. 2, pp. 279-286, 1994.

[199] H. Tsuzuki, P. S. Branicio, and J. P. Rino, "Structural characterization of deformed

crystals by analysis of common atomic neighborhood," *Computer Physics Communications,* vol. 177, pp. 518-523, 2007.

[200] http://isaacs.sourceforge.net/phys/rdfs.html. *g(r) RDF Explanation, assessed on 21 Nov. 2011.*

[201] S. Plimpton, "Fast parallel algorithms for short-range molecular dynamics," *Journal of Computational Physics,* vol. 117, pp. 1-19, 1995.

[202] Z. Tong, Y. Liang, X. Yang, and X. Luo, "Investigation on the thermal effects during nanometric cutting process while using nanoscale diamond tools," *The International Journal of Advanced Manufacturing Technology,* pp. 1-10, 2014.

[203] L. Pelaz, L. A. Marqués, and J. Barbolla, "Ion-beam-induced amorphization and recrystallization in silicon," *Journal of Applied Physics,* vol. 96, pp. 5947-5976, 2004.

[204] V. Borodin, "Molecular dynamics simulation of annealing of post-ballistic cascade remnants in silicon," *Nuclear Instruments and Methods in Physics Research Section B: Beam Interactions with Materials and Atoms,* vol. 282, pp. 33-37, 2012.

[205] D. Hickey, E. Kuryliw, K. Siebein, K. Jones, R. Chodelka, and R. Elliman, "Cross-sectional transmission electron microscopy method and studies of implant damage in single crystal diamond," *Journal of Vacuum Science & Technology A,* vol. 24, pp. 1302-1307, 2006.

[206] K. A. Unocic, M. J. Mills, and G. Daehn, "Effect of gallium focused ion beam milling on preparation of aluminium thin foils," *Journal of Microscopy,* vol. 240, pp. 227-238, 2010.

[207] A. Schilling, T. Adams, R. Bowman, and J. Gregg, "Strategies for gallium removal after focused ion beam patterning of ferroelectric oxide nanostructures," *Nanotechnology,* vol. 18, p. 035301, 2007.

[208] P. Olivero, G. Amato, F. Bellotti, O. Budnyk, E. Colombo, M. Jakšić, *et al.*, "Direct fabrication of three-dimensional buried conductive channels in single crystal diamond with ion microbeam induced graphitization," *Diamond and Related Materials,* vol. 18, pp. 870-876, 2009.

[209] A. Sorkin, "Computer Simulation of the Nucleation of Diamond from Liquid Carbon Under Extreme Pressures," Technion-Israel Institute of Technology, Department of Physics, 2006.

[210] P.Z. Zhu, Y.Z. Hu, T.B. Ma, and H. Wang, "Study of AFM-based nanometric cutting process using molecular dynamics," *Applied Surface Science*, vol. 256, pp. 7160-7165, 2010.

[211] Z. Tong, Y. Liang, X. Jiang, and X. Luo, "An atomistic investigation on the mechanism of machining nanostructures when using single tip and multi-tip diamond tools," *Applied Surface Science*, vol. 290, pp. 458-465, 2014.

[212] H. Balamane, T. Halicioglu, and W. Tiller, "Comparative study of silicon empirical interatomic potentials," *Physical Review B*, vol. 46, p. 2250, 1992.

[213] T.H. Fang, C.I. Weng, and J.G. Chang, "Molecular dynamics simulation of nano-lithography process using atomic force microscopy," *Surface Science*, vol. 501, pp. 138-147, 2002.

[214] C. L. Kelchner, S. Plimpton, and J. Hamilton, "Dislocation nucleation and defect structure during surface indentation," *Physical Review B*, vol. 58, p. 11085, 1998.

[215] R. Komanduri, N. Chandrasekaran, and L. Raff, "Molecular dynamics simulation of atomic-scale friction," *Physical Review B*, vol. 61, p. 14007, 2000.

[216] B. Luan and M. O. Robbins, "The breakdown of continuum models for mechanical contacts," *Nature*, vol. 435, pp. 929-932, 2005.

[217] V. Norouzifard and M. Hamedi, "Experimental determination of the tool–chip thermal contact conductance in machining process," *International Journal of Machine Tools and Manufacture*, vol. 84, pp. 45-57, 2014.

[218] N. Hiromu, "Principles of precision engineering," *Oxford New York Tokyo, Oxford University Press*, pp. 191-195, 1994.

[219] K. Liu and S. N. Melkote, "Effect of plastic side flow on surface roughness in micro-turning process," *International Journal of Machine tools and Manufacture*, vol. 46, pp. 1778-1785, 2006.

[220] R. Neugebauer, W. Drossel, R. Wertheim, C. Hochmuth, and M. Dix, "Resource and energy efficiency in machining using high-performance and hybrid processes," *Procedia CIRP*, vol. 1, pp. 3-16, 2012.

[221] N. Kawasegi, K. Ozaki, N. Morita, K. Nishimura, and H. Sasaoka, "Single-crystal diamond tools formed using a focused ion beam: Tool life enhancement via heat treatment," *Diamond and Related Materials*, vol. 49, pp. 14-18, 2014.

Appendices

Appendix I

Essential specification of FEI Quanta 3D FEG FIB system

FEI Quanta 3D FEG FIB system in Heriot-Watt University.

Electron beam resolution

- High-vacuum
  1.2 nm at 30 kV

  2.9 nm at 1 kV

- Low-vacuum
  1.5 nm at 30 kV

  2.9 nm at 3 kV

- Extended low-vacuum mode
  1.5 nm at 30 kV

Ion beam resolution

- 7 nm at 30 kV at beam coincident point
  (5 nm achievable at optimal working distance)

Electron optics

- High-resolution field emission SEM column optimized for high brightness or high-current
- 60 degree objective lens geometry with through-the lens differential pumping and heated objective apertures
- Accelerating voltage 200 V – 30 kV
- Probe current up to 200 nA – continuously adjustable
- Magnification 30x – 1280kx in "quad" mode

Ion optics

- High-current ion column with Ga liquid-metal ion source
- Source lifetime: 1000 hours guaranteed
- Acceleration voltage: 2 kV – 30 kV
- Probe current: 1 pA – 65 nA in 15 steps
- Beam blanker standard, external control possible
- 15-position aperture strip
- Magnification 40x – 1280kx in "quad" mode at 10 kV
- Charge neutralisation mode for milling of non-conductive samples

Chamber vacuum

- High-vacuum: < 6e-4 Pa
- Low-vacuum: 10 – 130 Pa
- ESEM-vacuum: 10 – 4000 Pa
- Pump-down time: (high-vacuum) < 3 minutes

Digital image processor

- Dwell time: 50 ns – 25 ms adjustable in steps of 100 ns
- Up to 4096 × 3536 pixel resolution
- 256 frame average or integration

Chamber

- 379 mm left to right
- 21 ports
- 10 mm electron and ion beam coincidence point
- Angle between electron and ion columns: 52 º

5-axis motorized stage

- Eucentric goniometer stage

  X = 50 mm

  Y = 50 mm

  Z = 25 mm
- Maximum sample height: 50 mm
- Tilt angle: –15 ºto + 75 º
- Rotation angle: n × 360 °
- Minimum step: 300 nm
- Repeatability @ 0 ºtilt: 2 µm
- Repeatability @ 52 ºtilt: 4 µm

Gas chemistry

- Platinum metal deposition
- Insulator deposition (SiO_2)
- Selective Carbon Mill

Appendix II

Essential specification of the FEI Tecnai T20 transmission electron microscopes (TEMs)

FEI Tecnai T20 transmission electron microscopes (TEMs) in Glasgow University.

Accelerating Voltage: 200 kV

Electron Source: LaB6 filament

Objective Lens: FEI Supertwin

- Cs = 1.2 mm
- Point resolution = 2.4 nm
- Line resolution = 1.5 nm
- Atomic resolution possible in many materials
- Allowable goniometer tilt about 40/30 (double tilt)

Alternative Lorentz objective lens for magnetic studies

- Objective lens current can be reverse for magnetization studies

Gatan Image Filter, GIF 2000

- CCD Camera for image acquisition
- Elemental mapping via energy filtered imaging
- Zero-loss filtering of images and diffraction patterns
- Using the microscope's "EFTEM" lens programme can achieve magnifications from < 10 kx to > 1000 kx
- Suitable for all kinds of image from low-magnification microstructural imaging to high-resolution imaging of atomic columns

SIS Megaview III CCD camera

- High acquisition rate imaging of images and diffraction patterns
- Can be controlled from within TIA
- Mounted at the 35 mm camera port providing a wide field of view ideal for low magnification imaging or imaging of low camera length diffraction patterns

Gatan off-axis TV-rate camera

Appendix III

Essential specification of Precitech Nanoform 250 UltraGrind machine tools

Precitech Nanoform 250 UltraGrind machine tools in Huddersfield University

Machine Base and Control

- Machine Base

  Natural, high-stability, sealed granite, with flood coolant stainless steel enclosure
- Machine Type

  Ultra precision, two, three or four axes CNC contouring machine
- Vibration Isolation

  FEA optimized dual sub-frames for the ultimate in environmental isolation
- Control System

  UPx™ Control System with Optional Adaptive Control Technology
- Operating System

  QNX real time operating system
- Programming Resolution: 0.01 nanometre linear / 0.0000001 ° Rotary

- Performance

  SPDT: Surface Roughness (Ra) < 1.5 nm, Form Accuracy (P-V) < 0.1 μm

  Grinding: Surface Roughness (Ra) < 10 nm, Form Accuracy (P-V) < 0.15 μm

  Tungsten carbide

Linear Hydrostatic Slideways

- Type

  Hydrostatic oil bearing slideways with symmetrical linear motor placement
- Travel: X and Z: 220 mm (8.6")
- Maximum Feedrate: 4,000 mm/min. (157 "/min)
- Drive System: AC linear motor
- Position Feedback Resolution: 16 picometers (0.016 nanometres)
- X-axis Straightness

  Horizontal: 0.2 μm (8 μ")

  Full travel 0.05 μm/25 mm (2 μ")
- Z-axis Straightness

  Horizontal: 0.2 μm (8 μ")

  Full travel 0.05 μm/25 mm (2 μ")
- Vertical Straightness

  Full travel 0.375 μm (15 μ")

Work holding/Positioning Spindle

- Type

  High Performance SP150 Spindle, Slot-type thrust bearing
- Standard Swing Capacity: 250 mm (9.8") diameter
- Motor: Integral brushless motor
- Load Capacity: 60 Kg (133 lbs) 50mm (2") out from spindle nose
- Axial Stiffness: 230 N/μm (1,314,000 lbs./in.)

- Radial Stiffness: 130 N/µm (743,600 lbs./in.)
- Motion Accuracy: Axial/Radial ≤ 15 nm (0.6µ")
- Thermal Control Optional: Liquid cooled chiller +/- 0.1C Accuracy
- C-axis Feedback Resolution: 0.026 arc-sec
- C-axis Position Accuracy: +/- 2 arc-sec
- C-axis Max Speed: 3,000 RPM
- Work Holding Spindle Max Speed: 7,000 RPM

Facility Requirements

- Power

  208 +/-10% or 230 +/-10% VAC - 3.0 KVA 1 phase - 50/60 Hz

- Air Supply

  Typical: 12 SCFM @100 PSIG

- Machine Footprint

  914 mm × 2120 mm × 1700 mm (36" × 83.5" × 67")